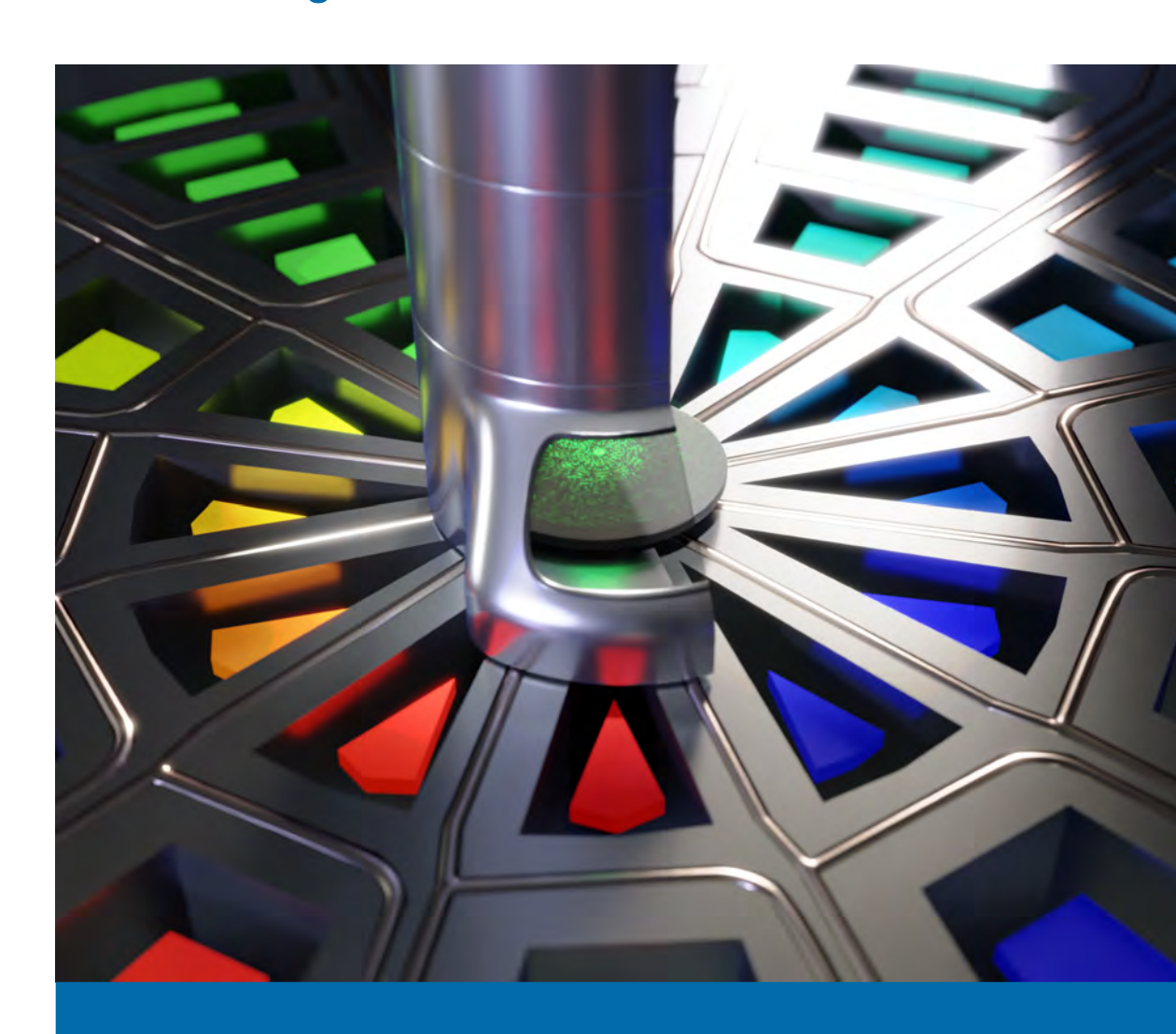
Exploring Adaptive Optics in the Transmission Electron Microscope

Francisco Vega Ibáñez



Supervisor Prof. dr. J. Verbeeck

Thesis submitted in fulfilment of the requirements for the degree of Doctor in Physics Faculty of Science | Antwerpen, March 2025





Faculty of Science

Exploring Adaptive Optics in the Transmission Electron Microscope

Thesis submitted in fulfilment of the requirements for the degree of Doctor in Physics at the University of Antwerp

Francisco Vega Ibáñez

Jury

Chair

Prof. dr. J. De Beenhouwer, University of Antwerp, Belgium

Supervisor

Prof. dr. J. Verbeeck, University of Antwerp, Belgium

Members

Prof. dr. B. Partoens, University of Antwerp, Belgium Prof. dr. T. Juffmann, Universität Wien, Austria Prof. dr. N. Talebi, Kiel University, Germany

Contact

Francisco Vega Ibáñez
University of Antwerp
Faculty of Science, Department of Physics
Electron Microscopy for Material Science
Groenenborgerlaan 171, 2020 Antwerpen, België
M: francisco.vegaibanez@uantwerpen.be
T: +32 (3) 265 32 48

© March 2025 Francisco Vega Ibáñez All rights reserved.



ISBN 987-90-57285-34-7 Wettelijk depot D/2022/12.293/03

Contents

1	Intr	oductio	on: Building and Operating a TEM	1	
	1.1	Buildi	ng an Electron Microscope	3	
		1.1.1	Electron Sources	3	
		1.1.2	Electron Lenses	5	
		1.1.3	Electron Detectors	14	
		1.1.4	Assembling the puzzle: the TEM optical bench	16	
	1.2	Worki	ng with an Electron Microscope	16	
		1.2.1	Conventional Transmission Electron Microscopy (CTEM)	16	
		1.2.2	Scanning Transmission Electron Microscopy (STEM)	18	
		1.2.3	The Point Spread Function and the Reciprocity Principle	19	
2	Exp	anding	the TEM capabilities: Electron Wavefront Shaping	21	
	2.1	Electro	on Wavefront Shaping	23	
		2.1.1	The Wave-Particle Duality of Electrons	23	
		2.1.2	The Aharonov-Bohm Effect	26	
		2.1.3	Phase Plates for Electrons	27	
	2.2	The la	ndscape for Electron Wavefront Shaping	31	
3	Des	igning	an Electrostatic Phase Plate for Aberration Correction	33	
	3.1	Introd	luction	34	
	3.2	.2 Methods			
		3.2.1	Electron Beam Parameters to be Optimized	35	
		3.2.2	Phase Plate Design Parameters	36	
		3.2.3	Phase Plate Pixel Pattern	38	

	3.3	Result	S	41
	3.4	Discus	ssion	44
	3.5	Concl	usion	47
4		ntum V trons	Navefront Shaping with a 48-element Programmable Phase Plate for	51
	4.1	Introd	uction	52
	4.2	Exper	imental considerations	53
		4.2.1	Description of the Electrostatic Phase Plate	53
		4.2.2	Characterization	54
	4.3	Appli	cation Examples	56
		4.3.1	Designer Electron Waveforms	56
		4.3.2	Object Sampling with Different Wavefunctions	58
		4.3.3	Adaptive Optics	61
		4.3.4	Phase programmed Ptychography	62
	4.4	Concl	usion	64
	4.A	Defoc	used Images of the Phase Plate	65
	4.B	Pixel I	ndex	66
5			of phase information from low-dose electron microscopy experi- we at the limit yet?	67
	5.1	Introd	uction	68
	5.2	Setup		69
	5.3	Recov	ering the phase and estimating its precision	71
		5.3.1	Zernike Phase Contrast	71
		5.3.2	Phase Retrieval through inversion	78
		5.3.3	Maximum Likelihood model under Poisson noise	80
	5.4	Nume	rical exercise for 4 unknown phases (1D)	82
	5.5	Nume	rical exercise for a small 2D case	82
	5.6	A moi	re realistic 2D object	83

CONTENTS

	5.7	Discussion	6
		5.7.1 The role of dose	6
		5.7.2 Is RPI the best we can do?	7
		5.7.3 Technological difficulties to realize this	8
		5.7.4 A note on re-normalisation	8
	5.8	Conclusion	9
6	Elec	tron Wavefront Shaping for the End-User 9	1
	6.1	State of the Art Electrostatic Phase Plate for Electrons: AdaptEM Wave-Crafter	2
7	Gen	eral Discussion and Conclusions 9	5
	7.1	Summary and Overview of this Work	6
	7.2	Outlook and Future Prospects for Electron Wavefront Shaping 9	7
	7.3	Conclusion	9
Li	st of 1	Figures 10	7
Li	st of	Tables 10	9
Li	st of .	Abbreviations 11	1
Li	st of A	Author's Contributions 11	3
	7.4	Peer Reviewed Articles	3
	7.5	Conference Talks and Poster Presentations	3
	7.6	Repositories	4
	7.7	Non-peer reviewed contributions	4

CONTENTS

Summary

The electron microscope has evolved from a simple magnification device into a sophisticated, multi-purpose characterization *laboratory*. Technological advances have propelled the technique to the point where we can routinely image individual atoms, determine the chemical composition of materials, reconstruct 3D nanoparticle volumes, and even capture chemical reactions in near real-time.

As traditional electron microscopy approaches its limits, novel strategies are needed to overcome these challenges and extract more information from each electron coming from our sample. Since electron microscopy relies on manipulating coherent electron waves, achieving greater flexibility in controlling these matter waves may be key to addressing many of the field's modern limitations.

Meanwhile, other fields have made remarkable progress in wave manipulation. Notably, the spatial light modulator (SLM), which allows precise position-dependent phase modulation of light, has revolutionized optics by enhancing traditional techniques and enabling numerous new applications.

In electron microscopy, however, the geometry of the fields produced by its active components significantly restricts position-dependent control of the electron wave. Despite these limitations, efforts to adapt the capabilities of SLMs to electron microscopy have shown promise, offering potential solutions to long-standing challenges such as contrast enhancement, aberration correction, and automation.

This work is dedicated to the evaluation of electron wavefront modulation and adaptive optics in the electron microscope, and it is comprised of the following chapters:

- 1. The First Chapter introduces the primary active components of a Transmission Electron Microscope (TEM). By building an electron microscope element by element, we examine the working principles and characteristics of each component, drawing parallels to traditional light optics where applicable. Additionally, the chapter outlines the most common TEM operation modes, highlighting their capabilities and limitations. This foundational understanding establishes the TEM as the framework for the rest of the work.
- 2. The Second Chapter builds upon the discussion from Chapter One, with a focus on the arbitrary shaping of electron wavefronts. To address the geometrical and operational limitations of the TEM active components, we propose the use of an electron wavefront shaping device to expand standard operational modes. This chapter provides essential theoretical and historical background to help understand the principles and strategies behind wavefront shaping. Specifically, the technology utilized in the experimental section of this thesis is the multi-element

- electrostatic phase plate (EPP) for electrons. This wavefront shaping technology will serve as the tool to explore adaptive optics within the framework of TEM in the subsequent chapters.
- 3. Chapter Three examines the potential of an EPP to correct aberrations in the TEM. This theoretical analysis identifies how the morphology of the active components of an EPP influences the electron probe in Scanning Transmission Electron Microscopy (STEM). Furthermore, we assess the current technological capabilities for manufacturing EPPs that meet the design requirements established in this study. Theoretical demonstrations highlight the possibility of correcting spherical aberration using an EPP with relatively few active segments.
- 4. In Chapter Four, we evaluate the performance of a state-of-the-art EPP for electrons. Specifically, we characterize the phase response of each active element within the EPP and analyze the phase sensitivity and error associated with each phase pixel. Additionally, we demonstrate the complex electron wavefront shaping and an automated imaging routine where the phase plate enhances the quality of a STEM image. Finally, we explore some theoretical applications of the device and present simulated results to illustrate these concepts.
- 5. The Fifth Chapter presents a theoretical study that evaluates the limits of dose-efficient measurements in electron microscopy. Specifically, we compare Zernike Phase Contrast (ZPC) with a diffraction-based measurement using a set of phase-structured waves. Notably, we derive and discuss how a slight normalization error can result in an overly optimistic estimation of dose efficiency in ZPC, ultimately favoring diffraction-based measurements under certain conditions. This finding offers valuable insights into dose efficiency and reinforces the relevance of diffraction-based measurements in electron microscopy.
- 6. The Sixth Chapter offers a comprehensive overview of the AdaptEM WaveCrafter, a commercially available EPP for electrons, which is utilized in the experimental section of this study. It describes the development of this technology, highlighting its capability to manipulate electron wavefronts in a TEM. Additionally, the chapter displays the different designs and some of their characteristic features.
- 7. Finally, Chapter Seven summarizes the contents of this thesis by outlining the main takeaways from each chapter and providing an overview of the present and future of electron wavefront shaping.

Samenvatting

De elektronenmicroscoop is geëvolueerd van een eenvoudig vergrotingsapparaat tot een geavanceerd, multifunctioneel karakteriseringsapparaat. Technologische vooruitgang heeft de techniek zover gebracht dat we routinematig individuele atomen kunnen afbeelden, de chemische samenstelling van materialen kunnen bepalen, 3D volumes van nanodeeltjes kunnen reconstrueren en zelfs chemische reacties in bijna real-time kunnen vastleggen.

Nu de traditionele elektronenmicroscopie zijn grenzen nadert, zijn er nieuwe strategieën nodig om deze uitdagingen te overwinnen en meer informatie te halen uit elk elektron dat uit ons monster komt. Aangezien elektronenmicroscopie afhankelijk is van het manipuleren van coherente elektronengolven, kan het bereiken van meer flexibiliteit in het beheersen van deze materiegolven de sleutel zijn tot het aanpakken van veel van de moderne uitdagingen van het veld.

Ondertussen hebben andere gebieden opmerkelijke vooruitgang geboekt op het gebied van golfmanipulatie. Met name de ruimtelijke lichtmodulator (SLM), die nauwkeurige positieafhankelijke fasemodulatie van licht mogelijk maakt, heeft een revolutie teweeggebracht in de optica door traditionele technieken te verbeteren en talloze nieuwe toepassingen mogelijk te maken.

Bij elektronenmicroscopie beperkt de geometrie van de velden die door de actieve componenten worden geproduceerd echter de positieafhankelijke regeling van de elektronengolf aanzienlijk. Ondanks deze beperkingen zijn de pogingen om de mogelijkheden van SLM's aan te passen aan elektronenmicroscopie veelbelovend gebleken en bieden ze potentiële oplossingen voor al lang bestaande uitdagingen zoals contrastverbetering, aberratiecorrectie en automatisering.

Dit werk is gewijd aan de evaluatie van elektronengolffrontmodulatie en adaptieve optiek in de elektronenmicroscoop en bestaat uit de volgende hoofdstukken:

- 1. Het eerste hoofdstuk introduceert de primaire actieve componenten van een transmissie elektronenmicroscoop (TEM). Door element voor element een elektronenmicroscoop op te *bouwen*, onderzoeken we de werkingsprincipes en eigenschappen van elk onderdeel en trekken we waar nodig parallellen met traditionele lichtoptica. Daarnaast schetst het hoofdstuk de meest voorkomende TEM werkwijzen, waarbij hun mogelijkheden en beperkingen worden belicht. Deze basiskennis legt de TEM vast als raamwerk voor de rest van het werk.
- Het tweede hoofdstuk bouwt voort op de discussie uit hoofdstuk één, met de nadruk op de willekeurige vormgeving van elektronengolffronten. Om de geometrische en operationele beperkingen van de actieve componenten van de TEM

aan te pakken, stellen we het gebruik van een apparaat voor het vormen van elektrongolffronten voor om de standaard operationele modi uit te breiden. Dit hoofdstuk biedt essentiële theoretische en historische achtergrond om te helpen begrijpen van de principes en strategieën achter golffront shaping. Specifiek, de technologie die wordt gebruikt in het experimentele gedeelte van dit proefschrift is de multi-element elektrostatische faseplaat (EPP) voor elektronen. Deze golffront vormende technologie zal dienen als het instrument om adaptieve optica te verkennen binnen het kader van TEM in de volgende hoofdstukken.

- 3. Hoofdstuk drie onderzoekt de mogelijkheden van een EPP om aberraties in de TEM te corrigeren. Deze theoretische analyse identificeert hoe de morfologie van de actieve componenten van een EPP de elektronensonde in raster transmissie elektronemicroscoop (STEM) beïnvloedt. Verder beoordelen we de huidige technologische mogelijkheden voor de productie van EPP's die voldoen aan de ontwerpeisen die in deze studie zijn vastgesteld. Theoretische demonstraties benadrukken de mogelijkheid om sferische aberratie te corrigeren met behulp van een EPP met relatief weinig actieve segmenten.
- 4. In hoofdstuk vier evalueren we de prestaties van een geavanceerde EPP voor elektronen. Specifiek karakteriseren we de faserespons van elk actief element binnen de EPP en analyseren we de fasegevoeligheid en -fout van elke fasepixel. Daarnaast demonstreren we de complexe vormgeving van het elektronengolffront en een geautomatiseerde beeldvormingsroutine waarbij de faseplaat de kwaliteit van een STEM-beeld verbetert. Tot slot verkennen we enkele theoretische toepassingen van het apparaat en presenteren we gesimuleerde resultaten om deze concepten te illustreren.
- 5. Het vijfde hoofdstuk presenteert een theoretische studie die de grenzen van dosisefficiënte metingen in elektronenmicroscopie evalueert. Specifiek vergelijken we Zernike fasecontrast (ZPC) met een diffractiegebaseerde meting die gebruik maakt van een reeks fasegestructureerde golven. Met name leiden we af en bespreken we hoe een kleine normalisatiefout kan resulteren in een te optimistische schatting van de dosisefficiëntie bij ZPC, waardoor diffractiegebaseerde metingen onder bepaalde omstandigheden uiteindelijk de voorkeur krijgen. Deze bevinding biedt waardevolle inzichten in dosisefficiëntie en versterkt de relevantie van diffractiegebaseerde metingen in elektronenmicroscopie.
- 6. Het zesde hoofdstuk biedt een uitgebreid overzicht van de AdaptEM WaveCrafter, een commercieel verkrijgbare EPP voor elektronen, die wordt gebruikt in het experimentele deel van deze studie. Het beschrijft de ontwikkeling van deze technologie en benadrukt de mogelijkheid om elektronengolffronten in een TEM te manipuleren. Daarnaast toont het hoofdstuk de verschillende ontwerpen en enkele van hun karakteristieke eigenschappen.
- 7. Tenslotte vat hoofdstuk zeven de inhoud van dit proefschrift samen door de belangrijkste punten uit elk hoofdstuk te schetsen en een overzicht te geven van het heden en de toekomst van elektrongolf vorming.

CONTENTS

"[...]I am impressed by the great limitations of the human mind. How quick we are to learn — that is, to imitate what others have done or thought before — and how slow to understand — that is, to see the deeper connections. Slowest of all, however, are we in inventing new connections or even in applying old ideas in a new field[...]"

Frits Zernike, 1953

CONTENTS

Chapter

Introduction: Building and Operating a TEM

Contents				
1.1	Build	ing an Electron Microscope	3	
	1.1.1	Electron Sources	3	
	1.1.2	Electron Lenses	5	
	1.1.3	Electron Detectors	14	
	1.1.4	Assembling the puzzle: the TEM optical bench	16	
1.2	Working with an Electron Microscope			
	1.2.1	Conventional Transmission Electron Microscopy (CTEM)	16	
	1.2.2	Scanning Transmission Electron Microscopy (STEM)	18	
	1.2.3	The Point Spread Function and the Reciprocity Principle	19	

Exploration and curiosity are inherent traits of the human species. From a young age, we use our senses to explore and gather information. Initially, this information helps us develop basic empirical knowledge. For example, we learn not to touch fire because it burns; however, we often lack the context to connect this sensory input with any plausible explanation other than simply saying, "Fire burns." As we grow older, we learn to use our observations to validate hypotheses and express them as models that relate certain input variables to potential estimated outputs with a degree of accuracy. This process ultimately leads to what is commonly referred to as *scientific knowledge*.

Our senses enable us to perceive reality, but they also have limitations. For instance, our vision is limited to the small range of the electromagnetic spectrum (the visible light spectrum) [1]. Additionally, we cannot see objects smaller than 0.1 mm or those located very far away in space. Furthermore, we often lack the receptors to perceive specific material properties, such as magnetization or polarization.

The development of tools has helped bridge the gap between our senses and the physical phenomena that comprise our reality. Telescopes offer a window into celestial bodies, allowing us to form and validate theories about the origins of our universe. Microscopes, on the other hand, enable us to observe the building blocks of matter and probe their properties. Understanding these properties is the driving force behind advancements in various fields of science.

As we continue to explore and validate new theories, our understanding of the building blocks of matter keeps expanding. This constant expansion creates a demand for improved tools and theories that can accurately determine the properties of the subject.

In microscopy, the minimum dimension that can be observed using electromagnetic radiation is directly linked to the wavelength carried by the probing particle:

$$\delta = \frac{\lambda}{2\eta \sin\left(\alpha\right)} \tag{1.1}$$

This equation is known as Abbe's diffraction limit [2], where λ and η represent the probing particle's wavelength and the refractive index of the medium, respectively. The term $\sin{(\alpha)}$ is the microscope's numerical aperture, which is often set so that the optical aberrations of the imaging system are kept within a reasonable range. Naturally, the initial microscopes were built to use visible light as the probing particle, with a wavelength between 400-700 nm, which limits an optical microscope's magnification to $\approx 2,000\times$ (around 200-250 nm resolution).

Thanks to Abbe's diffraction limit for visible light, our quest for higher magnification led us to explore electromagnetic radiation with shorter wavelengths, ultimately leading to the development of the electron microscope. Accelerated electrons, initially theorized as matter waves by de Broglie [3], have significantly shorter wavelengths due to their inverse relationship between wavelength and momentum:

$$\lambda = \frac{h}{p} \tag{1.2}$$

Where h represents Planck's constant and p denotes the relativistic momentum of elec-

trons. The reduced wavelength for electrons, typically on the order of a couple of picometers (approximately 1×10^{-12} m) when accelerated to 200-300 kV, allows us to examine material properties at the atomic level. Additionally, electrons are relatively easy to extract from a source material and manipulate because of their electric charge. This makes them more attractive than other particles with even smaller matter wavelengths, such as protons or neutrons, when designing such a characterization tool.

Despite the obvious differences between optical and electron microscopes, both come equipped with lenses, deflectors, motorized stages, and other elements to analyze samples. The fact that we can drive analogies between both arises from the fact that, for paraxial waves, where the deviation of the rays from the optical axis $\theta \approx \sin \theta$, the equations describing the propagation of unpolarized light (the Helmholtz wave equation) and electrons (Dirac or Schrödinger equation) take the same form.

The first electron microscope was introduced by Ruska and Knoll almost a century ago [4]. Since then, collaborative efforts have driven the development of the tool into the modern electron microscope we have today. This modern microscope is capable of routinely resolving atomic structures and probing the properties of materials. Over the following sections, we will review a modern transmission electron microscope's (TEM) key hardware, working principles, and operation modes.

1.1 Building an Electron Microscope

The primary function of a microscope is to form a magnified image of an object. Throughout history, people have used semi-transparent round pieces of glass or spherical bodies of water to achieve this [6], which aligns with the definition provided by the Oxford Dictionary: "An instrument consisting of a lens or a combination of lenses that uses light or other electromagnetic radiation to make enlarged images of objects [7]."

With technological advancements, we have evolved from simple glass pieces to precisely polished lenses with controlled apertures, motors, illumination sources, and other sophisticated components present in modern optical microscopes. Furthermore, the electron microscope was developed to achieve higher resolution by re-creating most elements of traditional optical microscopes to work with electrons. This adaptation involved creating electron sources, lenses, deflectors, and detectors. These elements are in constant development to enhance the resolution and broaden the capabilities of the electron microscope, resulting in a versatile measurement tool rather than just a *simple* magnifying device.

1.1.1 Electron Sources

To observe an object, we need to see how it interacts with light—this can involve reflection, scattering, refraction, or blocking of the light. Essentially, the object either acts as a light source or modifies the propagation of light from another source. Electron microscopes follow the same principle; they require an electron source, which is typically located at the top of a cylindrical metallic structure known as the *optical* column.



Figure 1.1: The development of microscopes throughout history has been quite remarkable. The Nimrud lens (a), one of the oldest dating evidence of the use of artifacts to magnify objects, was found in modern-day Iraq, and it is dated to 750 B.C. (adapted from https://en.wikipedia.org/wiki/File:Nimrud_lens_British_Museum.jpg by Geni). In the 17th century, Robert Hooke published some remarkable work on biology in his book "Micrographia," where he used a microscope manufactured by Christopher White, shown in (b), to observe biological specimens [5]. Modern optical microscopes, like the one shown in (c) by the Zeiss company (adapted from https://www.zeiss.com/microscopy/en/products/light-microscopes/super-resolution-microscopes/elyra-7.html), boast advanced optical and mechanical elements and computational integration for image processing. The first-ever prototype for an electron microscope was built by Ernst Ruska and is shown in (d) (adapted from https://commons.wikimedia.org/wiki/File:Ernst_Ruska_Electron_Microscope_-_Deutsches_Museum_-_Munich-edit.jpg by J Brew). In contrast, one of EMAT's modern TEM by Thermo Fisher Scientific is shown in (e).

An ideal electron source should produce a steady flow of electrons with a controllable current density and high spatial coherence.

There are two main types of electron sources: thermionic and field emission. Thermionic sources work similarly to incandescent light bulbs. A current passing through a filament generates heat, providing enough energy for the electrons to escape into the column. To withstand the high temperatures required for thermionic emission, thermionic electron sources are typically made of tungsten, lanthanum hexaboride (LaB_6), or cerium hexaboride (CeB_6). Thermionic sources also come with a negatively biased cylinder (Wehnelt Cylinder) around the emitting element to suppress the emission from unwanted areas (see fig. 1.2(a)).

In contrast, in a Field Emission Gun (FEG), a relatively large bias is applied to a sharp

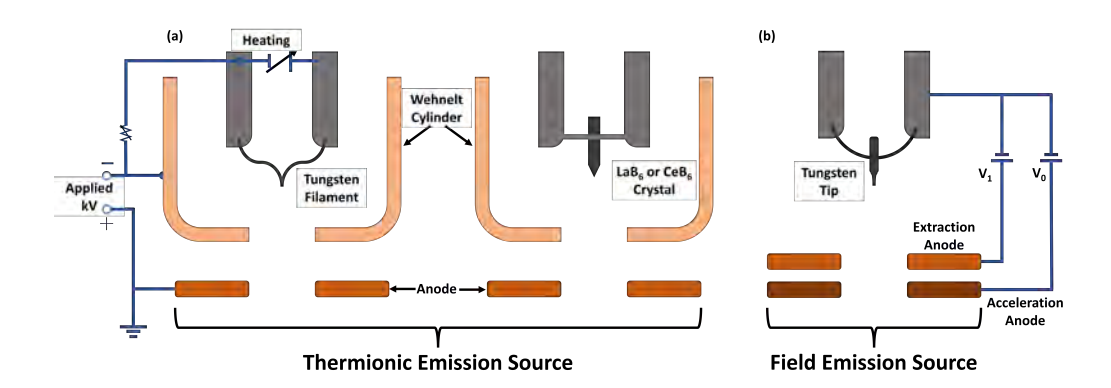


Figure 1.2: Diagram showing the main components of Thermionic (a) and Field Emission (b) electron sources. The simplified circuit in (a) (similar to (b), but not drawn for convenience) and (c) indicates the basic principle for extraction and acceleration of the electrons for each case (adapted from [8]).

tungsten tip (anode), generating a strong electric field. This field lowers the work function of the tip, allowing a quantum tunneling current of electrons to flow from the tungsten tip into the column (see fig. 1.2(b)). Notably, FEGs provide increased brightness and coherence, enabling electron microscopes to improve not only their spatial resolution but also the efficiency of spectroscopic techniques such as Electron Energy Loss Spectroscopy (EELS) and Electron Dispersive X-ray Spectroscopy (EDX).

As mentioned above, when designing an electron source, it is essential to consider brightness and coherence, both spatial and temporal. Regarding its brightness, in a TEM experiment, the electron current is typically set between 0.01 to 3 nA, depending on the sensitivity of the sample to beam-induced damage and the capability of such electron source to maintain coherent emission, which translates to around $6x10^7$ to $2x10^{10}$ electrons per second. In contrast, evaluating spatial coherence can be challenging, but generally, illuminating coherently a few microns in the condenser aperture is sufficient for most experiments. However, if the experiment involves assessing interference between partial wavelets or creating a complex optical wavefront profile, a few tens of microns may be needed. Lastly, temporal coherence is linked to the energy spread of the electrons extracted from the source, which is particularly crucial for high-energy resolution spectroscopic methods such as EELS. A comparison of the relevant parameters of the most common commercially available electron sources, including different types of thermionic and field-emitting sources, can be found in table 1.1.

1.1.2 Electron Lenses

When electromagnetic radiation propagates through a medium other than a vacuum, its interaction with the material's charges alters its propagation. These interactions occur with bound charges (i.e., electrons tightly bound to atoms or atomic nuclei) and unbound charges (i.e., free electrons in conductors). Furthermore, the changes in the wave's behavior (including its propagation speed and attenuation) are governed by the electromagnetic properties of the medium, specifically its permittivity (ε) and permeabil-

Table 1.1: Operational	and opti	cal parameters	s of some o	of the r	nost commonly used
electron sources [9,10]	_	-			•

		Thermionic		Field E	mission
Parameter	Units	Tungsten	LaB ₆	Schottky	Cold FEG
Work Function	eV	4.5	2.4	3	4.5
Operating Temperature	K	2700	1700	1800	300
Current Density (100 kV)	A/m^2	5	10^{2}	10^{5}	10^{6}
Source Diameter	nm	$5x10^4$	10^{4}	15	2
Energy Spread (100 kV)	eV	3	1.5	0.7	0.4
Brightness (100 kV)	A/m^2sr	10^{10}	$5x10^{11}$	$5x10^{12}$	10^{13}
Emission Current Stability	%/hour	<1	<1	<1	5
Operating Vacuum	Pa	10^{-2}	10^{-4}	10^{-6}	10^{-8}

ity (μ) . These properties determine how the medium responds to the electromagnetic field of the radiation itself. Compared to a vacuum, where permittivity and permeability are ϵ_0 and μ_0 , respectively, the medium's relative permittivity ($\epsilon_r = \epsilon/\epsilon_0$) and relative permeability ($\mu_r = \mu/\mu_0$) dictate the degree to which the wave slows down and dissipates.

The change in the wave's phase velocity v is proportional to the contrast between the medium's permittivity and permeability and those of the vacuum. Specifically:

$$v = \frac{1}{\sqrt{\epsilon \mu}} = \frac{c}{\sqrt{\epsilon_r \mu_r}},\tag{1.3}$$

where $c = 1/\sqrt{\epsilon_0 \mu_0}$ is the speed of light in a vacuum.

Furthermore, for any pair of media, the ratio of the sine of the incident angle θ_1 to the sine of the angle of refraction θ_2 is equal to the ratio of the phase velocities of the wave in the two media $\frac{v_1}{v_2}$, which is also equal to the refractive index of the second medium with respect to the first, given by the ratio $\frac{n_2}{n_1}$. This relationship is known as Snell's law¹ [12]:

$$\frac{\sin \theta_1}{\sin \theta_2} = \frac{n_2}{n_1} = \frac{v_1}{v_2} \tag{1.4}$$

As an example, as light passes through a transparent material, such as the windows in our homes, the deviation of light is nearly constant for all rays, meaning we can barely perceive alteration of the rays coming from an object behind it. However, if the glass through which light passes varies in thickness, it will cause the light to change direction in proportion to the angle of the surface upon entering and exiting the glass. This is similar to how some shower screens blur what is behind them, as any light passing through them will be reflected in different directions. Essentially, lenses work similarly to the previous examples. A polished piece of glass with a spherical surface bends the

¹The refraction of rays, now known as Snell's law, was a long-standing problem dating back to ancient Greece. The oldest record of a (wrong) description of ray propagation from air into glass dates back to ancient Greece and Ptolemy's book on Optics. Abu Said al-Ala Ibn Sahl later corrected Ptolemy's work, providing the first correct mathematical description of what we now call Snell's law [11].

incoming rays proportionally to the distance of the ray to the center of the lens, causing them to converge at a focal point.

Classical optics often use ray diagrams to illustrate how light travels, such as the one shown in fig. 1.3. The diagram shows how rays coming from an object of size a_0 on the Object Plane (OP) are focused by the lens at a focal distance f in the Back Focal Plane (BFP). These rays then converge to create an image of size a_i at a distance d_i on the Image Plane (IP). It's important to note that this diagram can be followed in either direction (top to bottom or bottom to top) and that the names of the different planes are simply a matter of convention.

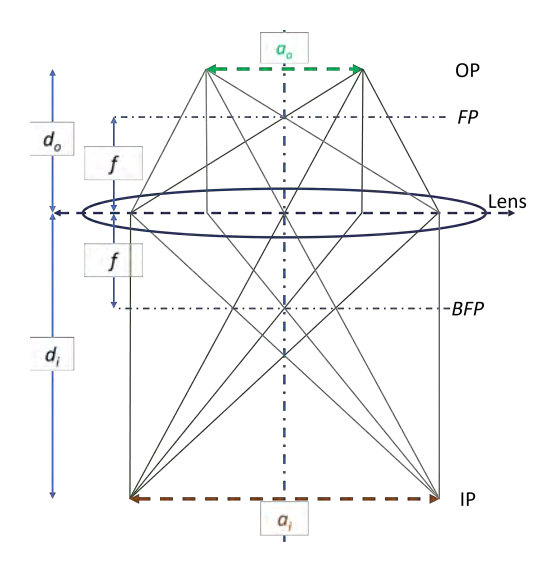


Figure 1.3: Typical ray representation of a convex lens, the light emitted from an object of width a_0 is bent and then replicated at a distance d_i , producing an image of size a_i . The bent rays form a crossover point on both foci on either side of the lens at a focal distance f.

As the equations describing light and electrons' propagation in the paraxial approximation are similar, we can again describe electron lenses' behavior akin to round glass lenses. Electron lenses use an electrostatic or magnetic field to replicate the spherical profile found in an optical lens, creating a focusing effect on the electron beam that passes through. It is important to note that the diagram in fig. 1.3 should be taken as a visual reference only, as it is exaggerated horizontally. Despite the difference in scale, both light and electron lenses have two main objectives: creating a magnified image of each point in the object or focusing parallel rays to the smallest possible probe in the focal plane of the lens.

Electromagnetic Lenses

Electromagnetic electron lenses use a magnetic field to focus an electron wave. When an electric current flows through a cylindrical coil, known as a solenoid, it generates a magnetic field with a toroidal shape around the wire. This magnetic field induces magnetization in soft iron pole pieces around the coils, which shape and concentrate the

field into a rotationally symmetric configuration along the optical axis, as illustrated in Figure fig. 1.4.

An electron traveling through this magnetic field experiences a force that is proportional to the field, as described by the Lorentz force:

$$\mathbf{F} = -e \left(\mathbf{v} \times \mathbf{B} \right) \tag{1.5}$$

We can expand the cross-product to get the force components along each axis:

$$F_{\hat{r}} \approx -ev_{\phi}B_z \tag{1.6}$$

$$F_{\hat{r}} \approx -ev_{\phi}B_{z}$$

$$F_{\hat{\phi}} = -e(v_{z}B_{r} - v_{r}B_{z})$$

$$F_{\hat{z}} \approx ev_{\phi}B_{r}$$

$$(1.6)$$

$$(1.7)$$

$$F_{\hat{z}} \approx e v_{\phi} B_r$$
 (1.8)

When analyzing the components of the Lorentz force, we find that electrons entering a magnetic field experience an azimuthal force, which causes them to spiral around the optical axis. Additionally, under the paraxial approximation ($r \ll 1$), the strength of the radial field B_r can be approximated as proportional to the radial distance r. Therefore, the spiraling motion is primarily influenced by the axial field B_z . The term $v_r B_z$ adds a secondary oscillatory component to the azimuthal force.

Notably, flipping the current's direction will flip the magnetic field's axial component, changing the rotation direction. Additionally, we see that the electrons that deviate from the optical axis will be subjected to a larger azimuthal force, which, in turn, will increase the radial force component, focusing them toward the optical axis.

Focusing Effect and Lens Curvature

The focusing strength of the electromagnetic lens is intimately related to the curvature of the electron's trajectory.

The centripetal force experienced by an electron traveling through a rotationally symmetric electromagnetic lens is given by:

$$F_{\hat{r}} = \frac{mv_{\phi}^2}{R} \tag{1.9}$$

Substituting the radial Lorentz force component, we get:

$$-ev_{\phi}B_{z} = \frac{mv_{\phi}^{2}}{R} \tag{1.10}$$

Solving for *R* we can obtain the helical path of the electron as it travels through the lens' field, often found in literature as the cyclotron radius, or Larmor precession:

$$R = \frac{mv_{\phi}}{eB_{z}} \tag{1.11}$$

This equation indicates that the radius of curvature R is inversely proportional to the strength of the axial magnetic field B_z . From the perspective of the electron traveling along the optical axis, the magnetic field varies from 0 to B_{max} and then returns to 0, hence the notion of this *curvature*.

From this, after going through some mathematical derivation, it can be proven that the focusing strength of a lens is proportional to the square of the magnetic field along the electron's trajectory [13]:

$$\frac{1}{f} \propto \int B_z^2(z)dz \tag{1.12}$$

While this explanation provides some general guidelines on the behavior of electromagnetic lenses, for a more in-depth analysis of electron optics, several dedicated books on electron microscopy detail this phenomenon [9,13–15].

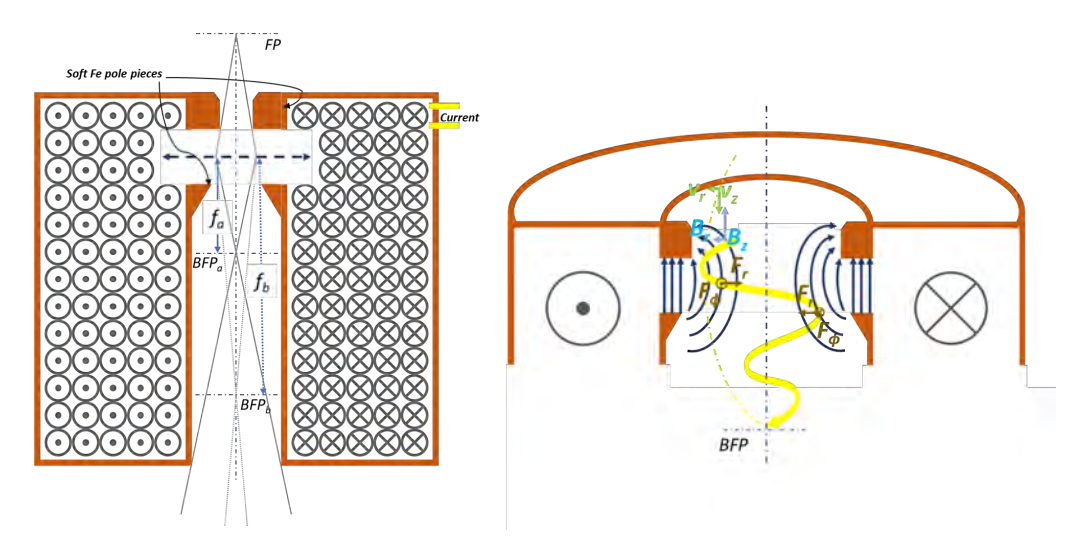


Figure 1.4: The diagram illustrates the cross-section of an electron lens in 2D (left). When electrons enter the lens from a point in the focal plane (FP), they are deflected by the magnetic field created by the current passing through the coils. The current flowing into the page is represented by \otimes , while the current flowing out of the page is represented by \odot . This current magnetizes the soft-iron pole pieces, generating a toroidal magnetic field around the coils. The distance to the back focal plane (BFP) can be adjusted by increasing (f_a) or decreasing (f_b) the current flowing through the coils. The notation is similar to that in fig. 1.3 to emphasize the parallels between electron and optical lenses. The diagram is extended (right) to represent the electron velocity upon entering the lens $\mathbf{v} = (v_r, 0, v_z)$, the magnetic field within the lens $\mathbf{B} = (B_r, 0, B_z)$, and the azimuthal (F_ϕ) and radial (F_r) forces resulting from the interaction. (adapted from [8]).

Despite significant technological advancements, electromagnetic lenses still exhibit imperfections. Small variations in the alignment or thickness of the copper coils result in inconsistencies in the magnetic field generated by the lens. Additionally, the soft iron pole pieces and surrounding conductors can experience switching of ferromagnetic

domains due to the lens's magnetic field, leading to remanent magnetization. This remanent magnetization in the surrounding conductors leads to hysteresis and aberrations.

To address these issues, reset routines are often run on the coils to restore ferromagnetic domains and lenses typically incorporate a water cooling system that helps minimize resistance variations in the copper coils due to thermal gradients. Furthermore, most lens modules are equipped with a pair of deflectors positioned at the top to align the electron beam with the lens's entrance, as well as a stigmator located at the bottom (which will be briefly discussed in the following sections) to correct for irregularities in the magnetic field.

Electrostatic Lenses

In an electrostatic lens, we assume that the magnetic field is zero and only consider the electric field term, represented by **E**. The derivation becomes much simpler since there is no longer a vector product between the electrons and the field. With a symmetrical cylindrical electric field given by $\mathbf{E} = (E_r, 0, E_z)$ eq. (1.5)'s components become:

$$F_{\hat{r}} = -eE_r \tag{1.13}$$

$$F_{\hat{z}} = -eE_z \tag{1.14}$$

When electrons pass through the optical axis, the radial component of the electric field (F_f) is canceled out. However, if electrons enter the lens aperture at an angle, they will acquire a radial velocity component from the inhomogeneous local electric field. This can cause the electrons to converge or diverge, depending on the direction of E_r .

The concept of electrostatic lensing was implicitly introduced in this chapter during the discussion of electron emission. In a microscope with a thermionic gun, the Wehnelt cylinder (shown in fig. 1.2(a)) is typically negatively biased and serves as the first lens through which electrons pass. Electron microscopes can also utilize the $F_{\hat{z}}$ component of the electrostatic Lorentz force to accelerate electrons using a simple acceleration anode (as shown in fig. 1.2(b)) or a more complex array of anodes with an electric field gradient for a more robust and stable acceleration. In general, an electrostatic lens is a metallic plate or an array of metallic plates set at high voltages, which can cause an electron beam to converge or diverge and accelerate or decelerate the electrons passing through it (see fig. 1.5).

Nonetheless, when working with electrons at high acceleration voltages (100-300 kV), magnetic lenses are often a more practical solution. Achieving similar focal lengths with electrostatic lenses at such energy levels and convergence requirements would necessitate unfeasible electrostatic fields or disproportionately large dimensions for the electrodes. As a result, electrostatic lenses are more commonly used in microscopes that operate with lower-energy electrons [16–18], even as aberration correctors [19,20]

An important point to consider within the scope of the thesis is that even though threeelectrode electrostatic lenses, also called Einzel lenses, are not practical for focusing highenergy electrons, they can be used to locally shift the phase of the electron beam without

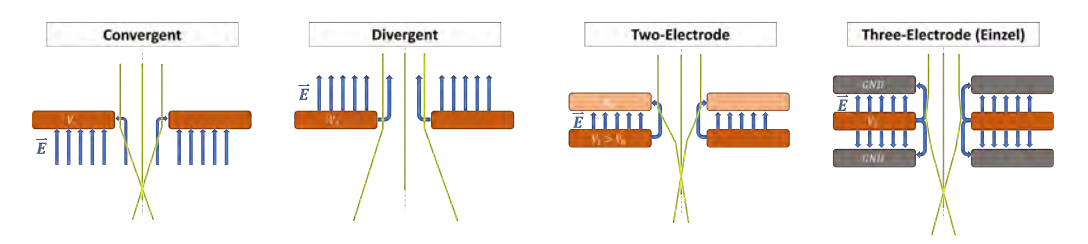


Figure 1.5: Ray diagram representation of different types of electrostatic lenses: convergent (a), divergent (b), two-electrode (c), and three-electrode (Einzel lens) (d). The figure dimensions are exaggerated to illustrate the effect of the lens.

changing its propagation velocity. This ability has various potential applications, which will be explored later.

Electron Lens Aberrations

In the previous sections, we discussed how imperfections in manufacturing and environmental variations can affect the field generated by a lens, resulting in typical parasitic aberrations. However, even with perfect lenses, aberrations are inevitable. The paraxial approximation suggests that every point can be reproduced in the image, convolved by a point spread function (PSF) induced by the diffraction-limited optical system (given by eq. (1.1)). However, the difference in effective path length between rays entering the lens at different angles or for rays with slight energy variations results in different focal lengths. This effect is even more pronounced in electron microscopy, leading to the assertion that electron microscopes, unlike optical ones, are aberration-limited rather than diffraction-limited. In other words, the aberration limit prevents arbitrary selection of our numerical aperture, ultimately resulting in lower effective resolution even at higher numerical apertures.

The impact of spherical aberration has been known for almost a thousand years [21]. However, it wasn't until 1857 that Seidel broke down the first-order monochromatic aberrations into different constituent terms. These are now commonly referred to as the five Seidel aberrations: spherical, coma, astigmatism, field curvature, and distortion² [22]. Generally, we can find distinct notations for the aberrations of an optical system across different fields [23]. However, for this work, it is most convenient to follow the notation of Uhlemann and Haider [24]. This notation allows us to express the aberration function $\chi(\theta,\phi)$ as a weighted sum of cosines:

²While defocus is technically an aberration, it is typically not considered as one since it can be fixed by changing the image plane or changing the strength of the lens.

$$\chi(\theta,\phi) = \frac{2\pi}{\lambda} \Big[\theta \quad A_0 \cos(\phi - \phi_{11}) + \frac{\theta^2}{2} \left(A_1 \cos(2(\phi - \phi_{22})) + C_1 \right) + \frac{\theta^3}{3} \left(A_2 \cos(3(\phi - \phi_{33})) + B_2 \cos(\phi - \phi_{31}) \right) + \frac{\theta^4}{4} \left(A_3 \cos(4(\phi - \phi_{44})) + S_3 \cos(2(\phi - \phi_{42})) + C_3 \right) + \frac{\theta^5}{5} \left(A_4 \cos(5(\phi - \phi_{55})) + B_4 \cos(\phi - \phi_{51}) + D_4 \cos(3(\phi - \phi_{53})) \right) \Big]$$
(1.15)

Following eq. (1.15), we can determine the phase shift on the electron wavefront at a specific azimuthal position ϕ for a given numerical aperture θ . The weighting parameters used for this calculation include: shift A_0 , astigmatism $A_{i>0}$, coma B_i , defocus C_1 , spherical aberration C_3 , star aberration S_i , and three-lobe aberration. These weighted sum components are visually represented in fig. 1.6. Considering the summation of the effect of all the aberrations, one can construct the phase term imposed by them on the electron wavefront as $e^{i\chi(\theta,\phi)}$.

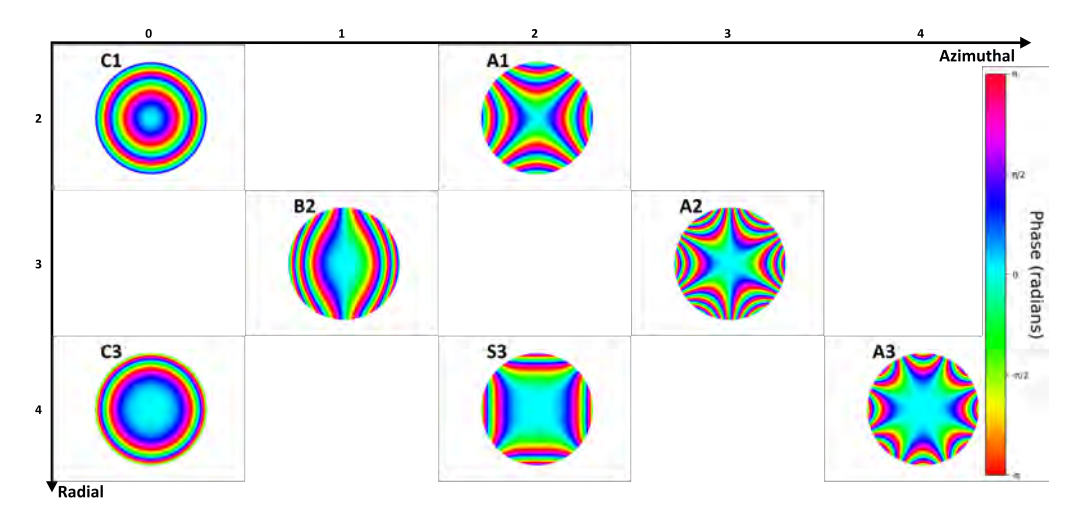


Figure 1.6: Simulated phase aberrations constructed from eq. (1.15). The coefficients used for the simulations are C1 = A1 = 20nm, $B2 = A2 = 2\mu m$, and $C3 = S3 = A3 = 75\mu m$. All phase profiles are over a semi-convergence angle $\alpha = 20 \ mrad$. The color bar on the right represents the phase, while the amplitude is equal to one throughout the array

In 1934, Otto Scherzer and Ernst Brüche extended this theory to electrons, largely establishing the theoretical basis of geometrical electron optics [25]. In their work, they solved a Laplacian equation system for the electromagnetic potential, given that the electron energy is conserved and that the following assumptions apply:

1. The Electromagnetic field is rotationally symmetric

- 2. The Electromagnetic field is static
- 3. The electron velocity does not change direction
- 4. There are no space charges

From this exercise, Scherzer concluded that every electromagnetic lens must have an inherent positive spherical aberration [26].

In addition to the inherent lens aberrations, the energy spread of the electron beam can cause chromatic aberrations. This is because the position of the back focal plane of a lens depends on the electron's wavelength, which in turn comes from its velocity³. However, modern TEMs can typically compensate for this effect by adding a monochromator. The monochromator, which typically operates in conjunction with the electron gun lens, increases the spatial spread of the electron beam based on their energy levels. After the beam is dispersed, an aperture is positioned along its path to narrow the energy spread of the electrons before they reach the condenser system.

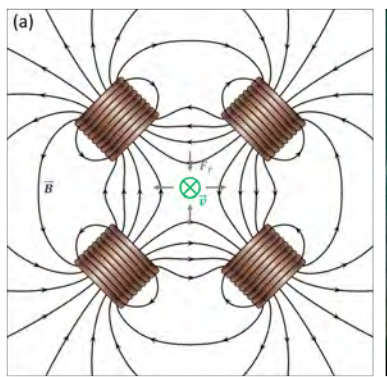
Aberration Correction and Multi-Polar Lenses

As discussed before, there are limitations to using electrostatic lenses for fast electrons in the TEM column. Due to this, we are restricted to using convergent electromagnetic lenses. The absence of a divergent electron lens makes correcting rotationally symmetric aberrations challenging, which affects the instrument's performance. However, Scherzer proposed a solution to this problem shortly after he described the electron lens aberrations [28, 29]. Scherzer's proposal involves introducing multi-polar lenses to generate non-rotationally symmetric fields, compensating for the aberrations. One example of these lenses is the previously hinted stigmator, which employs a quadrupolar lens to correct the parasitic aberrations generated by inhomogeneities in the lens field. Multipolar electromagnetic lenses are constructed based on the same principle as cylindrical electromagnetic lenses, with the difference being that they use more than one solenoid, typically oriented perpendicular to the optical axis, as shown in fig. 1.7.

In general, correcting lens aberrations follows a logical order. By examining the expansion of the aberration function as shown in eq. (1.15) and illustrated in fig. 1.6, we can determine that the next aberration coefficient to address is determined primarily by its multiplicity, followed by the order of θ . From this, and given that first-order astigmatism (A_1) can be corrected with relative ease, we get that the first significant obstacle affecting the performance of the TEM is Spherical Aberration (C_3), often denoted also as C_s in literature.

Several attempts to experimentally realize Scherzer's original concept were made in the later half of the twentieth century with varying levels of success [30–39]. However, it was not until 50 years later that the Haider-Rose-Urban project successfully demonstrated this concept [40–42]. Despite being seemingly straightforward on paper, the accuracy and stability required to implement a spherical aberration corrector successfully posed one of the most significant breakthroughs in the history of electron microscopy [43]. Technically

³This effect is similar to how light is refracted at different angles depending on its color [27], giving its name to the aberration.





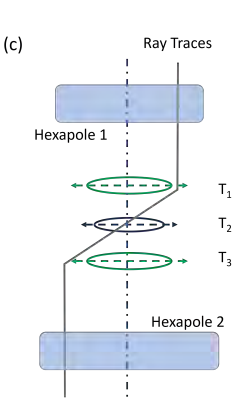


Figure 1.7: The diagram in (a) depicts the magnetic field lines (in black) in a quadrupolar lens. As the electrons move into the page with a velocity represented by \mathbf{v} , they experience a radial Lorentz force $F_{\hat{r}}$. This force can be adjusted by regulating the current in each solenoid (adapted from http://commons.wikimedia.org/w/index.php?curid=11 117039 by Geek3). In (b), there is an image of a hexapole corrector used in a TEM (source http://commons.wikimedia.org/w/index.php?curid=16445968 by Materialscientist). Finally, (c) shows a simplified ray diagram of a double-hexapole aberration corrector, including the transfer lenses.

speaking, the original demonstration of such a spherical aberration corrector comprised two magnetic hexapoles coupled by transfer doublets, as shown in fig. 1.7(b,c).

Nowadays, aberration correctors are commercially available and capable of correcting well beyond third-order spherical aberration [44, 45], even for lower acceleration voltages [46–48]. Altogether, the development and refinement of multi-polar electromagnetic lenses has expanded the horizon of TEM, making it one of the most capable characterization techniques.

1.1.3 Electron Detectors

So far, we have discussed the process of extracting electrons from a source and manipulating their paths using lenses and other electromagnetic components. However, even the most sophisticated electron gun and precise optical system would be ineffective without a capable device to detect the electrons. In optical microscopy, our eyes detect visible light emitted or reflected by objects, but they are limited in capturing images or providing precise measurements. Similarly, in electron microscopy, the detector plays a crucial role in converting the electromagnetic radiation or scattered electrons from a sample into meaningful data. By using lenses to filter and project this radiation in various ways, we can obtain detailed information about the specimen, such as a real-space image with atomic resolution, a diffraction pattern in momentum space, or a spectrum revealing chemical composition.

In the TEM, electrons are extracted from a source and initialized in a *well-defined* quantum state, determined by the spatial and temporal coherence of the instrument [49,50]. When these electrons interact with a sample, they encode information about the specimen into

their altered wavefuction. Measuring this alteration with an electron detector allows us to retrieve critical structural and chemical details. However, the detection process is inherently affected by noise, which limits the accuracy of even unbiased measurements.

Detection in an electron microscope relies on energy exchange between the high-energy probing electrons and the detector material. In the TEM column, the electrons possess kinetic energy far exceeding the detector system's thermal energy, represented by (k_BT) . This energy transfer alters the detector's state, generating a measurable response. Assuming the signal surpasses noise sources like electronic or shot noise, this response can be processed and converted into a computationally analyzable format.

While factors like Detective Quantum Efficiency (DQE) and Modulation Transfer Function (MTF) influence the detector's ability to maintain spatial resolution and signal fidelity, this section will emphasize the geometric and positional aspects of detectors. Focusing on these practical elements provides a solid foundation for understanding image formation in common TEM operational modes without delving into the complex physics of signal readout or electronic conversion.

Photographic film screens were one of the earliest electron detectors used in TEM [9,51]. When the transmitted electrons struck the screen, an image was produced based on an interference pattern, which showed a contrast between areas with high and fewer electron counts. Eventually, photographic film screens were replaced with electronic pixelated detectors for enhanced performance and convenience [52–54], while the fundamental concept of image formation remained the same. The resolution of pixelated detectors is generally limited by how accurately we can track the spread of energy deposited by an electron in a finite region of space. Furthermore, increasing the number of pixels allows a finer sampling of the electron spread over a fixed collection angle (given that the energy spread remains within one pixel). However, as discussed in section 1.2.3, having more pixels will substantially increase data volume.

Another approach is to use the microscope's probe-forming optics to encode spatial information by densely sampling the material with a fine electron beam. A single-pixel detector can then capture the scattered electron signal, providing one value for each spatially encoded beam. This simplifies the readout process, as only one value needs to be saved, which is proportional to the number of electrons scattered onto the detector's collection range. Furthermore, interpreting the signal becomes easier because the contrast is a simple comparison between intensity values from each recording. The principle behind single-pixel detectors is similar to that of a single-pixel comprising a pixelated detector. However, single-pixel detectors typically have a ring shape and are positioned in the dark-field region below the sample, where the distance between the detector and the sample determines its angular collection range⁴.

⁴In most TEMs, the distance in question is not a fixed physical position, as that would significantly restrict the instrument's versatility. Instead, a projection system is responsible for projecting the image or diffraction pattern onto a detector. This setup allows users to adjust the distance from the sample to the camera, known as the camera length.

1.1.4 Assembling the puzzle: the TEM optical bench

The preceding sections covered the primary components needed to build an electron microscope. In an actual setup the microscope includes a cooling system and multiple vacuum pumps. The instrument is normally placed on a sturdy base and has a thick frame to minimize environmental vibrations. In some cases, it is also enclosed in a metallic box, eliminating undesired external electromagnetic radiation and thermal fluctuations. Additionally, multiple active elements can often work together to form a *module*. Following the established convention in this work, the top module of an electron microscope is responsible for the extraction of electrons⁵, consisting of the gun and accelerator, followed by the condenser. Next is the probe corrector (for probe-corrected instruments), followed by the objective, typically located in the middle of the optical bench, which houses the sample holder. Below the objective module, one can find an image corrector (for image-corrected instruments), followed by the projection system, and the spectroscopy module, often having different detectors along the way. All these components are sketched in fig. 1.8, where a diagram of a state-of-the-art TEM is shown.

1.2 Working with an Electron Microscope

After reviewing the components often found in a TEM, we are now ready to use the tool for material characterization. The two most commonly used modes in a TEM are conventional TEM (CTEM) and scanning TEM (STEM). In the following sections, we will briefly introduce these modes, discuss the physics of image formation, and provide an overview of each's main advantages and limitations.

1.2.1 Conventional Transmission Electron Microscopy (CTEM)

CTEM is a mode of operation in TEM where a sample is illuminated with a coherent plane wave. In CTEM, the optical configuration is similar to traditional wide-field light microscopy. In imaging mode, the detector plane is optically coupled with the bottom plane of the sample, projecting the exit electron wave onto a pixelated detector, where the scattered electron intensity is recorded. In this mode, our resolution is limited by the aberrations of the objective lens. Modern systems have an aberration corrector capable of achieving down to 0.5 Å [55,56]. With plane wave illumination, image contrast is caused by variations in the transmitted beam, which can result from absorption, dynamical effects (elastic scattering on a crystalline sample), or phase contrast (interference due to local phase modulation of the electron wave by the sample).

The contrast in images at lower to medium magnifications is mainly due to dynamical effects that result in high-angle scattering (intensity variations). At this magnification level, the electron wave's phase variations can lead to undesired artifacts like Fresnel fringes due to imprecise focusing. However, when aiming for a high-resolution image

⁵In some cases, such as with Nion TEMs, the geometry is inverted. However, this does not apply to the TEM work conducted in this thesis so we will adhere to this convention.

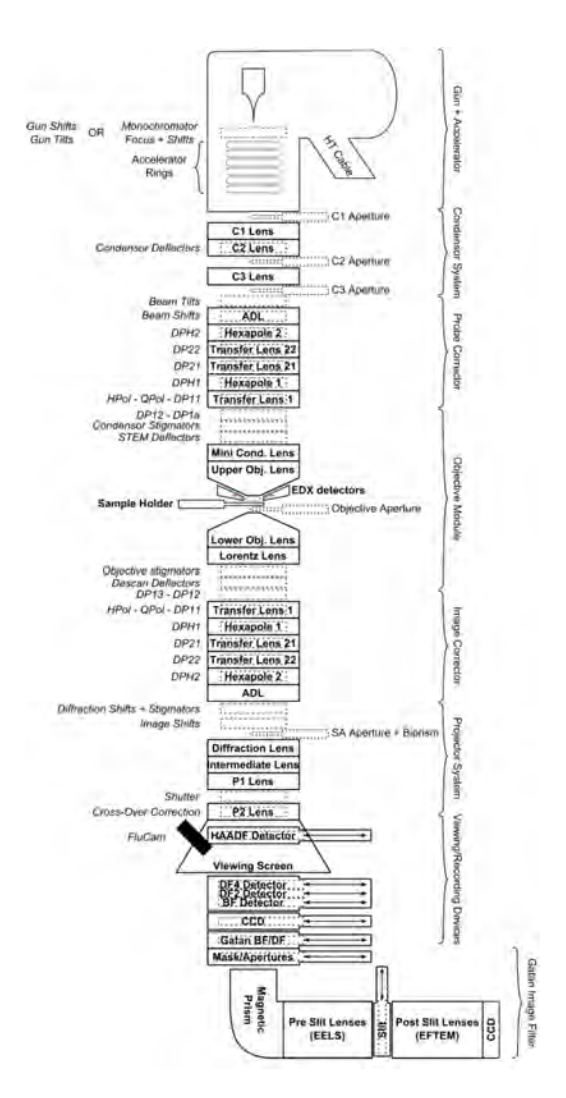


Figure 1.8: Diagram showing the main optical elements of a FEI Titan¹. The diagram labels each component and groups them by modules, whose names are shown with braces on the right. Most of the experimental results contained in this thesis were obtained with this microscope.

(HRTEM), the fine structure of the material comes almost entirely from the phase contrast. For example, when electrons pass through a thin crystal that is oriented with one of its main crystallographic axes aligned with the optical axis, they perceive the positively charged atomic nuclei along the columns as lower energy channels [57,58]. This phenomenon, known as atomic lensing or channeling, results in larger phase differences and improved phase contrast.

The contrast transfer function (CTF) in CTEM can be expressed as follows:

$$CTF(\mathbf{k}) = A(\mathbf{k})e^{i\chi(\mathbf{k})}$$
(1.16)

Where $A(\mathbf{k})$ represents the objective aperture, which is usually a top hat function, and the phase term $e^{i\chi(\mathbf{k})}$ is the aberration function of the spatial frequency \mathbf{k} . In practical terms, the equation for CTF yields that the highest spatial frequency k_{max} is proportional to the numerical aperture. However, as we are aberration-limited, objective lens aberrations will typically hinder the interpretability of the spatial frequencies transferred by the optical system.

Another option in CTEM is to project the exit electron wave onto the momentum space (far-field diffraction). Under this projection condition, we can obtain a diffraction pattern of our sample, which contains information about its crystalline structure.

1.2.2 Scanning Transmission Electron Microscopy (STEM)

In STEM, a sharp electron probe is used to scan the sample, obtaining one intensity measurement per probe position to create an image. STEM has an advantage over CTEM in that, in addition to the elastically (effectively no energy lost) or inelastically (some of the electron energy is exchanged with the sample) scattered electrons transmitted through the sample such as in, e.g., EELS [59], it can also capture other spatially-resolved signals such as characteristic x-rays [60–66], visible light photons (cathodoluminescence) [67, 68], or electrons that originate from the material itself (secondary electrons) [69–71] simultaneously taking advantage of the known position of the electron probe.

In STEM, the electron probe can be understood as the Fourier transform of the condenser aperture, which is usually represented by an Airy pattern. However, in the following chapters, we will explore instances where this is not the case. Furthermore, regardless of the shape of the condenser aperture, aberrations in the condenser lens will distort the STEM probe. This deformation is proportional to the semi-convergence angle (α) for a fixed aberration value. Mathematically, the probe function is expressed as:

$$\psi(\mathbf{r}) = \mathcal{F}\left[A(\mathbf{k})e^{i\chi(\mathbf{k})}\right] \tag{1.17}$$

The term $A(\mathbf{k})$ represents the aperture function, while the phase term $e^{i\chi(\mathbf{k})}$ accounts for the aberrations in the condenser system. Typically, the probe is scanned in a raster pattern across the sample's surface. At the same time, a single-pixel detector collects a signal that is proportional to the number of scattered electrons within its angular range. This single-pixel detector is typically configured as a ring located in the darkfield region (at high scattering angles), which gives this scanning-detection technique its name: High-Angle Annular Dark Field (HAADF) STEM [72–74].

Moreover, it is common practice to adjust the collection angle in the dark field to optimize sensitivity for specific atomic elements [75,76], or even to collect data within the Annular Bright Field (ABF) range [77,78], as the signal received by the detector within a certain angular range is proportional to the scattering cross-section of the atoms in the material, which is generally related to the atomic number (Z) [79,80]. In any case, the collection

 $^{^6}$ Typically, the CTF also includes a term $E(\mathbf{k})$, representing an information envelope containing the spatial and temporal coherence of the wave.

angle of the detector is modified by changing the distance between the detector and the sample using the projector system.

1.2.3 The Point Spread Function and the Reciprocity Principle

If we look closer at equations 1.16 and 1.17, we notice that they have a similar structure, with the main difference being a Fourier transform. This resemblance arises from the fact that the optical configuration of STEM is effectively the inverted version of that found in CTEM. This observation highlights a crucial concept in TEM known as the reciprocity principle [81,82].

In CTEM, we get an image when electrons deposit their energy onto the detector. However, this energy is deposited over a finite area on the detector, leading to the concept of a PSF for the detector. Naturally, if we reduce the width of this PSF, we achieve a higher point resolution. This PSF, which comes on top of the PSF of the optical elements in the microscope, links the physical characteristics of the detector, including thickness and pixel size, to the achievable resolution in CTEM, given that the camera length is fixed.

Conversely, in STEM, the equivalent factors that influence resolution are the probe diameter (our effective PSF in this case) and the scan's step size, as the scattered signal is captured using a single-pixel detector.

In both STEM and CTEM, resolution is linked to the numerical aperture of the system. Users can typically set this aperture within a certain range, but it is often constrained by optical aberrations.

According to the reciprocity principle, enhancing resolution in CTEM requires minimizing the aberrations in the objective lens system and reducing the energy spread of electrons on the detector. In contrast, in STEM, we need to focus on reducing the aberrations in the probe-forming optics of the condenser system to decrease the probe size, while the detection process is more straightforward.

4D-STEM

Recently, there has been increasing interest in alternative setups for STEM. These configurations utilize a pixelated detector to capture the Convergent Beam Electron Diffraction (CBED) pattern. This approach allows us to collect more information with each STEM recording, as the scattering data is resolved in both the real space (sample plane) and reciprocal space (diffraction plane) [83–85]. Although this concept was initially introduced with a different naming convention [83,86], the field has since adopted the more commonly used term 4D-STEM [87].

This 4D dataset allows for increased dose efficiency and resolution through computational imaging reconstruction methods. Still, it comes at the cost of losing the live, straightforward image formation of a HAADF-STEM image. Furthermore, recent research has demonstrated that using 4D-STEM, one can achieve atomic resolution even without an aberration corrector, showing extra robustness to the optical imperfections of the imaging system [88]. It is worth noting that 4D-STEM techniques currently hold

the record for the highest spatial resolution for an image [89, 90], which is superior to the reported values both in CTEM and STEM.

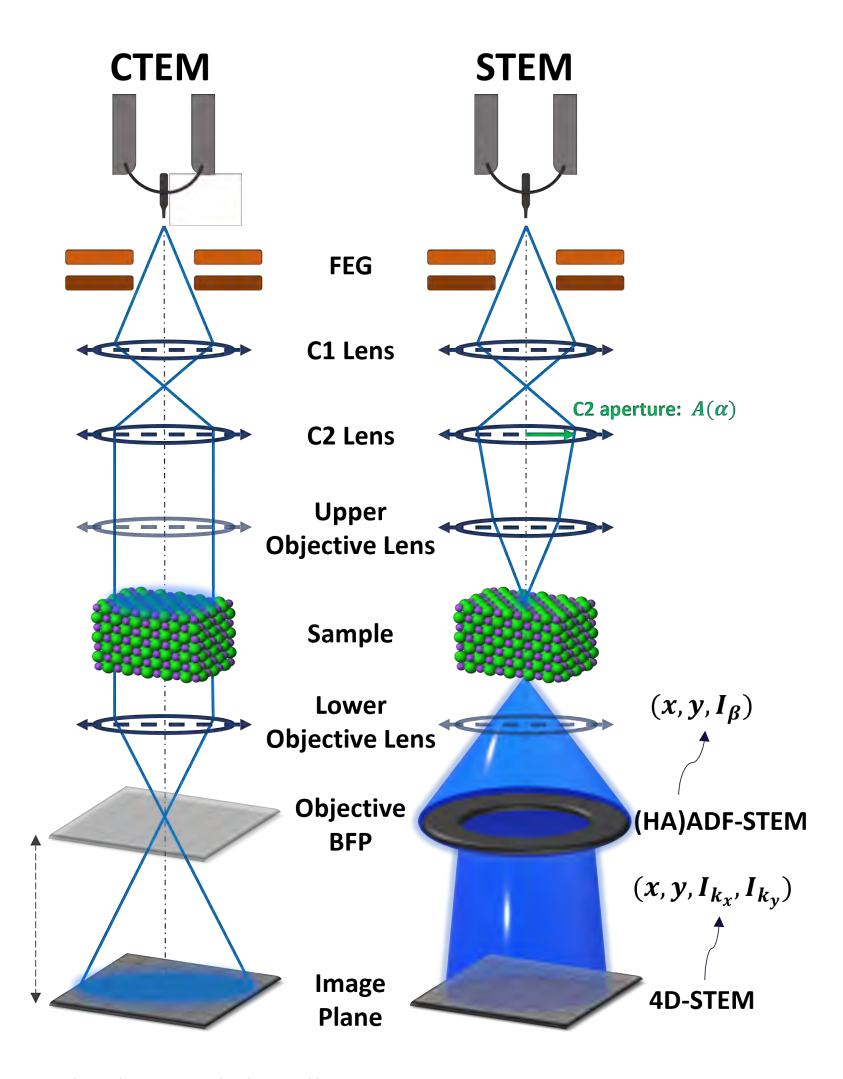


Figure 1.9: The diagram below illustrates TEM's most common operation modes. In addition to adjusting the optical elements above the sample, a projection system (not shown) is typically employed to magnify the image and switch between diffraction and imaging modes. The most frequently used mode for STEM is HAADF, where an intensity signal I_{β} is captured for each probe position (x,y) on the sample plane. More recently, there has been growing interest in 4D-STEM applications, where a pixelated detector in reciprocal space acquires spatially resolved intensity (I_{k_x}, I_{k_y}) . These applications are gaining attention due to their dose efficiency and ability to withstand some optical imperfections in the microscope.

Chapter

Expanding the TEM capabilities: Electron Wavefront Shaping

Contents		
2.1	Electron Wavefront Shaping	23
	2.1.1 The Wave-Particle Duality of Electrons	23
	2.1.2 The Aharonov-Bohm Effect	26
	2.1.3 Phase Plates for Electrons	27
2.2	The landscape for Electron Wavefront Shaping	31

The previous chapter covered the main pieces and operational modes in the TEM. While CTEM and STEM provide critical insights into the structure and properties of materials, they are fundamentally limited by the design of their components. Any electron microscope operates by manipulating the trajectory of electrons traveling from the source to the detector, with a sample placed along this path. This control is achieved by adjusting the electromagnetic fields generated by the TEM's numerous active elements. These fields, in turn, shape the electron wavefront during its propagation through the column, facilitating the interpretation of the signal at the detector. However, wavefront shaping extends beyond electron microscopy, driving advancements across various scientific disciplines.

Wavefront shaping, the ability to spatially and temporally manipulate the phase of coherent waves, has already transformed numerous fields. In radio and light astronomy, wavefront shaping enables adaptive optics to correct atmospheric distortions and achieve high-resolution imaging [91,92]. Similarly, radar systems use it for beam forming and improving signal detection [93]. In acoustics, wavefront shaping facilitates more precise control of sound propagation for applications such as noise control and acoustic imaging [94–96]. Seismology and telecommunications also benefit from wavefront shaping techniques to enhance signal clarity and precision in detecting seismic waves and beam forming for communication networks [97–99].

Given the advancements in these fields, incorporating wavefront shaping into electron microscopy holds significant potential for improving existing techniques in TEM. Furthermore, the versatility of wavefront shaping offers promising avenues for innovation in electron microscopy, suggesting that its potential applications are far from being fully realized.

Implementing wavefront shaping requires devices capable of inducing phase changes in a wave within a specific area. These devices are often paired with automated control systems to achieve desired functions for adaptive wavefront optimization. A classic example of such a device in optics is the spatial light modulator (SLM), which typically features a controllable array of mirrors or a liquid crystal-based system [100–102]. These devices are crucial for precise wavefront control, and their adaptation into electron microscopy could enhance its capabilities significantly.

Fundamentally, every TEM has lenses and deflectors that have some control over the electron wavefront's phase. Nevertheless, this manipulation is often limited by the design of the components, given that:

- Electron lenses, due to their rotational symmetry, are limited to changing their focal point along the optical axis within the TEM's column
- Deflectors are designed to adjust the x-y position of the electron beam, shifting it back to the optical axis or scanning a probe over the sample
- Aberration correctors provide the most versatility in terms of wavefront manipulation. However, they are largely susceptible to mechanical instabilities and are mostly optimized to achieve a stable flat phase profile that minimizes the effect of Seidel aberrations in the lenses.
- Aberration correctors can only apply harmonic phase profiles by precisely controlling the boundary conditions of the fields in the multipoles.

2.1. ELECTRON WAVEFRONT SHAPING

• Aberration correctors and lenses are relatively slow and experience hysteresis, complicating precise automated wavefront control.

In other words, the optical components typically used in a TEM are optimized specifically for CTEM and STEM, and any non-conventional wavefront shaping using these optical elements is subjected to the aforementioned limitations. While there have been efforts to utilize existing technologies, such as aberration correctors, in innovative ways to develop new imaging modes [103–107], we are still far from achieving the versatility and robustness seen in state-of-the-art SLM.

Arbitrary electron wavefront shaping in the TEM is challenging due to several factors. First, manipulating the phase of matter waves is more complex than manipulating photons or acoustic waves, mainly because of the significantly higher energy of the accelerated electrons. Additionally, the physical space constraints within the column and the vacuum requirements necessary to minimize scattering and maintain other optical components (such as the field emission gun and lenses) limit the options for integrating a reliable tool to modulate the electron wavefront.

Despite the challenges, recent developments over the past few decades have successfully integrated some of the SLM capabilities into a TEM. In this chapter, we will provide an overview of the key advancements in adapting the concept of SLM for electron microscopy. Specifically, we will explore the physical principles underlying electron wavefront shaping and highlight the significant developments that lead to today's state-of-the-art devices. Additionally, we will introduce Electrostatic Phase Plates (EPP) for electrons, which are promising candidates for creating a generalized wavefront shaping device in TEM.

2.1 Electron Wavefront Shaping

The modulation of accelerated electrons fundamentally depends on the interaction between the electron wave and an electromagnetic field. This is, in fact, the very principle enabling electron microscopy imaging: as electrons traverse a material, they interact with the electromagnetic fields generated by the atoms within the material, resulting in specific modulations on the electron wave that ultimately reaches the detector. Thus, as electron microscopists, our primary task is to decode the information imprinted onto the electron wavefront by the material we study, revealing its properties. However, in this section, we will not focus on the interactions between the material and the electron wavefront. Instead, our primary focus will be on exploring the physical principles behind electron wavefront modulation and extending them to the design of a programmable device capable of arbitrarily modulating the phase of the electrons inside a TEM.

2.1.1 The Wave-Particle Duality of Electrons

In the previous chapter, we explored the concept of an electron lens from the perspective of classical electrodynamics. In this framework, electrons are viewed as point-charged particles that experience Lorentz forces along their trajectories, which was sufficient

for our discussion. However, as introduced by De Broglie [3], electrons can also be understood as matter waves through a quantum mechanical perspective. From this perspective, their propagation is described by the Schrödinger equation¹:

$$i\hbar \frac{\partial}{\partial t} \Psi(\mathbf{r}, t) = \hat{\mathbf{H}} \Psi(\mathbf{r}, t)$$
 (2.1)

Where \hbar is the reduced Planck's constant, $\Psi(\mathbf{r},t)$ represents the electron wavefunction, and \hat{H} is the energy operator, often referred to as Hamiltonian [112, 113], which is composed by the kinetic and potential energy contributions:

$$\hat{H} = \left(\frac{\hat{p}^2}{2m} + V(\mathbf{r}, t)\right) \tag{2.2}$$

In this context, m represents the relativistically corrected mass of the electrons, and $\hat{p} = -i\hbar\nabla$ is the momentum operator, with $\nabla = \left(\frac{\partial}{\partial x} + \frac{\partial}{\partial y} + \frac{\partial}{\partial z}\right)$.

Additionally, we can state that the fast electrons moving through the microscope's column encounter a time-independent potential, denoted as $V(\mathbf{r})$. Since the relativistic electrons passing through the column *perceive* a snapshot of these fields, we can approximate the entire spatial evolution of the electron wave function from a stationary perspective.

In fact, the fast electrons traveling through the sample spend an extremely short amount of time within the potential field, much shorter than the timescale of the potential's temporal oscillations (such as those caused by vibrating atoms in a crystal lattice). Therefore, we can approximate these potentials as static. To account for the effect of atomic vibrations, we can average over several small, instantaneous displacements of the atomic species. This approach is commonly referred to in the literature as the *frozen phonon approximation* [114,115].

As a result, we can consider the energy E as a constant Eigenvalue of the Hamiltonian. We can then separate the solution of the Schrödinger equation into spatial and temporal components:

$$\Psi(\mathbf{r},t) = \psi(\mathbf{r})e^{-iEt/\hbar} \tag{2.3}$$

Where $\psi(\mathbf{r})$ represents the spatial part of the wavefunction, and the exponential term is a time-dependent phase factor that depends on the energy eigenvalue E of the system's stationary state. As the derivative acts only on the exponential term of Ψ , and the $e^{-iE/\hbar} \neq 0$, we can simplify eq. (2.1) as:

¹In a more rigorous formulation, the propagation of relativistic electrons should be modeled starting from Dirac's equation [108]. Nevertheless, the derivation presented here provides a reasonable approximation for the spatial propagation of electrons in a TEM, as the energies involved in a TEM are well within the predictive range of the Schödinger equation [109,110], including a relativistic correction of the wavelength and mass and assuming that the spin has a negligible role [111].

$$E\psi(\mathbf{r}) = \left[-\frac{\hbar^2}{2m} \nabla^2 + V(\mathbf{r}) \right] \psi(\mathbf{r})$$
 (2.4)

This equation governs the stationary states of a quantum system. It can be used to understand the interaction between the fast electrons in the TEM column and the quasi-static fields generated by the optical elements, external fields, or the sample.

Young's Double Slit Experiment

In the last section, we introduced the wavefunction $\Psi(\mathbf{r},t)$, which describes the quantum state of a particle, such as an electron. The square of the magnitude of this wavefunction, $|\Psi(\mathbf{r},t)|^2$, is the probability distribution for the particle's position at some time t. This interpretation reflects the wave-particle duality of quantum mechanics, a concept that sparked significant debate and controversy in its early days. In this section, we will briefly explore historical aspects and key theories and experiments that helped clarify this debate, allowing us to understand the wave-particle behavior of electrons.

The classical corpuscular theory of light, as described by Newton [116], struggled to explain phenomena such as interference and diffraction. In response, other theories that accounted for the wave-like nature of light, such as Huygens' wave theory [117], gained wider acceptance. A pivotal experiment that helped validate the wave theory of light was Young's double-slit experiment [118]. In this experiment, Young demonstrated that light passing through two narrow slits creates an interference pattern on a distant screen, providing compelling evidence of its wave nature (see fig. 2.1). To follow up, Geoffrey Ingram Taylor conducted an experiment in which the source of light was reduced considerably in size, showing the appearance of interference fringes [119] and leading to a famous statement by Dirac: "Each photon then interferes only with itself" [120].

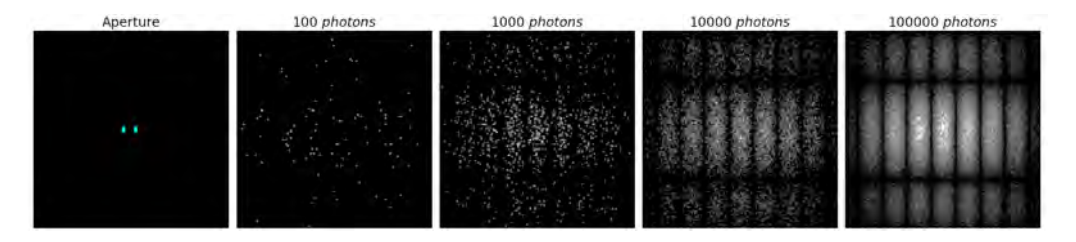


Figure 2.1: Young's double slit experiment simulation: as the number of photon counts increases on the far-field detector, the interference pattern emerges, suggesting the wave-like behavior of light.

Later, the proof of concept for wave-particle duality was extended to matter waves. The first demonstration supporting De Broglie's formulation for electrons was the Davisson-Germer experiment [121], which confirmed that electrons can exhibit diffraction, a phenomenon inherently related to wave interference. Subsequently, Claus Jönsson became the first to replicate Young's double slit experiment using electrons [122]. Following the history of photon double slit experiments, later research by Merli et al. [123] and Tonomura et al. [124] demonstrated the development of interference patterns resulting from single electron events.

2.1.2 The Aharonov-Bohm Effect

After explaining the wave-particle duality of electrons, we can introduce another fundamental concept in quantum mechanics essential for understanding the later chapters of this thesis: the Aharonov-Bohm effect. The Aharonov-Bohm effect demonstrates that electromagnetic potential fields can directly influence charged particles, even when no electromagnetic fields are present [125]. Importantly, this effect highlights that, unlike in classical physics, potentials are not merely mathematical tools; they possess observable significance within the system.

In the presence of a static electromagnetic potential, electrons traversing a region of space where both the electric and magnetic fields are zero may still undergo a phase shift. This shift is proportional to the scalar potential $\phi(\mathbf{r})$ and the vector potential $\mathbf{A}(\mathbf{r})$ present in the surroundings, which are related to the electric and magnetic field, respectively as:

$$\mathbf{E} = -\nabla \phi(\mathbf{r}) - \frac{\partial \mathbf{A}(\mathbf{r})}{\partial t}$$

$$\mathbf{B} = \nabla \times \mathbf{A}(\mathbf{r})$$
(2.5)

$$\mathbf{B} = \nabla \times \mathbf{A}(\mathbf{r}) \tag{2.6}$$

Following the derivation for eq. (2.4), to account for the effect of the scalar potential $\phi(\mathbf{r})$ and the vector potential $\mathbf{A}(\mathbf{r})$ on the spatial evolution of an electron with charge -e, and in the absence of any other potential $V(\mathbf{r})$ we simply need to add a correction to the Hamiltonian such that:

$$\hat{H} = \frac{1}{2m} \left(\hat{\boldsymbol{p}} + e \mathbf{A}(\mathbf{r}) \right)^2 - e \phi(\mathbf{r})$$
 (2.7)

In the presence of static, spatially varying potentials, the solution to the time-independent Schrödinger equation will be modified by a phase factor to account for these potentials:

$$\Psi(\mathbf{r}) = \psi(\mathbf{r})e^{i\Delta\phi_{AB}} \tag{2.8}$$

And the phase factor $\Delta \phi_{AB}$ is given by:

$$\Delta \phi_{AB} = \frac{e}{\hbar} \left(\int_{\Gamma} \mathbf{A}(\mathbf{r}) \cdot d\hat{z} - \int_{\Gamma} \phi(\mathbf{r}) dz \right)$$
 (2.9)

Where Γ is the trajectory of the electron beam in the propagation direction \hat{z} .

From eq. (2.9), we get the local phase shift that the electron wavefront experiences as it traverses a region of space, which is proportional to the strength of the potential fields in that region.

For example, consider a long, thin solenoid that confines a magnetic field B inside it. The magnetic field is zero outside the solenoid, yet the vector potential A extends into the surrounding space. An electron beam split into two paths around the solenoid

2.1. ELECTRON WAVEFRONT SHAPING

can acquire a relative phase shift due to the vector potential alone, which becomes observable when the beams are recombined to form an interference pattern. The phase shift is directly related to the magnetic flux enclosed by the electron paths, and this shift alters the interference pattern, demonstrating that the vector potential exerts a measurable influence (see fig. 2.2 (a)).

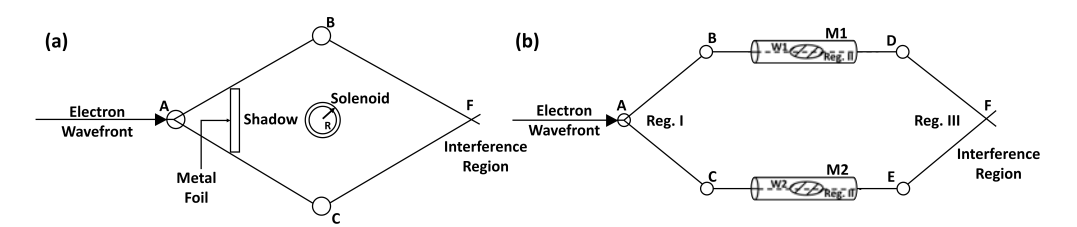


Figure 2.2: Schematics of experiments proposed by Aharonov and Bohm demonstrating interference with a magnetic vector potential (a) and electric scalar potential (b). (a) elements A, B, and C split the electron beam into two paths and interfere at F after being influenced by the vector potential produced around a solenoid. (b) devices A, B, C, D, and E divert and guide wave packets W1 and W2 through cylindrical metal tubes M1 and M2 inside which we apply a scalar potential, resulting in interference at F. Schematics are adapted from Fig. 1 and 2 of Ref. [125].

Alternatively, we can consider an electron wavefront traveling through areas of space that have different scalar potentials. As a result, the interference pattern of the electron wavefront will change due to the phase shifts acquired by the partial wavelets as they encounter varying scalar potentials along their paths (see fig. 2.2 (b)). However, in any practical realization of this effect, it is nearly impossible to create a region along the electron's trajectory that is entirely free of electric fields while maintaining a well-defined scalar potential field. This limitation leads to a quasi-electrostatic interpretation of the Aharonov-Bohm effect.

By combining the concepts from Young's double slit experiment with the electric Aharonov-Bohm phase shift, we can directly observe the variation in the resulting interference pattern. Specifically, we can compare two scenarios: one in which there is no local projected potential (electric scalar potential) and another where one of the slits is subjected to a potential such that $\Phi_{AB} = \pi$. In the latter case, we will see an alteration in the original interference pattern. This change occurs due to the phase acquired by the wavefunction as it passes through the double slit in the presence of a scalar potential, yielding destructive interference in the middle of the pattern, as illustrated in Figure fig. 2.3.

The wave-particle duality of electrons as matter waves, along with Young's double-slit experiment and the Aharonov-Bohm effect will play an important role to understand the theoretical and experimental results that will be discussed throughout this work.

2.1.3 Phase Plates for Electrons

The concept of a phase plate for electrons has been partially discussed throughout this work. Essentially, any optical element positioned along the path of an electron beam functions as a phase plate by altering the field in a specific region along its propagation

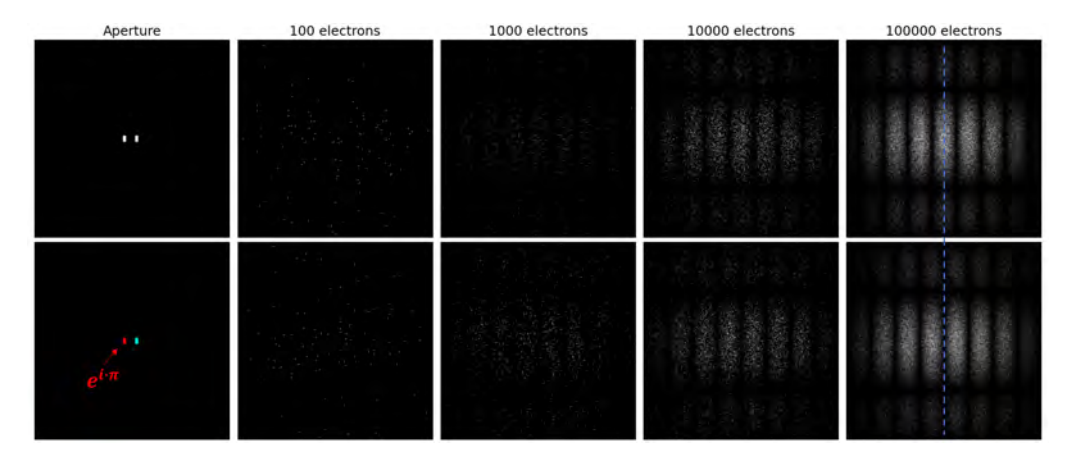


Figure 2.3: Young's double-slit experiment (top) contrasted with a setup where one of the slits is subjected to an electric scalar potential (bottom), resulting in a variation of the interference pattern.

path. This modification effectively introduces a phase term to the solution of eq. (2.1). Therefore, whether we use a traditional electromagnetic lens or a double-slit aperture with a projected potential, we essentially have a phase plate for electrons. In the following section, we aim to explore how to take advantage of the electrostatic Aharonov-Bohm effect further to develop a controllable spatial modulator for the electron wavefront.

2.1.3.1 Single-Element Electrostatic Phase Plates

Börsch introduced the concept of an electrostatic phase-shifting element for electron waves in 1947 [126]. In his design, Börsch relied on the electrostatic Aharonov-Bohm phase shift described in eq. (2.9) to modulate the phase of an electron wavefront locally. Using this principle, an EPP for electrons can adjust the phase shift by modulating an electric field induced by a chosen voltage. Despite the relatively simple concept behind this EPP, Börsch pointed out the technological difficulties of creating such a miniaturized component at that time, which delayed its realization for a few decades. As technology advanced, Matsumoto and Tonomura materialized the idea by developing a miniaturized Einzel lens comprising a biased metal layer between two grounded electrodes, called $\lambda/4$ phase plate [127]. An adaptation of the original schematic by Börsch and the implementation by Matsumoto and Tonomura are shown in fig. 2.4.

Recently, the miniaturized Einzel lens has been employed to create EPPs for electron microscopy, commonly referred to as Börsch phase plates [128,129]. Initially, this concept aimed to adapt the Zernike phase plate [130–132] for use in the TEM to enhance contrast in biological imaging, rather than serving as a generalized wavefront shaping device. When the phase plate lens is positioned in the back focal plane of the objective lens, it shifts the unscattered beam that passes through the active element (see fig. 2.4 (b)). This setup conveniently produces an image of the sample on the image plane, emphasizing the contrast related to the phase shift introduced by the sample. A more detailed analysis of this concept will be presented later in chapter 5.

2.1. ELECTRON WAVEFRONT SHAPING

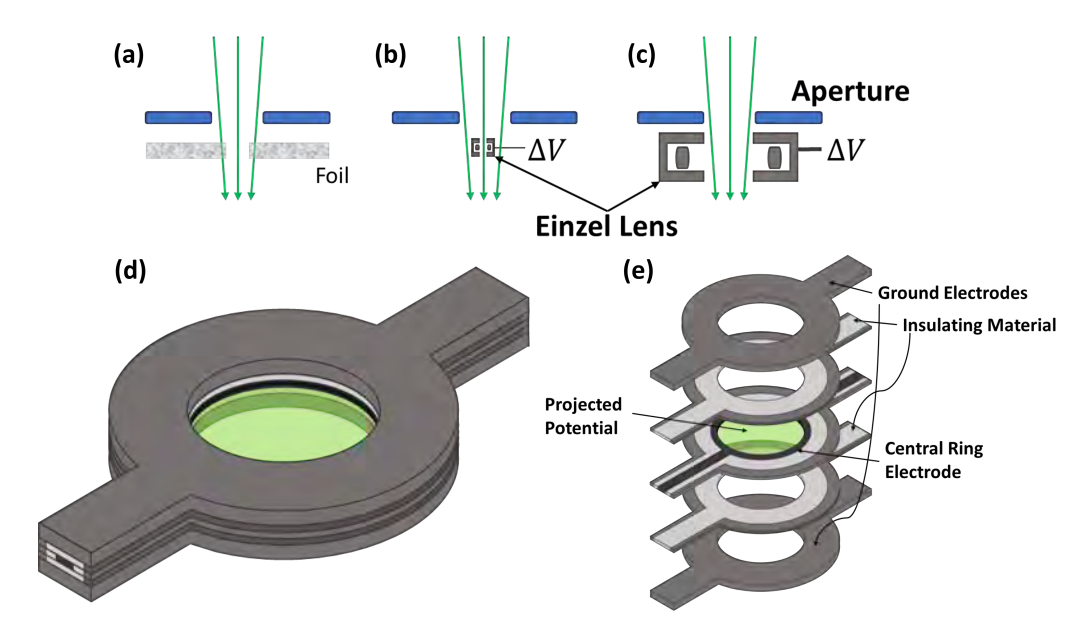


Figure 2.4: Diagram of an electrostatic phase shifting element, as proposed by Börsch, adapted from [126]. Implementations of a Zernike Phase Plate are shown using a thin film (a) and a small Faraday cage (b). A different setup of (b) is shown in (c), where the central and surrounding beams travel inside the cage. The miniaturized realization of Börsch's Einzel lens concept, as demonstrated by Matsumoto and Tonomura, adapted from [127] (d), with a more detailed view of the layers in (e).

One of the first implementations of the Börsch phase plate was conducted by Schultheiss et al. [133], who introduced symmetrical support beams to provide mechanical stability to the device. Several alternative implementations of Börsch phase plates can also be found in the literature [134–136].

Other researchers have investigated EPPs with cylindrical symmetry, taking different approaches. For example, Tamaki et al. proposed a design in which the contact potential of a bimetallic structure serves as the self-biasing element, projecting an electric field into the enclosed region of the device [137].

Some researchers have explored an alternative symmetry involving a layered structure integrated into the objective aperture, forming a protruding beam. This configuration for an EPP is commonly known as a Zach phase plate [138]. In this setup, electrons traveling through the device experience phase shifts corresponding to their distance from the center of the aperture, where the protruding beam is located. This effect is due to the potential gradient generated by this active element. Several studies have highlighted the significant role of the Zach phase plate in phase imaging [139–143].

2.1.3.2 Multi-Element Electrostatic Phase Plates for Electrons

Single-element EPP devices have been implemented and tested in the TEM with partial success. However, they are limited to a narrow angular range (the transmitted beam)

when adjusting the electron wavefronts' phase, which reduces their versatility for more generalized wavefront shaping. To create a more versatile wavefront shaping device closer to the capabilities of an SLM used in light optics, we need to increase the number of individually adjustable phase-shifting elements in the EPP. The multi-element electrostatic EPP consists of an array of Einzel lenses with separate voltage sources. However, achieving this requires fitting all the necessary supports and interconnections for controlling each phase-shifting element into a device small enough to be inserted into a conventional TEM, and these increase with the number of pixels it possesses. However, here we will focus on the general concept, and the practical design details about the device will be discussed later in chapter 3. Despite the technological challenge, the first demonstrations of multi-element EPPs in a standard TEM by Verbeeck et al. showcased a prototype device consisting of 2×2 phase-shifting elements mounted on a Dens Solutions Wildfire in-situ heating chip holder positioned on an especially designed heating chip [144] (see fig. 2.5 (b)). In their work, the EPP's capabilities are tested by generating unique wavefront profiles by changing the potential in each programmable pixel. Furthermore, expanding the concept to a more generalized multi-element EPP was suggested, along with a list of potential applications for them. Similarly, Thakkar et al. presented a three-element multi-layered structure that achieved similar electron wavefront control and provided a detailed description of the manufacturing process [145] and later improvement of it to reduce cross-talk between neighboring pixels [146].

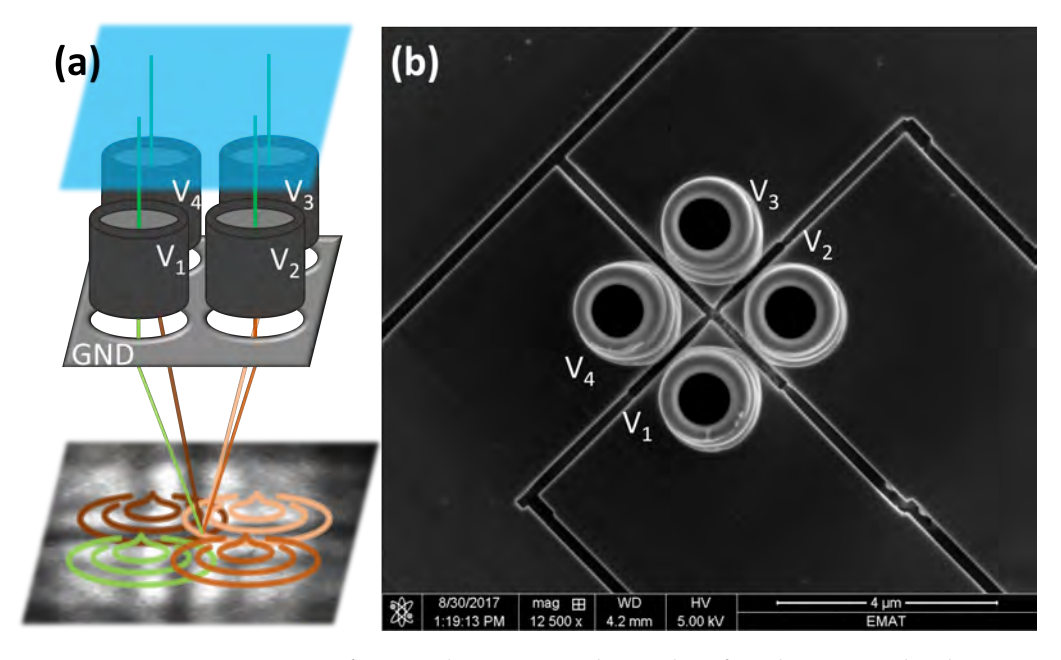


Figure 2.5: Demonstration of a 2x2 Electrostatic Phase Plate for Electrons. The diagram in (a) illustrates the operational principle of the device, where different voltages are applied to each of the individual conductive cylinders. This configuration creates a 4-slit aperture Aharonov-Bohm device. Part (b) presents an SEM image of the device mounted on the Dens Solutions Wildfire in-situ heating chip holder. Figure adapted from [144]

2.2 The landscape for Electron Wavefront Shaping

So far, we have explored how arbitrary wavefront shaping can be achieved, but we have only begun to consider the potential applications and challenges that this development aims to address. For instance, with the increasing use of plasmonic nanoparticles with various shape complexity, phase-modulated illuminations can probe the symmetries of various plasmonic modes through phase-shaped electron energy loss spectroscopy (PSELS) [107,147,148]. Another area that could benefit from electron wavefront shaping is phase retrieval. The long-standing *phase problem* in electron microscopy significantly limits the microscope's ability to find atomic sites in a unit cell, detect light elements without damaging the specimen, or provide high contrast for atomic species with similar atomic numbers. Incorporating phase diversity into the electron beam could enhance information retrieval, resulting in more dose-efficient measurements or improved phase contrast. This topic will be discussed in detail in chapter 5.

Electron microscopes encounter several challenges, including the need for highly trained operators and expensive components. Moreover, some electron microscopy experiments, such as tomography, could take significant time and effort to yield usable data. Like SLM in light optics, electron wavefront shaping presents a promising solution. Adaptive EPPs could facilitate automated measurements, enhance aberration correction, and offer a versatile alternative to some of the current electron microscope modules, as we will cover in chapter 3 and chapter 4.

Within the scope of all concepts presented in this chapter, the main objective of this thesis is to explore the potential application of wavefront shaping in electron microscopy. For that, we will subdivide this exploration into three main topics:

- If we want to correct for aberrations in the TEM, how can we design an EPP to achieve this? Additionally, how can we connect existing and emerging technologies to reach this objective?
- What is the behavior and performance of the latest state-of-the-art EPP, and how effectively can it be integrated with traditional TEM operation modes?
- What are the ultimate limits of electron wavefront shaping, and how do they compare with the field's golden standards?

Furthermore, we will provide a comprehensive overview of the technology from an end-user's perspective, highlighting its ease of operation and seamless integration into various microscopy setups. Lastly, we will summarize this thesis's key findings and discuss the challenges and engineering obstacles that must be overcome to harness this technology's potential fully.

CHAPTER 2. EXPANDING THE TEM CAPABILITIES: ELECTRON WAVEFRONT SHAPING

Chapter 3

Designing an Electrostatic Phase Plate for Aberration Correction

This chapter is based on:

Vega Ibáñez, F., Béché, A., & Verbeeck, J. (2023). Can a programmable phase plate serve as an aberration corrector in the transmission electron microscope (TEM)? Microscopy and Microanalysis, 29(1), 341-351.

Contents

3.1	Introduction	ŀ
3.2	Methods	;
	3.2.1 Electron Beam Parameters to be Optimized	;
	3.2.2 Phase Plate Design Parameters	<u> </u>
	3.2.3 Phase Plate Pixel Pattern	3
3.3	Results	l
3.4	Discussion	ŀ
3.5	Conclusion	7

Summary

The recent advancements in programmable electrostatic phase plates allow us to explore their potential applications. In this chapter, we examine various designs for phase plates with the specific aim of correcting spherical aberration in TEM. Through numerical analysis, we investigate whether a phase plate could achieve spatial resolution as fine as 1 Ångström on a standard uncorrected TEM. We assess some design aspects, such as fill factor, pixel pattern, and symmetry, to understand their impact on the electron probe size and current density. Our findings suggest that certain proposed designs can produce a probe size as small as 0.66 Å, indicating the potential for correcting spherical aberration beyond the 1 Å limit using a programmable phase plate composed of an array of electrostatic phase shifting elements.

3.1 Introduction

As previously discussed in section 1.1.2, the development of the aberration corrector, originating from the Haider-Rose-Urban project [40–42], represents one of the most significant breakthroughs in electron microscopy. Interestingly, inspired by what has been discussed throughout this work, we can describe the aberration corrector as a combination of optical multipoles that apply a *phase plate* to the electron wavefront, compensating for the aberrations caused by spherical electromagnetic lenses.

In this section, we build upon the concepts discussed in chapter 2 to explore a novel method for correcting optical aberrations. Our main focus is on third-order spherical aberration (C_s), as lower-order aberrations can typically be managed using relatively simple components like stigmators, deflectors, or lenses. In contrast, correcting C_s poses a greater challenge and was the primary objective of the first aberration corrector project. To tackle this issue, we draw inspiration from SLMs and propose the design of an array of electrostatic Einzel lenses. This array aims to apply a position-dependent phase shift to the coherent electron wavefront.

The concepts and reasons why a programmable phase plate is attractive for electron microscopy have been discussed briefly in chapter 2. Following this interest, several groups have explored different means to achieve similar freedom in phase shaping of electron beams using miniaturized multipolar lenses [149], interaction with optical near fields [150–154], electrostatic nanofabricated elements applying a projected potential to a region of free space [133,140,155–157], and many others to be discussed in later chapters.

In this chapter, we have chosen a technological approach that builds upon the proof of concept established first by Matsumoto and Tonomura [127], and then extended to multiple phase pixels by Verbeeck et al., as detailed in section 2.1.3.2 and illustrated in fig. 2.5. We will evaluate whether an array of electrostatic phase shifters can function effectively as a C_s corrector for TEM. Demonstrating the feasibility of this solution would allow for the integration of a small device into the TEM column with minimal alterations to its existing configuration. Additionally, it would provide a rapid response tool that can auto-tune and address instrument or specimen-induced drifts when combined with adaptive algorithms. This capability could streamline experiments and improve dose

efficiency, which will be discussed in later chapters of this work.

As simple as the idea may sound, the devil is in the details, and this chapter attempts to give an overview of the design parameters that have to be balanced between manufacturability and expected performance to evaluate whether aberration correction with a programmable electrostatic phase plate could have a future in TEM.

3.2 Methods

Electron Beam Parameters to be Optimized 3.2.1

In order to evaluate different designs for programmable phase plates, we need to first agree on the beam parameters to optimize. For aberration-corrected STEM, we are interested in spatial resolution and current density in the electron probe. It is convenient to determine the spatial resolution by using the d_{50} metric, defined as the real-space diameter containing 50% of the probe intensity [158]. This definition closely relates to the full width at half maximum (FWHM) for very sharp beams. However, it also has the added benefit of taking into account the influence of scattered current in the outer regions of the electron probe, known as beam tails. For the case of current density, we assume that the phase plate is coherently illuminated with a uniform incident beam. This would result in a total probe current of I_0 if a circular aperture, matching the total diameter of the phase plate, were used instead. As the electrostatic phase plate will block part of this beam inherent to the construction of the segments making up for it (sketched in fig. 3.1), we get that the beam current with the phase plate is $I' = I_0 \zeta$ with ζ the fill factor of the specific phase plate. Ideally, this fill factor should be as close to 1 as possible, meaning no blocking of the electron beam, but practical design constraints will determine what is realistic to achieve.

The average current density, J_{50} , in the d_{50} probe diameter is then given as:

$$J_{50} = \frac{4\zeta I_0}{\pi d_{50}^2} \tag{3.1}$$

In comparison, for an ideal aberration-corrected system with circular aperture and convergence half angle α , this becomes:

$$d_{50,ideal} \approx 0.514 \frac{\lambda}{\alpha}$$

$$J_{50,ideal} \approx 15.152 \frac{I_0 \alpha^2}{\pi \lambda^2}$$

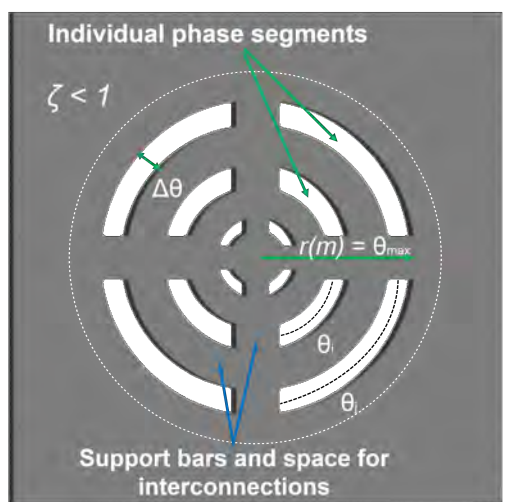
$$(3.2)$$

$$J_{50,ideal} \approx 15.152 \frac{I_0 \alpha^2}{\pi \lambda^2} \tag{3.3}$$

Note that in this theoretical design exercise, we ignore other contributions to experimental probe broadening, such as those caused by source size [159], vibrations, sources of electronic noise, thermal drifts, or chromatic aberrations that could affect the final probe size [160].

To keep the arguments as general as possible, we focus on high-level design parameters and avoid going into details and technical challenges arising from manufacturing.





Conventional round aperture

Programmable pixelated phase plate

Figure 3.1: Sketch of a conventional round aperture versus an array of phase-shifting elements occupying a similar area as in the round aperture case. Parameters such as fill factor (ζ) and angular range ($\Delta\theta$) are indicated along with the relation between maximum aperture (θ_{max}) and radius (r(m)). We show where the interconnections and supports are allocated in the aperture, thus reducing the fill factor.

3.2.2 Phase Plate Design Parameters

After listing the probe parameters we aim to study and optimize, we will now provide insight into some phase plate design considerations to achieve probe size reduction and increase current density. We want to pay special attention to the number of phase-shifting elements, their width, and the percentage of the aperture they will block (all correlated through the interconnections that deliver the bias to each element). A simple rule of thumb is that more segments come with more interconnections, thus blocking more of the incoming electron beam. However, as mentioned before, we will discuss the mathematical implications of the design choices for the phase plate segments, leaving the manufacturing of the phase plate itself out of the scope of this study.

3.2.2.1 The Role of the Fill Factor

As mentioned above, adding material to the beam's path is inevitable if we aim to break the symmetry constraints imposed by the Maxwell equations on fields in free space, which leads to the concept of the fill factor (ζ). This modulation of the local amplitude of the electron beam will inevitably lead to a broadening of the probe as long-range tails are introduced.

If we try to estimate this effect, we can begin with a wavefunction on the probe forming

aperture with a constant amplitude:

$$\psi_{in}(\mathbf{k}) = \frac{1}{\sqrt{A}} a(\mathbf{k}) e^{i\phi(\mathbf{k})}$$
(3.4)

With $a(\mathbf{k})$ a function defining the aperture's shape being either 1 ($\mathbf{k} < \alpha$) or 0 ($\mathbf{k} > \alpha$), $A = \int a(\mathbf{k})d^2\mathbf{k}$ is the total area of the aperture, ϕ the local phase, and \mathbf{k} a vector in the aperture plane. The wavefunction in real space then becomes:

$$\Psi(\mathbf{r}) = \int \psi_{in}(\mathbf{k})e^{i\mathbf{k}\cdot\mathbf{r}}d^2\mathbf{k}$$
 (3.5)

We consider as the ideal case a circular aperture and a flat phase (i.e., the diffraction limit). In this case, the probe will be the sharpest and the wave will have a value at the central point:

$$\Psi_{ideal}(0) = \frac{1}{\sqrt{A}} \int a(\mathbf{k}) d^2 \mathbf{k} = \sqrt{A}$$
 (3.6)

Now, suppose we want to describe the situation of a pixelated phase plate with the same outer dimensions. In that case, we can put a mask M over the ideal aperture, which is either 1 (electron transparent) or 0 (not electron transparent). Again, we assume the ideal case where the pixelated phase plate can still provide a flat phase in those areas where the plate is electron transparent, we get:

$$\psi_{pp}(\mathbf{k}) = \psi_{in}(\mathbf{k})M(\mathbf{k}) \tag{3.7}$$

This mask changes the maximum of the real space wave function to:

$$\Psi_{pp}(0) = \sqrt{A}\zeta\tag{3.8}$$

With $\zeta = \int \frac{M(\mathbf{k})}{a(\mathbf{k})} d^2\mathbf{k}$ the fill factor of the phase plate.

Now, let us consider the resulting probe, which consists of the sum of the ideal corrected wave and an unwanted tail part:

$$\Psi_{vv}(\mathbf{r}) = \zeta \Psi_{ideal}(\mathbf{r}) + \Psi_{tails}(\mathbf{r}) \tag{3.9}$$

Where ζ describes the scaling of the central maxima with respect to the ideal corrected case. We can now write the intensity of the probe as:

$$I_{pp}(\mathbf{r}) \approx \zeta^2 I_{ideal}(\mathbf{r}) + I_{tails}(\mathbf{r})$$
(3.10)

With any given intensity being $I_i = |\Psi_i|^2$, and assuming that the current of the tails does not overlap with the central spot. This assumption is reasonable given that the ideal probe is a maximally compact function near the center, and the tails come from the high spatial frequencies of the mask, which are much smaller than the total aperture radius.

If we normalize the total current illuminating the round aperture $I_{ideal,total} = I_0 = 1$ for simplicity, the total intensity in the probe then becomes:

$$I_{tot,pp} \approx \zeta^2 + I_{tot,tails}$$

$$\zeta \approx \zeta^2 + I_{tot,tails}$$

$$I_{tot,tails} \approx \zeta(1 - \zeta)$$
(3.11)

If we normalize the tails relative to the total intensity in the probe, we get:

$$I_{tot,tails,rel} \approx 1 - \zeta$$
 (3.12)

In other words, the unwanted tail part of the probe formed by a pixelated phase plate scales approximately as $1-\zeta$, as illustrated in fig. 3.2. These tails will form a low-resolution background signal to any scanned probe setup. This background is undesirable for most conventional imaging methods, such as HAADF-STEM, because it increases counting noise. Additionally, these tails are particularly problematic for spectroscopic methods as they introduce counts from electrons situated away from the probe center. To prevent these tails, we want to create a mask with the highest possible fill factor. For the same reason, to optimize the value of d_{50} , we need a $\zeta>0.5$, and the ideal case would be to bring this value as close to 1 as possible. Cutting off the tails with an aperture placed lower in the TEM column could be another option, but this would require cutting apertures with an equivalent real space diameter only slightly larger than the probe size, which seems extremely difficult to obtain if we aim for Å probes, especially when considering that working in another (magnified) plane than the sample plane will introduce inevitable lens aberrations.

3.2.3 Phase Plate Pixel Pattern

In order to best compensate for the lens aberrations in a pixelated phase plate, it is important that each phase-changing segment can locally correct for the phase error of the other lenses in the microscope as well as possible. This will naturally lead to pixel patterns that mimic the aberration function's symmetry. Starting from the aberration function $\chi(\theta)$ and considering only the defocus $C_1 = (\Delta f)$ and $C_3 = C_s$ terms, eq. (1.15) becomes:

$$\chi(\theta) = \frac{\pi}{\lambda} \left[-\Delta f \theta^2 + \frac{C_s}{2} \theta^4 \right]$$
 (3.13)

We now look for the highest angle that still can be corrected by a segment in the phase plate, and we assume a cylindrically symmetric set of segments covering an angular range between θ_i and θ_{i+1} . A second-order Taylor expansion of the aberration function around θ_i leads to:

$$\chi|_{\theta_{i}}(\Delta\theta) \approx \frac{\pi}{\lambda} \left[-\Delta f \theta_{i}^{2} + \frac{C_{s}}{2} \theta_{i}^{4} \right] + \frac{2\pi}{\lambda} \left[-\Delta f \theta_{i} + C_{s} \theta_{i}^{3} \right] \Delta\theta + \frac{\pi}{\lambda} \left[-\Delta f + 3C_{s} \theta_{i}^{2} \right] \Delta\theta^{2} + \dots$$
(3.14)

3.2.3.1 Zeroth-Order Phase Correction

Suppose we use a zeroth-order phase plate, producing a constant phase shift which is programmable per segment. If we allow for a maximum phase error ϵ within each segment, we get the maximum angle up to which we can correct:

$$\chi|_{\theta_i}(\Delta\theta) < \epsilon \tag{3.15}$$

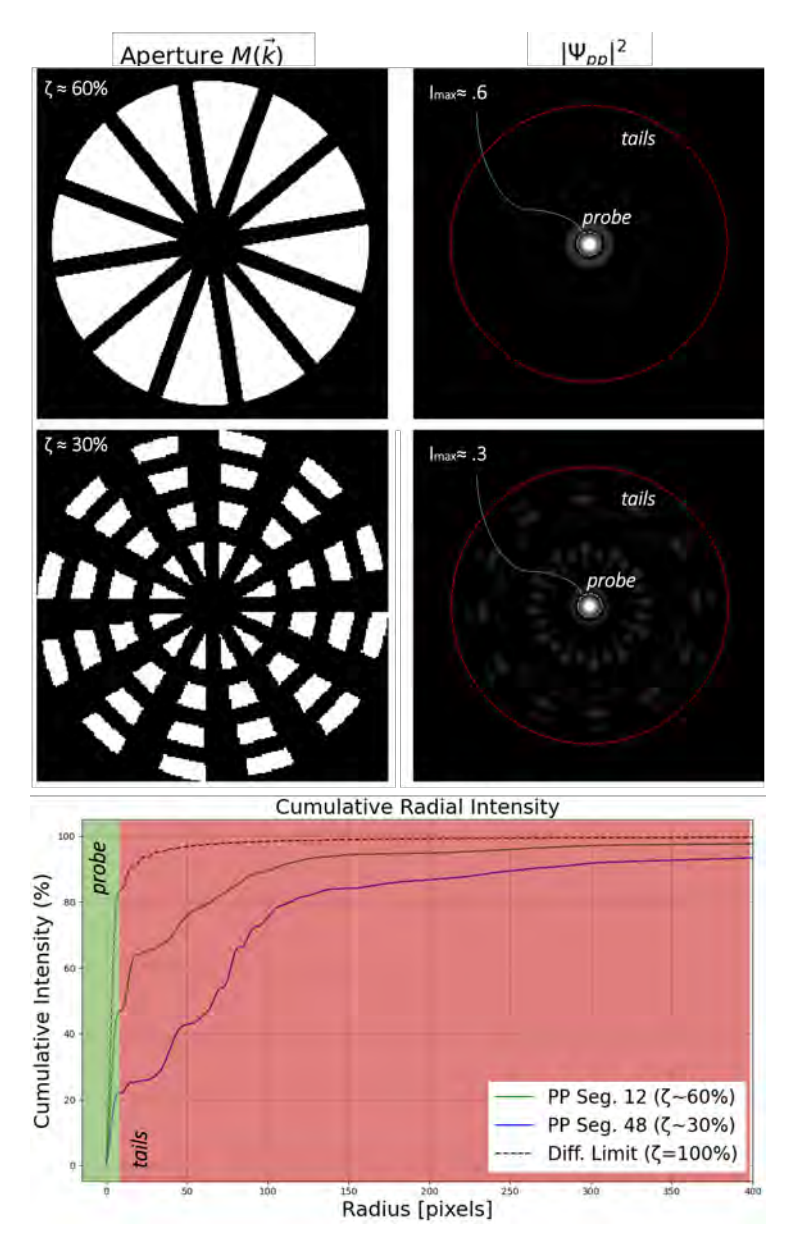


Figure 3.2: Representation of the effect of the Fill Factor (ζ) on probe intensity. Due to the amplitude modulation, the resulting probe intensity, represented as $|\Psi_{pp}|^2$, will have a portion of its intensity in the central lobe, with maximum intensity (I_{max}) proportional to ζ . The contrast of the probe arrays shown on the right has been adjusted arbitrarily to enhance the visibility of the much lower-intensity tails. Additionally, a cumulative integrated intensity is shown below. The shaded areas roughly indicate the *wanted* sharp probe section (green) and the *unwanted* longer-range tails (red), with a diffraction-limited probe shown in black for comparison.

$$\frac{\pi}{\lambda} \left[\left(-2\Delta f \theta_i + 2C_s \theta_i^3 \right) \Delta \theta + \left(-\Delta f + 3C_s \theta_i^2 \right) \Delta \theta^2 \right] < \epsilon \tag{3.16}$$

This puts an upper limit on the maximum angle that can be corrected depending on how small we can make $\Delta\theta$. If we assume only C_s needs correction, we can choose $\Delta f = 0$, and consider the first-order Taylor expansion to be sufficient. We then get:

$$\Delta \theta < \frac{\epsilon \lambda}{\pi 2 C_s \theta_i^3} \tag{3.17}$$

For a typical $C_s = 1$ mm, θ_i =15 mrad, and $\epsilon = 2\pi/10$, we obtain a $\Delta\theta < 58\mu rad$. This would require feature sizes of the segments of only 0.3% of the total aperture diameter and could become rather difficult to manufacture. Alternatively, we can express the maximum angle for a given minimum size of $\Delta\theta$:

$$\theta_{max} < \left(\frac{\epsilon \lambda}{2\pi C_s \Delta \theta}\right)^{\frac{1}{3}} \tag{3.18}$$

This leads to 5.8 mrad for $\Delta\theta = 1$ mrad, giving us the maximum aperture angle we can correct with a flat phase within the given error ϵ .

3.2.3.2 First-Order Phase Correction

If, on the other hand, we allow for first-order correction in each phase segment, meaning a linear projected potential ramp in the radial direction and thus requiring at least two independent potential electrodes per segment, the situation changes. In this case, the phase could be corrected up to the first order, and we get the phase error:

$$\chi|_{\theta_i}(\Delta\theta) < \epsilon \tag{3.19}$$

$$\frac{\pi}{\lambda} \left| \left(-\Delta f + 3C_s \theta_i^2 \right) \right| \Delta \theta^2 < \epsilon \tag{3.20}$$

$$\frac{\pi}{\lambda} \left| \left(-\Delta f + 3C_s \theta_i^2 \right) \right| \Delta \theta^2 < \varepsilon$$

$$\Delta \theta < \sqrt{\frac{\varepsilon \lambda}{\pi (\Delta f + C_s 3\theta_i^2)}}$$
(3.20)

For simplicity, we choose $\Delta f = 0$, which yields:

$$\Delta\theta < \sqrt{\frac{\epsilon\lambda}{3\pi C_s \theta_i^2}} \tag{3.22}$$

For a typical $C_s = 1$ mm, θ_i =15 mrad and $\epsilon = 2\pi/10$, we get $\Delta\theta < 0.76$ mrad which is ≈13 times larger as compared with zeroth-order correction. Following the steps of the previous section, we can express the maximum angle for a given minimum size of $\Delta\theta$:

$$\theta_{max} < \sqrt{\frac{\epsilon \lambda}{3\pi C_s \Delta \theta^2}} \tag{3.23}$$

This leads to 11.46 mrad for $\Delta\theta$ = 1 mrad, nearly double its zeroth-order counterpart.

We give a simplified sketch of the main building blocks needed to make up for both a zeroth- and first-order phase-shifting elements in fig. 3.3. Furthermore, we show a plot of eq. 3.17 & eq. 3.22 in fig. 3.4 for two different phase errors ϵ . To put this into perspective, we give the resolution ranges for some manufacturing techniques (shaded regions).

In order to translate the previous results to meters, we can take a scaling factor to relate angle (mrad) and physical distance (meters), assuming that the widest area we can coherently illuminate is in the order of $100\mu m$ (so, despite the maximum aperture angle θ , we still illuminate the same area in meters). With this in mind, and looking at the right axis scale on fig. 3.4, we can get a value for the physical dimension corresponding to the minimum $\Delta\theta$ needed to keep the phase error under a specific error (ϵ).

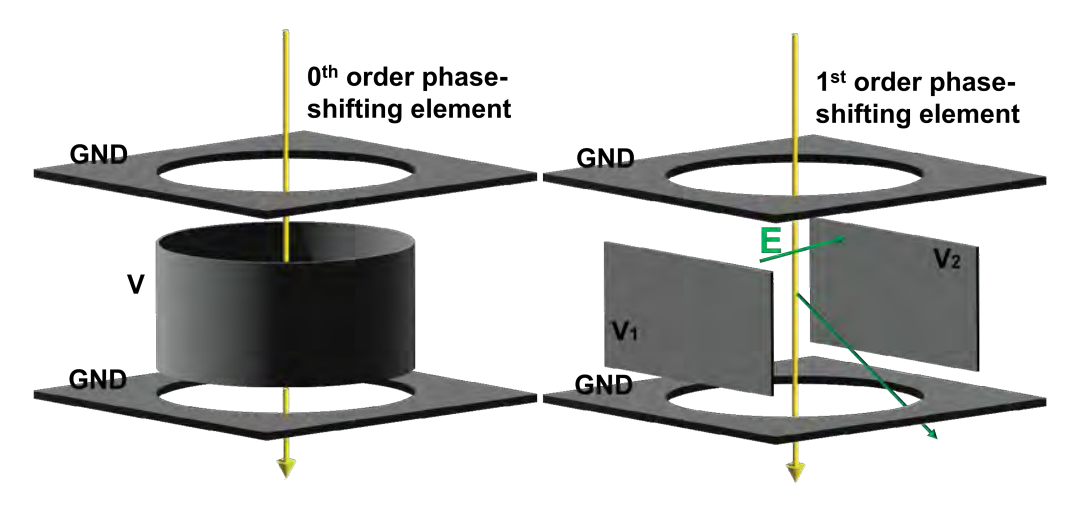


Figure 3.3: Sketch of zeroth- and first-order phase element as the main building blocks of an array of programmable phase-shifting segments.

3.3 Results

Integrating the design rules discussed above, we numerically simulated a set of different electrostatic phase plate designs to test their capabilities to correct C_s at 300 keV with two approaches: (1) applying constant phase shift (zeroth-order) and (2) a combination of constant and linear ramp shift (first-order) segments. As C_s is rotationally symmetric, the proposed designs all consist of concentric rings to make maximum use of the symmetry of the problem.

For reference, these proposed concentric segments shown in fig. 3.5 (a-d) are analogous to those labeled in fig. 3.1 as *individual phase segments*, with the only difference being that we reduce the spacing between segments arbitrarily for our study, and their working principle is the same as the one sketched in fig. 3.3.

After some design iterations, we narrowed down the study to compare three apertures: zeroth-order concentric rings (fig. 3.5 b), a hybrid design (fig. 3.5 c), and a simplified version of the latter (fig. 3.5 d). We show the resulting probe profiles from the apertures in fig. 3.5 (i). This figure shows how the probe from all proposed designs approaches that of a corrected instrument, visibly improving over a non-corrected instrument. It should be mentioned that fig. 3.5 (i) only gives a view of an azimuthally integrated

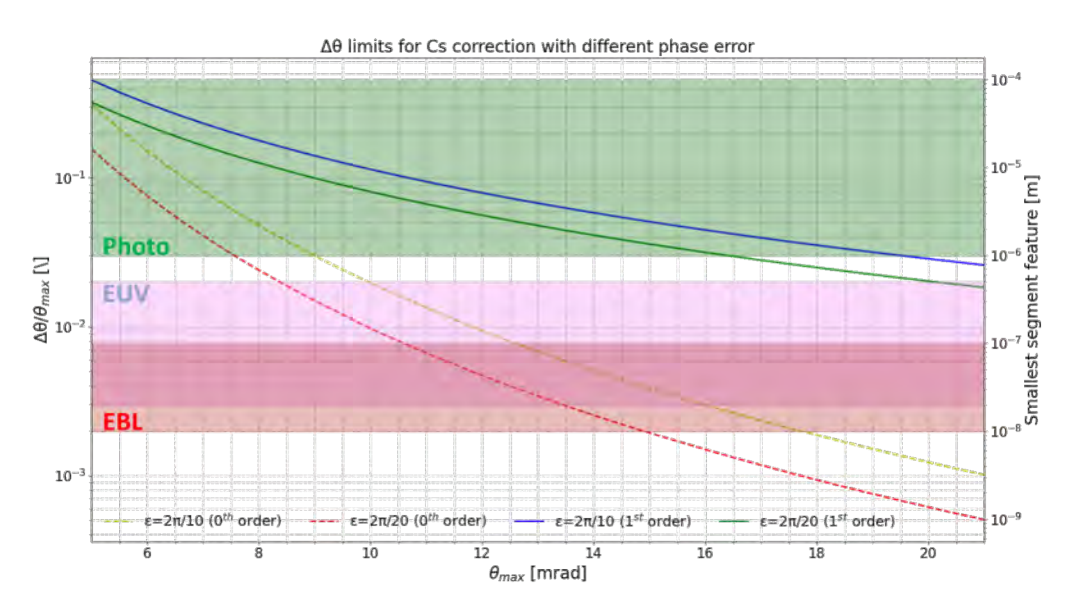


Figure 3.4: Minimum $\Delta\theta$ needed to correct for C_s as a percentage of the total aperture for different phase errors ϵ (left axis, log scale). These can be translated to minimum segment feature sizes when assuming a total aperture diameter of 70 μ m (right axis). The shaded regions (green, violet, red) show the approximated region where photolithography, extreme ultraviolet (EUV) lithography, and electron beam lithography (EBL) would be required to make such features [161].

intensity which is normalized to the maximum intensity of each probe for scale (y-axis) and shows only the tails of the lower spatial frequency features (x-axis).

The fill factor (ζ) displayed in fig. 3.5 was calculated by counting the number of pixels in the matrix with a value different than 0 and dividing it by the total number of pixels a round aperture with the same radius will have. Furthermore, the spacing between holes shown in fig. 3.1 is arbitrarily reduced for simplicity.

The calculated probe size (d_{50}) for the different proposed designs is shown in fig. 3.6, under optimal conditions (i.e., Scherzer's defocus). The d_{50} value is thus simulated for each of the plates, with an increasing opening angle. We find that all the proposed designs offer some C_s correction. However, the linear phase profile obtained by applying first-order correction can keep the phase relatively flat for higher opening angles, further reducing the probe size. More specifically, we reach a d_{50} value of 0.93Å at 15 mrad for the zeroth-order phase plate, a d_{50} of 0.66Å at 21 mrad for the hybrid design and a d_{50} of 0.75Å at 18 mrad for the simplified hybrid design. These values represent a 40%, 57%, and 52% improvement in spatial resolution, respectively, compared to a non-corrected instrument. At higher opening angles (i.e., larger than 21 mrad), we must reduce the width of the segment to reduce the phase error, and this will eventually become an issue for fabrication.

The relative current density can be calculated from eq.3.1 and is plotted in fig.3.7 assuming $I_0 = 50$ pA, all the proposed designs increase this value. More specifically, 6.4x for the zeroth-order phase plate, 28x for the hybrid phase plate shown, and 16.4x for the

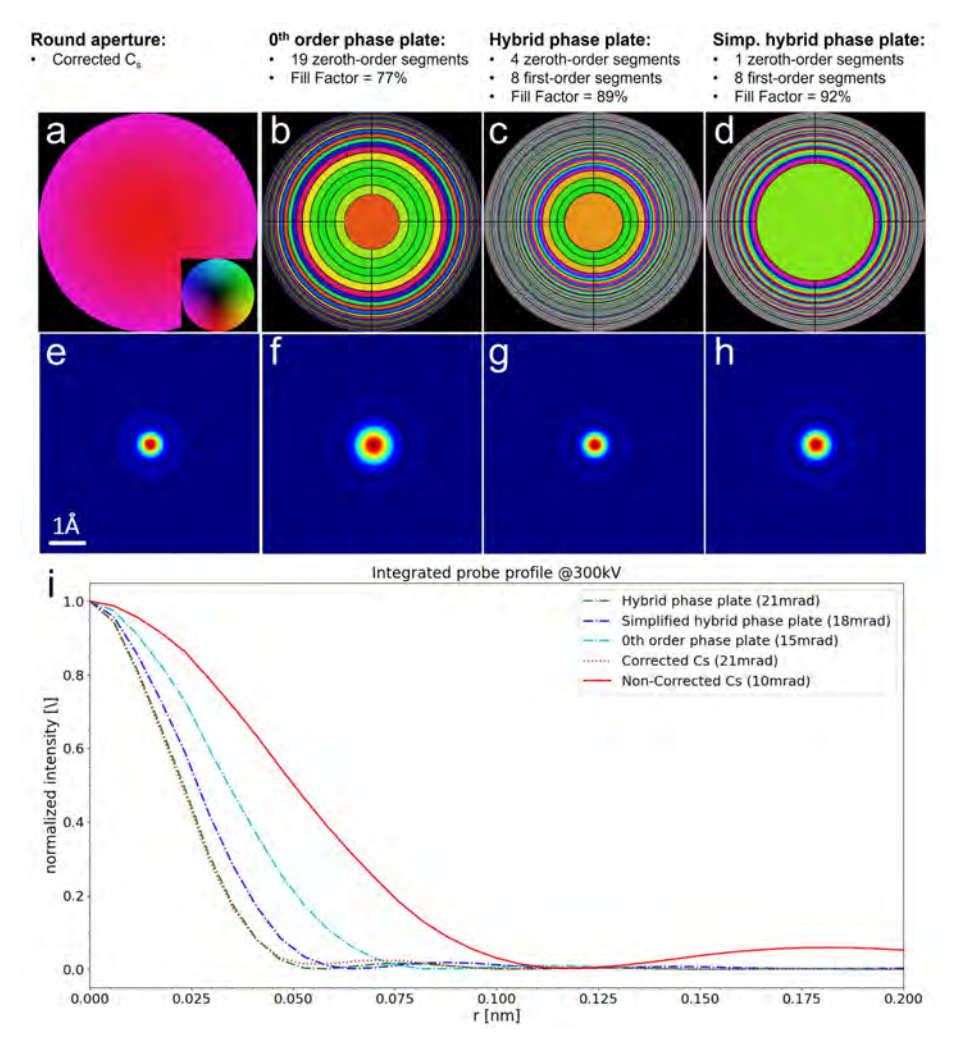


Figure 3.5: Simulated performance of different apertures at 300 keV. (a) The aberrations over a corrected round aperture at 21 mrad with $C_s = 1 \mu m$ and Scherzer's defocus. The aberrations for (b,c,d) are 1.2 mm C_s with Scherzer's defocus as well. (b) A zeroth-order phase plate with 19 segments and $\approx 77\%$ fill factor at 15 mrad opening angle, (c) and (d) hybrid correction phase plates with four central zeroth-order segments followed by eight first-order segments and $\approx 89\%$ fill factor at 21 mrad in the case of (c), and one central zeroth-order hole followed by eight first-order segments and $\approx 92\%$ fill factor at 18 mrad for (d). (e-h) The simulated probe intensities below the corresponding phase plate responsible for them; the simulation box is 6x6Å. (i) A radially integrated profile for each of the abovementioned figures. The proposed alternatives improve the spot size compared with the aberrated instrument. However, it is important to mention that the feature size of the smallest segment in (b) is $\approx 270nm$, whereas the hybrid plates' segments are $1.5\mu m$ wide. The color wheel inset in (a) shows the scale used to represent both phase (hue) and amplitude (intensity).

simpler hybrid design, compared to a non-corrected round aperture at 10 mrad. This relative current density is highly important for, e.g., spectroscopic methods where the increased current in a small probe can lead to a vastly improved signal-to-noise ratio on top of the gain in spatial resolution.

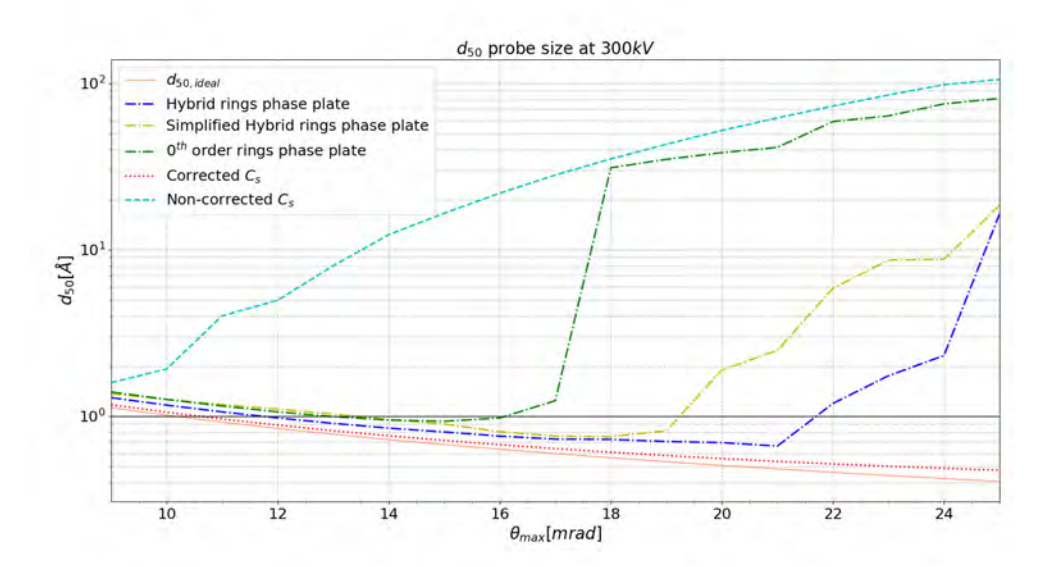


Figure 3.6: Simulated probe size d_{50} assuming 300 keV, C_s = 1.2 mm, and Scherzer defocus for the phase plates and non-corrected aperture. The black line shows the 1Å limit. All proposed phase plate designs are capable of a probe size below this limit (blue, yellow, green lines). However, they are still outperformed by a multipole corrector (red line).

3.4 Discussion

This design exercise shows that having an adaptive phase plate in the condenser aperture plane can correct C_s . Not only did we numerically obtain a probe size below the 1Å limit, but we also increased the relative current density more than 20x. However, implementing a tool like the one proposed in this study poses several challenges. The most critical issue is the possibility of manufacturing a device with all the necessary electrical connections to control each phase segment separately. As the aperture angle increases, we quickly reach regions of rapid changes in the aberration function. This then requires narrower segments to keep the phase error within a reasonable range. However, reducing the segment size or going from zeroth-order segments to first-order segments will increase the number of interconnections needed to control such implementation, ultimately reducing the attainable fill factor.

We show the relation between probe size (d_{50}) and fill factor (ζ) in fig. 3.8. We can observe how the probe size for a plate with a ζ < 0.5 cannot even match the performance of a non corrected instrument in terms of d_{50} for small angles. Nevertheless, at angles > 11 mrad,

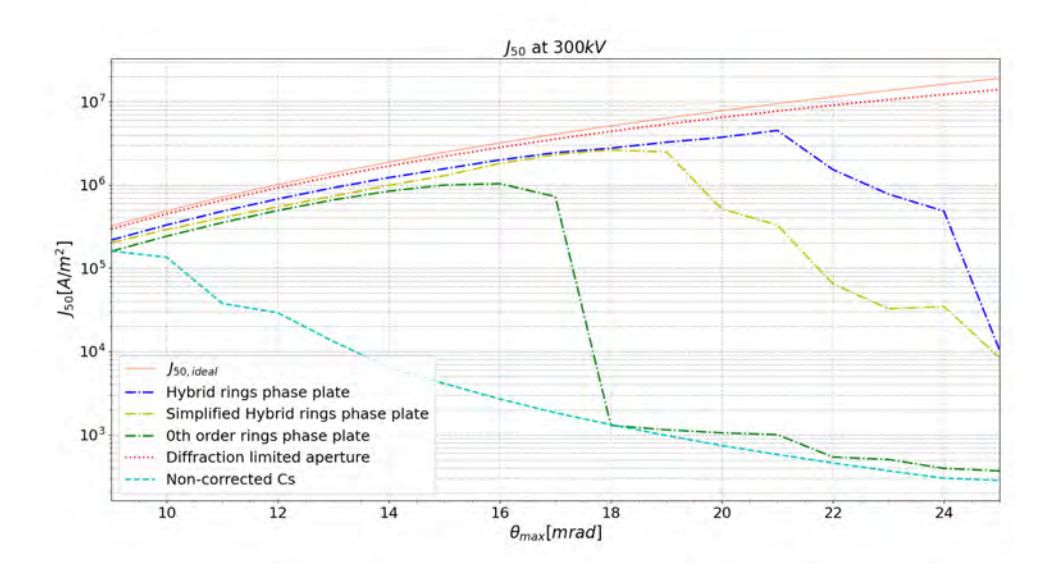


Figure 3.7: Current density J_{50} for the different phase plate designs at different θ_{max} assuming a total incoming current up to 50 pA. All proposed designs significantly improve compared with a non-corrected aperture; the red (dotted) line shows the corrected instrument's performance.

this less-than-ideal phase plate can still significantly improve d_{50} and hence increase J_{50} when compared with the non corrected situation. This may be of interest in cases where current density is more important than ultimate resolution.

In general, from section 3.2.2.1, we can see that if we aim to achieve any significant correction up to a certain d_x , we must adjust the fill factor accordingly. Suppose we aim to mitigate the effect of the tails to enclose 70% of the current. In that case, we must design a phase plate with a given symmetry to correct aberrations, with a fill factor of at least 70%, as any less would mean that we need to include a portion of the long-range tails to enclose the desired probe current. This is relevant because often, when contrast is the primary concern, we seek a signal-to-background (SBR) ratio that enables us to visualize the sample.

It is important to note that the fill factor has a double negative effect on the probe current. On the one hand, it lowers the current in the beam due to partial blocking by a factor ζ . On top of this, the beam that gets through is split into the desired part (central spot) and a tail part, which further lowers the intensity of the desired part of the beam to ζ^2 . Often, more than enough beam current is available, and the sample may limit how much current can be used. In such cases, the initial loss due to the finite transparency of the phase plate is not a problem. The tails argument still holds then, as they will lead to a degraded image contrast while still the full probe current beam damage is still induced.

Increasing the number of segments (more interconnections) or reducing their size brings the fabrication process closer to the resolution limit of photolithography ($\approx 1 \mu m$) as indicated in fig.3.4. For this reason, one must be careful with the phase plate design since high-complexity designs will require higher-resolution methods such as EUV or

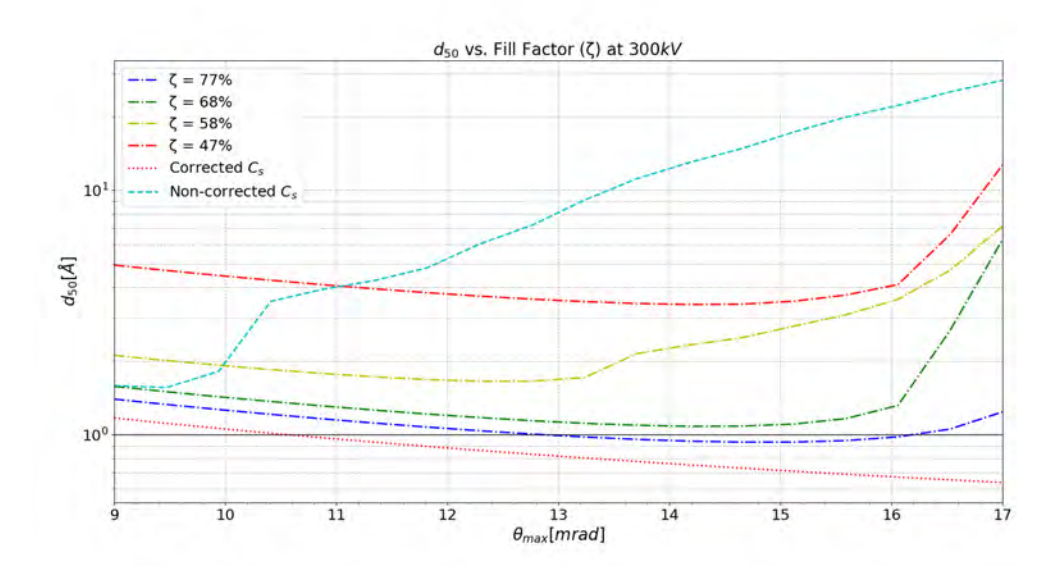


Figure 3.8: d_{50} value for different ζ using a zeroth-order phase plate. We kept the same design as in fig. 3.5 b. for the segments, only increasing the width of the lines going outwards in the radial direction and thus keeping the sampling on θ the same. We can observe how the d_{50} is heavily affected by ζ , making it difficult for a zeroth-order phase plate to obtain a sub-Å probe for $\zeta < 0.70$

e-beam lithography [161]. For instance, a zeroth-order correction requires only one electrode to create an Einzel lens inside the region of the segment. In contrast, a firstorder implementation would require a plate capacitor-like arrangement to achieve the required phase ramp. Another way to increase the fill factor is to tie the different electrodes together with a fixed resistor string, saving multiple interconnection lines. The drawback of this solution is that it would take away the ability to fine-tune each segment individually. If the projected potentials do not meet expectations, correcting them is challenging unless resistor values can be adjusted, such as through laser trimming, to achieve the desired gain. Furthermore, having a significant C_s correction seems unreasonable for phase plates with less than 50% fill factor since most of the current will land on the tails of the probe, as shown above. However, we demonstrate here that the number of segments needed to achieve sub-1Å correction can be kept relatively low, thus reducing the design complexity significantly over the design proposed in a previous study [144], (fig.5). The predicted resolution should be taken with some reservation as effects like source size broadening, vibrations, chromatic aberration, higher-order aberrations, and thermal/electronic noise were not considered for the theoretical study and will further lower the actual attainable resolution in practice.

An advantage of the proposed designs is that the performance of an electrostatic phase plate is relatively insensitive to the quality of the voltage sources driving the segments [144]. We test this claim in the zeroth-order design in fig. 3.9 by adding different normally distributed phase noise to each of the phase segments and calculating the resulting d_{50} and the difference between a case where no noise is present. We note that the increase in probe size to such noise remains under 0.1Å for most aperture angles.

Assuming an electronic system is designed to provide a maximum of 200π phase shift, such precision and noise requirements would easily be met even, i.e., with a humble 12-bit digital-to-analog converter.

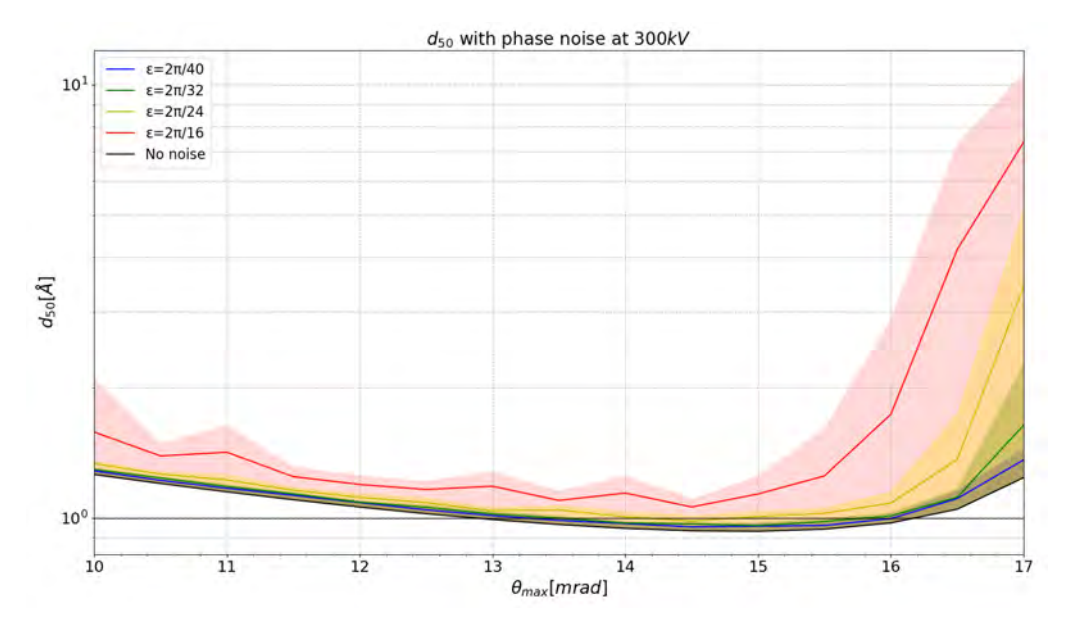


Figure 3.9: Average probe size d_{50} including different levels of phase noise ϵ for the zeroth-order ring phase plate. The shaded area represents the 2σ variation for 10 random realizations of the phase noise, and the black line shows the performance of the phase plate without any phase noise (lower limit). The plot shows that sub-Å performance is possible for all but the highest noise level simulated here.

3.5 Conclusion

We have numerically demonstrated how a programmable electrostatic phase plate can correct third-order spherical aberration in the TEM with phase plates of modest complexity consisting of 19 segments (zeroth-order) and as few as 8 segments for a hybrid design. All the proposed designs are capable of flattening the electron wavefront up to relatively high opening angles, providing sub-1Å probe sizes.

We discussed the benefit of moving from zeroth-order to first-order phase shifters to contain the phase error within some error margin. On top of this, we showed how the segment width for a first-order element does not necessarily need to have unreasonably small dimensions to correct C_s with acceptable performance. In terms of shape, we can expect that a circularly symmetric design compensates for the phase shift caused by C_s since it mimics its symmetry, thus correcting the aberrations more efficiently within each segment. In practice, some breaking of this symmetry would otherwise also be helpful to compensate for non-cylindrical aberrations. However, this would further increase the number of phase-shifting elements, and the complexity of getting interconnects to each.

We found that, to achieve C_s correction to any significant extent, the phase plate has to have a fill factor $\zeta \geq 0.75$ to achieve $d_{50} \leq 1 \text{Å}$. Moreover, we demonstrated a significant increase in current density, which is crucial for applications such as STEM-EELS, even for cases where the fill factor is low. When the current density at the center of the probe is important, we argued that it scales as ζ^2 , since the total current and the amount of current in the probe tails scale with the fill factor.

We investigated the robustness of the correction versus noise on the electrostatic potentials of the phase-shifting elements, showing that, for a zeroth-order phase plate, we get excellent results for $\epsilon \leq 2\pi/24$, which is well within reach of even simple digital-analog converter circuits. For instance, we can refer to traditional optics, where the Strehl ratio [162–164] serves as a standard measure of the degradation of the PSF of an optical system (i.e., the probe). A variation of $\pi/10$ radians indicates excellent optical performance.

This study demonstrates that an adaptive optical device can enhance the performance of a non-corrected instrument without requiring significant changes to the column's optical configuration. However, further development and testing are needed to assess its reliability and lifespan before it can be considered a viable solution. Additionally, incorporating adaptive optical elements in an electron microscope increases flexibility and performance, allowing for a broader range of experimental setups and ultimately expanding the microscope's capabilities.

Besides (adaptive) aberration correction, one of the potential applications for electrostatic phase plates is to shape the beam to either enlarge the depth of focus or increase the z-resolution. This first idea has been demonstrated before using a spatial light modulator that can generate Bessel-like beams invariant with propagation length [165, 166]. However, we can also attempt to correct higher-order aberrations with a phase plate to increase the opening angle, potentially enhancing the z-resolution (which scales as the inverse of the squared opening angle).

Another possible application is to use the phase plate for phase retrieval experiments, which will be discussed thoroughly in chapter 5. This idea has already been studied in optics [167–169], and it has been hinted that the possibilities of fast and reliable wavefront tuning with the electrostatic phase plate can allow us to do the same in the electron microscope [170].

Increasing selectivity in inelastic scattering experiments by differential experiments that rapidly change the probe between two or more configurations is another class of applications that could shed light on the magnetic, chiral, and optical response of materials at the nanoscale [107, 147]. Furthermore, having such adaptive apertures allows for automatic correction and optimization, self-tuning the phase of each of the segments to match the user's needs.

The performance of the proposed designs in terms of C_s correction capabilities is inferior to that of a modern multipole corrector. Still, the proposed setup would offer several significant advantages, such as small size (1 mm scale), low power consumption (1 W scale), high speed (up to 100 kHz, extendable to much higher), no hysteresis, vastly reduced precision constraints on drive electronics (12 bit suffices), negligible drift, and potentially low production cost.

3.5. CONCLUSION

These observations will guide further practical implementations with the experimental realization of phase plate-based aberration correction on the nearby horizon.

CHAPTER 3. DESIGNING AN ELECTROSTATIC PHASE PLATE FOR ABERRATION CORRECTION

Chapter

Quantum Wavefront Shaping with a 48-element Programmable Phase Plate for Electrons

This chapter is based on:

Yu, C. P., **Vega Ibañez, F.**, Béché, A., & Verbeeck, J. (2023). Quantum wavefront shaping with a 48-element programmable phase plate for electrons. SciPost Physics, 15(6), 223.

Contents

Contents		
4.1	Introduction	52
4.2	Experimental considerations	53
	4.2.1 Description of the Electrostatic Phase Plate	53
	4.2.2 Characterization	54
4.3	Application Examples	56
	4.3.1 Designer Electron Waveforms	56
	4.3.2 Object Sampling with Different Wavefunctions	58
	4.3.3 Adaptive Optics	61
	4.3.4 Phase programmed Ptychography	62
4.4	Conclusion	64
4.A	Defocused Images of the Phase Plate	65
4.B	Pixel Index	66

Summary

In this chapter, we present a 48-element programmable phase plate designed for coherent electron waves. This device results from a combination of photolithography and focused ion beam techniques. Building on the concept introduced by [144], this section leads to a more generalized solution for electron wavefront shaping. The phase plate chip is mounted on an aperture rod in the C2 plane of a transmission electron microscope that operates within the 80-300 kV range. We characterize the phase plate's behavior using the Gerchberg-Saxton algorithm, which demonstrates a phase sensitivity of 0.075 rad/mV at 200 kV and a phase resolution of approximately $3\times10^{-3}~\pi$. Additionally, we provide a brief overview of potential use cases supported by both simulated and experimental results.

4.1 Introduction

So far, we have explored electron wavefront shaping, emphasizing its potential applications and the benefits it may provide. However, while we have outlined the design parameters and linked them to current manufacturing technology capabilities, we have not yet discussed the performance and capabilities of a state-of-the-art electron wavefront modulator.

Besides canceling geometric aberrations, the ability to arbitrarily shape the electron wavefront is gradually gaining attention with the hope of improving contrast or selectivity in electron microscopy setups. There has been a renewed surge of such phase modulators and their applications in the past few years. In soft material imaging, different phase plates such as Zernike [171, 172], Boersch [128, 133], Zach [139, 142], or Volta [173-175] have been implemented in the TEM to imprint a constant phase shift to a (central) part of the electron wave, to increase the contrast when imaging weak phase objects. Some other designs with relatively higher complexity may modify both the amplitude or phase configuration of the electron wave to create an electron probe of specific shape [176], to increase contrast [177, 178], or to extract specific information from the electron-sample interaction [179, 180], to name a few. Some of these complex modulators even exhibit control over the parameters or magnitude of the modulation. The electrostatic phase plate reported by Verbeeck et al. [144] has demonstrated changes in interference between 4 partial waves by altering their mutual phase relation. In a different approach to electrostatic phase plates, reported by Tavabi et al. [181], a tuneable azimuthal phase was demonstrated by setting up specific electric field boundary conditions, which can be interpreted as adding orbital angular momentum to the electron beam. Moreover, Barwick and Batelaan [182] showed that a pulsed laser beam could induce a phase shift in the electron beam and that the contrast of the formed image can be optimized by tuning the intensity of these laser pulses. Different realizations of using the ponderomotive force to change the phase of an electron beam appeared as well [150, 183–185].

In this chapter, we report on an adaptive electrostatic phase plate based on the proof of principle demonstration by Verbeeck et al. [144], but with significantly increased complexity, performance, and practical usefulness. The phase plate consists of 48 openings,

or pixels, transparent to an incoming coherent electron wave. The vertical walls of the pixels are made into electrodes so that an electric potential can be established inside, locally changing the wavelength of that part of the transmitted wave. Since separate voltage sources control each of the 48 pixels, the phase of the entire transmitted coherent electron wave can be programmed at will. This design and the electrostatic nature grant the phase plate several advantages, such as short response time, the ability to realize complex and arbitrary phase configurations, low power dissipation, compactness, and high stability and repeatability.

The experimental part of the chapter provides a concise summary of the reported phase plate. First, the design of the phase plate is described, as well as the components and mechanism for creating a phase shift on an electron wavelet. The manufacturing design choices are briefly discussed in relation to the scope of the challenges faced. The device's optical performance is then evaluated regarding its phase sensitivity and response time.

We discuss some potential applications in electron microscopy. Using the unique properties of a fast, hysteresis-free, programmable phase plate, we demonstrate how novel imaging setups can expand or improve imaging modalities in TEM. We provide simulated examples and early experimental attempts towards electron wave modulation, complex sampling schemes, adaptive optics, and phase-coded ptychography to hint at what phase plates could bring to the electron microscopy community.

4.2 Experimental considerations

4.2.1 Description of the Electrostatic Phase Plate

The basic working principle of the phase plate is sketched in fig. 4.1-a. A coherent incoming electron wave is made to interact with an insulating membrane that has several holes. The top and bottom surfaces of the membrane are covered with a ground shield, while the inside of the holes is coated with a conductive layer that can be put to a controlled electrostatic potential (V_1 and V_2 in the simplified sketch). The potential surrounding the holes creates a landscape of potential for fast electrons, accelerating them upon entry and decelerating them upon exit. Therefore, the change in wavelength will be localized. This will cause a phase change between the partial waves leaving these holes where one could imagine them as coherent Huygens sources that will constitute a now phase-programmed wave upon propagation in free space. As discussed in eq. (2.9), the phase shift ϕ obtained is given by the electrostatic Aharonov-Bohm shift:

$$\Delta \phi_{AB} = \frac{\pi e}{\lambda E_0} \int_{\Gamma} \phi(\mathbf{r}) dl \tag{4.1}$$

For an electron wave with wavelength λ and energy E_0 , crossing a region of space with an electrostatic potential $\phi(\mathbf{r})$ along a trajectory Γ . In the case of a weak perturbation, the electron's trajectory is not altered by this field, and the phase shift becomes directly related to the projected electrostatic potential. The goal of a pixelated phase plate is to create a potential profile that, in projection, leads to a constant phase shift within a phase pixel, proportional to the voltage applied to each pixel element. This occurs if

the projected potential changes as little as possible over the region covered by each hole, which can be obtained by choosing a high aspect ratio (height/diameter> 1).

From a practical perspective, the AdaptEM WaveCrafter phase plate [186] comprises three main elements shown in fig. 4.1b-e: a dedicated condenser aperture holder containing the phase plate chip, a 48-channel programmable voltage source, and a remote computer for control and user interface, respectively. The phase plate used in this work comprises 48 independent, active elements, or pixels, arranged in 4 concentric rings and 12 petals (see fig. 4.1b). Each element consists of a layered structure similar to the one described by Matsumoto and Tonomura for a single phase-shifting element [127]. An aspect ratio (depth of the hole to the diameter of the hole) of approximately two was chosen to minimize lensing and crosstalk effects between pixels, as the fringe fields around each segment could affect the phase shift of that phase pixel. Additionally, a total active area diameter of 50 μm ensures that a modern electron microscope can coherently illuminate the entire device.

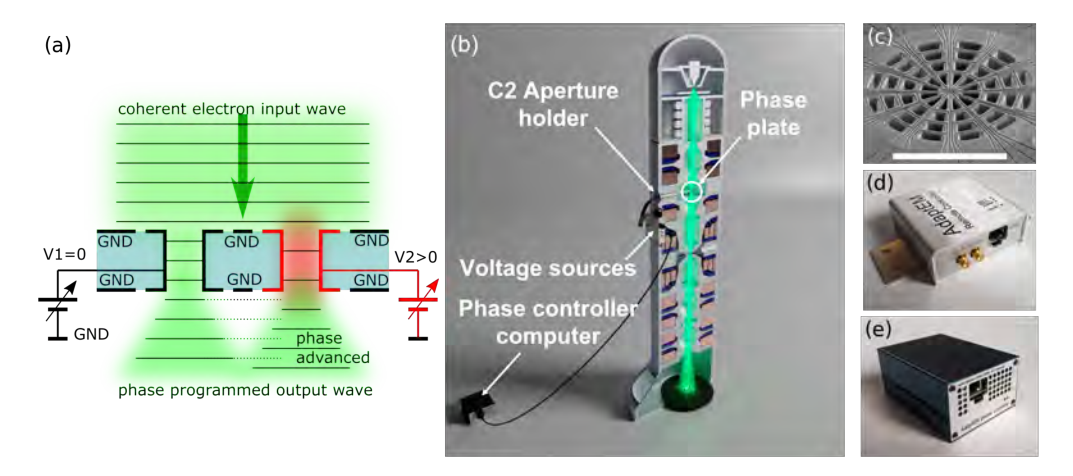


Figure 4.1: Sketch of the working principle of the phase plate (a). Only 2 pixels are drawn. 3D render of the setup (b) and the main components, including the phase plate (c), the voltage sources (d), and the phase controller computer (e). A reference bar of $30 \mu m$ is presented in (c).

One considerable advantage of this phase plate design lies in the relatively low voltage (in the mV range) required to induce a phase shift of 2π . This avoids high electric field breakdown issues in the nanoscale features of the chip and has the benefit that readily available voltage sources, which are simultaneously precise, stable, low power, fast and reliable, can be used.

4.2.2 Characterization

To experimentally examine the projected potential profile, a phase reconstruction based on the Gerchberg-Saxton (GS) algorithm [187,188] was performed on a set of TEM images of the phase plate, where each pixel is excited with increasing electrostatic potential (48 pixels, 11 voltage levels, 528 images in total). For the characterization, the phase plate is inserted in the sample plane of an FEI Tecnai Osiris S/TEM operating at 200 kV and

4.2. EXPERIMENTAL CONSIDERATIONS

illuminated with a parallel electron beam. The images are taken from the back focal plane of the objective lens (diffraction mode), while the objective lens is largely defocused so that the detector can capture the near-field diffraction pattern of the phase plate. This experiment is aimed to characterize the projected potential on the phase plate, while varying the phase inside each pixel in a range between 0 and 2π . A rough estimation of the voltage corresponding to a 2π phase shift was first found by assigning a gradually increasing voltage to half of the pixels randomly and repeatedly. Theoretically, a 2π phase shift should not result in any difference in the diffraction pattern formed by the phase plate. Thus a visual inspection of the voltage at which the pattern shows the least variation over time is a reasonable estimation of the value at which the pixels yield a 2π phase shift. Once this voltage $V_{2\pi}$ was found, a series of images with different potentials equally spread between 0 and $V_{2\pi}$ was taken for each pixel.

The defocused condition was specifically chosen so that outgoing waves from the electrodes interfered strongly with each other, and the phase difference between separate neighboring wavelets is significantly encoded in the recorded intensity images (see section 4.4). This choice of detection plane was preferred over recording at an in-focus condition that interferes all of the wavelets together (far-field) for several reasons. First of all, at the right focus, the transmitted electrons are concentrated in a very small region (less than 1 % of the size of the recorded defocused images), and creating a high enough camera length to sufficiently sample such patterns on a pixelated camera for phase retrieval is not trivial. On top of that, the inversion invariant nature of the wave intensity in the reciprocal space would also challenge obtaining a unique reconstruction and greatly hinder the retrieval algorithm's convergence [189].

The result of the reconstruction is summarized in fig. 4.2. The phase response of all pixels, as they were individually excited, is fitted using a linear function, representing the phase sensitivity of that pixel to the applied voltage. A phase sensitivity matrix can be constructed showing the phase sensitivity of pixel i upon exciting pixel j. The phase sensitivity matrix in fig. 4.2 shows a strong response on the diagonal, meaning that a given excited pixel is the only one showing a significant linear phase shift against a voltage applied to itself. An average phase sensitivity of 0.075 rad/mV is found, which translates to a theoretical phase resolution of approximately $3\cdot 10^{-3}~\pi$ according to the smallest step size provided by an ideal 16-bit Digital to Analog Converter (DAC) (maximum 2.5 V, smallest step 2.5×2^{-16} V). The error matrix, also shown in fig. 4.2, indicates response deviation from the expected linear behavior, mainly resulting from imperfections in the phase retrieval process, such as the finite pixel size and non-ideal detector response. These can cause a difference between the recorded intensity and the actual waveform. The error is calculated by the root mean square error of the fitted result, which is found, at maximum, to be 3% of 2π (0.19 rad), while on average less than 0.5% of 2π (0.027 rad).

Besides the expected response of the phase plate, it is equally important to characterize any non-ideal behavior. The inhomogeneity describes the phase deviation within the pixel area from the ideal constant, homogeneous expectation. We evaluate the standard deviation of the reconstructed phase within each activated pixel and find it to be < 1.7% of 2π . The cross-talk refers to the phase response within a pixel region caused by the voltage applied to another pixel. We estimate this as the maximum linear response of a non-excited pixel as a function of any other excited pixel. The off-diagonal lines found exactly 12 pixels away from the main diagonal in both matrices in fig. 4.2 indicate

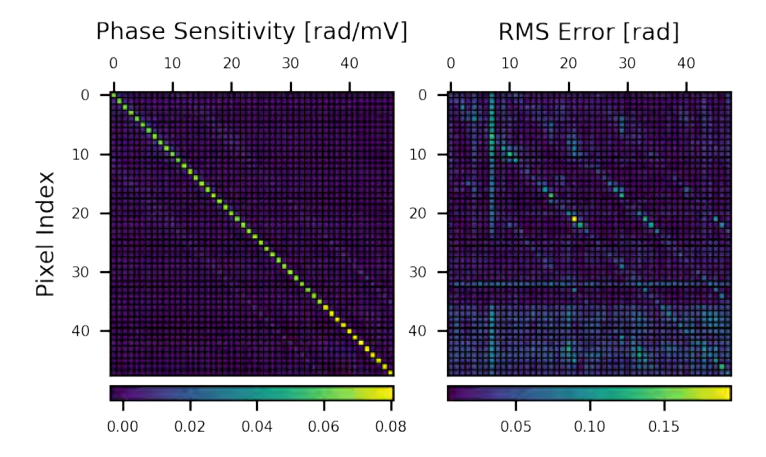


Figure 4.2: Phase sensitivity matrix and the corresponding root mean squared error of the linear fitting.

that the strongest cross-talk is, unsurprisingly, found between neighboring pixels due to how the pixels are ordered in the matrix (see section 4.4). The cross-talk is measured to be < 0.012 rad/mV, which amounts to 15% of the response of the excited pixel. In summary, the inhomogeneity only creates phase error much less than $\frac{2\pi}{10}$, which is generally accepted as very good in light optics [162,164], while the cross-talk is clearly the biggest contributor to a non-ideal response. This behavior could be significantly improved in the next design iteration, where an additional top-ground layer could shield the effects from neighboring pixels and the conductive tracks leading to those pixels.

Characterizing the temporal response of the phase plate is also important for applications that rely on rapid switching between different electron probe shapes or phase configurations. Since the phase shift results from the projected potential in the electrodes, the response of the phase plate can be characterized by the time required to build up the potential. With the criterion of phase error $<\frac{2\pi}{10}$, the response time is measured to be less than 1.3 μs for reaching from 10 % to 90 % of $V_{2\pi}$ and is entirely dominated by the settling time of the DAC.

4.3 Application Examples

4.3.1 Designer Electron Waveforms

To demonstrate the capability and visualize the effects of a freely programmable phase plate, we recorded the far-field diffraction patterns of various phase-modulated electron waves in a TEM (fig. 4.3). These patterns form rather complex configurations compared to ones formed by commonly-used round apertures, even when all phase plate elements are at ground potential. This is due to the amplitude modulation created by the set of holes, which produces highly delocalized tails. In the previous chapter, we showed how the proportion of the electrons in these tails is directly related to the fill factor (% of

4.3. APPLICATION EXAMPLES

the electron wave not blocked by the material of the phase plate) of the probe forming aperture chapter 3. Although improvement has been made on the fill factor (current design approximates 30%, while the proof of concept 2x2 version from 2018 [144] had only 17%), a large proportion of the electrons can still be expected in the tails.

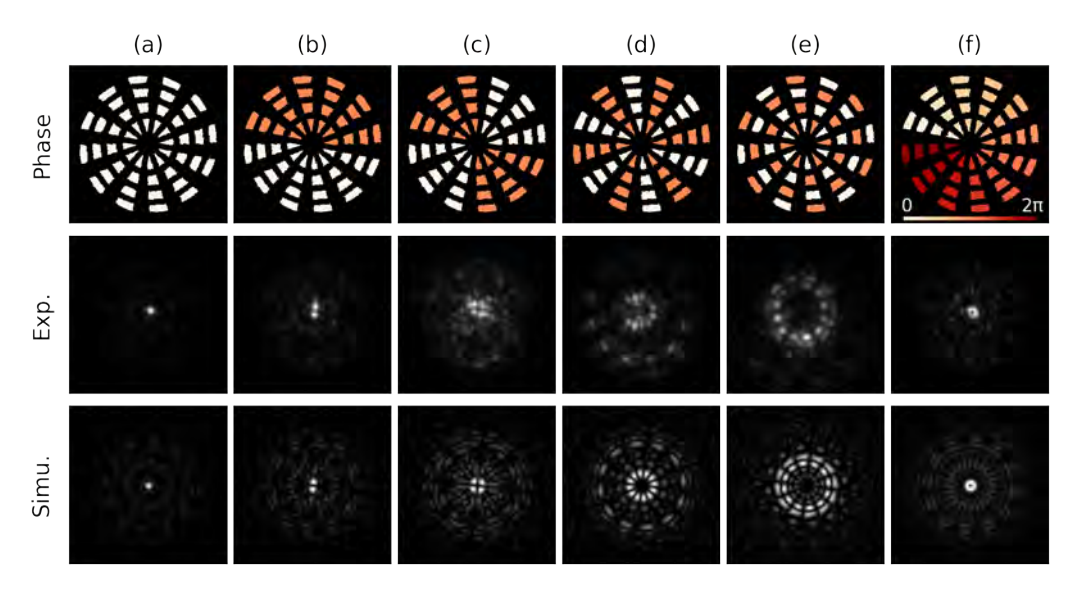


Figure 4.3: Realization of various electron quantum states. The three rows of figures, from top to bottom, are the phase configurations set on the phase plate, the simulated probe shapes, and the resulting experimental probe images, respectively. Note the excellent agreement between expected and obtained results showing successful arbitrary wavefront shaping.

A match between the general profiles of the experimental and simulated intensities profiles is found. From fig. 4.3, columns (b-e) show a phase shift of π applied to half of the total pixels with different patterns; therefore, the original single intense spot in the diffraction pattern is split into multiple parts due to destructive interference. Double-spots (b), quadruple-spots (c), and even a 12-spot (d) consisting of six $0-\pi$ pairs are shown. By taking into account the radial distribution of the rings, a checkerboard-like pattern (e) can be created. These patterns cover a few instances of the 48-dimensional Hadamard basis set [190], which defines an orthogonal basis consisting entirely of pixels with either 0 or π phase. Lastly, (f) shows the result of a vortex setup with an orbital angular moment equal to 1 [157,191]. This is done by creating a phase ramp from 0 to 2π in the azimuthal direction. The vortex can be verified by the signature singularity point at the center of the resulting probe approximating one member of the Laguerre-Gaussian orthogonal basis set [192]. Despite not having a reference for the dimension of such probes due to the optical calibration of the camera, it can be expected from the convergence angle (i.e., 1mrad) that they are a few nanometers in size.

The phase plate can also create a phase profile imitating geometric optical elements and aberrations. Typically they can be modeled by a phase shift that follows a Zernike polynomial [130] in the angle with respect to the optical axis [15]. How faithfully the phase plate can recreate such polynomials at different angles has been discussed theoretically in detail in chapter 3 and relates to parameters such as the order of aberration, the fill

factor, number of pixels, and pixel shape. Here, a defocus effect (second-order in angle) is introduced by either the conventional electromagnetic objective lens of the microscope or by the phase plate to demonstrate this concept. The resulting probe shapes are shown in fig. 4.4, respectively. The two rows show good resemblance with each other up to 200 nm defocus. Further defocusing causes a steep phase ramp within the area of the individual pixels, which can not be faithfully reproduced anymore by the phase plate. For this reason, the phase plate can not replace an actual (round) lens of any significant strength.

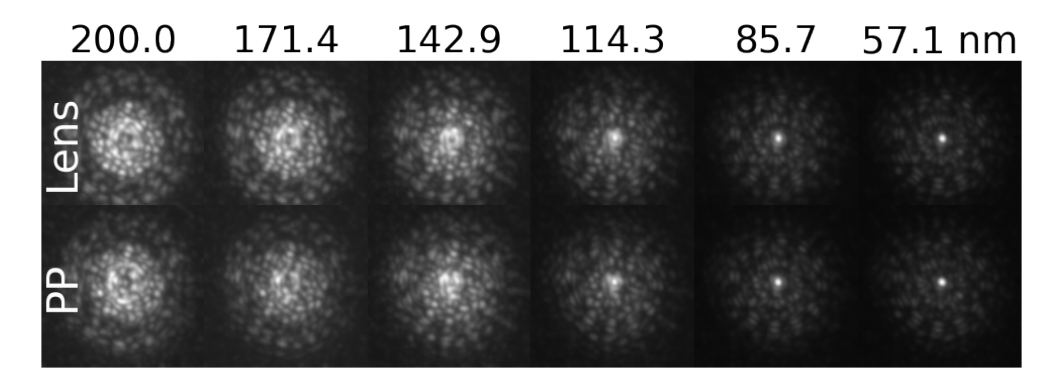


Figure 4.4: Defocused probes formed by defocusing the microscope lenses (top row) and the phase plate (bottom row) at 300 kV acceleration voltage and an opening angle of 1 mrad. Note the close similarity of both, showing that the phase plate can mimic the action of a round lens to up to 200 nm defocus.

4.3.2 Object Sampling with Different Wavefunctions

As introduced before, electron microscopy is a technique for analyzing an unknown material by employing an electron wave. When the incident electron wave interacts with the object being examined, information from that object is imprinted onto the wave. This interaction redistributes the intensity and phase of the incident electron wave compared to the wave that has passed through the object. When the measurement result of the interaction between the object and a beam with a given electron waveform provides insufficient information about the sample, a selection of different waves can be used to interrogate the object. For example, in-line holography [193–195] is done by recording the intensity of the beam post-interaction, while varying its phase in reciprocal space, i.e., through a focal series done with the objective lens. STEM essentially describes a process to accumulate information about the material by a dense sampling while spatially scanning a localized electron beam. In both cases, multiple measurements while changing the incoming electron wave enriches the acquired information and eliminates confusion that can sometimes not be resolved with a measurement process that only uses a single static waveform.

Such multi-waveform sampling schemes rely entirely on the ability to alter the wavefunction of the beam electron states. Even though some form of modulation of the wavefunction is present in any electron microscope (e.g., defocus, beam tilt, beam shift, or aberration correctors), they often rely on electromagnetic elements, which can suffer

4.3. APPLICATION EXAMPLES

from slow settling times and hysteresis effects. For example, in the acquisition of images in a focal series, an update rate in the order of seconds to minutes is typically applied to induce small focal changes in the objective lens [196, 197].

The phase plate presented here can update to an entirely new pattern in a few μ s without hysteresis so that complex sampling schemes can be realized efficiently. For instance, the phase plate can cycle over a few different wavefront settings for each probe position in a STEM recording. Compared to through-focal TEM acquisition, where the focus is changed between recording image frames, we could now update multiple focus levels for each probe position in a STEM scan, providing, i.e., increased depth of field [198]. This dramatically reduces the difficulty of realigning each image, especially in cases of severe sample drift, and also avoids inconsistencies caused by contamination building up on the sample over time.

Changing the defocus is just one of the possible manners of forming a selection of wavefunctions to sample an object of interest. As it consists in a non-orthogonal influence, it could be argued that this is not even an optimal choice of basis. The adaptability and rapid response of the phase plate can be extended to a wide variety of orthogonal basis sets that can be specifically chosen to efficiently encode selected knowledge about the sampled object into the probing electron waves.

A similar concept is widely used in light microscopy and is an essential cornerstone for techniques such as stimulated emission depletion (STED) microscopy [199–201]. Two or more waveforms sequentially illuminate the sample, and the sharp feature created by the difference between the illuminating waves can be exploited to increase the resolution of the final image. The main difference is that the proposed method is simply an incoherent subtraction of two signals, despite the complexity of the subtraction or deconvolution employed to interpret the final signal. In contrast, in, e.g., STED, both signals are inherently combined through the optical process responsible for shaping the PSF. This seemingly small implication could play a vital role when discussing dose efficiency, as the noise increases with each recording, which is not the case for optical methods. A similar approach to what we discuss here is given by switching laser mode microscopy (SLAM) [202, 203], where the subtraction between the two PSF occurs once the signal is recorded.

Indeed, changing between a probe state with and without orbital angular momentum will slightly improve image resolution due to differential imaging with both probes (super-resolution). But more importantly, this method also cancels the long probe tails arising from the amplitude modulation of the pixel shapes, as these tails are nearly identical for both probe wavefunctions. This is a far more critical effect as it dramatically increases the practical resolution that can be obtained even when the fill factor of the phase plate is not ideal and shows a way to significantly outperform the results presented earlier for the single waveform aberration correction prospects of programmable phase plates for electrons chapter 3. The result of this differential scheme is demonstrated with (HAADF)-STEM simulation (fig. 4.5). Electron probes are generated from the far-field diffraction of three illuminating wavefunctions created by a phase plate. These wavefunctions comprise a zero phase, a vortex phase, and a conventional round aperture. This study uses these probes to scan a single-layer hexagonal boron nitride sample with an electron beam energy of 200 keV. The experiment operates with a spherical aberration coefficient C_3 of 1.2 mm and at Scherzer defocus, similar to the settings of a typical

uncorrected TEM. The convergence angles of the electron probes are set to 9.5 and 11 mrad for the round aperture and the phase plate, respectively. We select a larger opening semi-angle for the phase plate since its capability to correct aberrations yields an optimal imaging condition at 11 mrad. The subtraction of the vortex image from the plain phase plate is then presented as the difference image. Although the dose and stability requirements for the experiment increase, with this method, we can potentially increase the resolution of a non-corrected microscope by combining this technique with, e.g., the findings from chapter 3, broadening the possibilities for the implementation of this technology, as we could circumvent the use (and cost) of an aberration corrector in some cases.

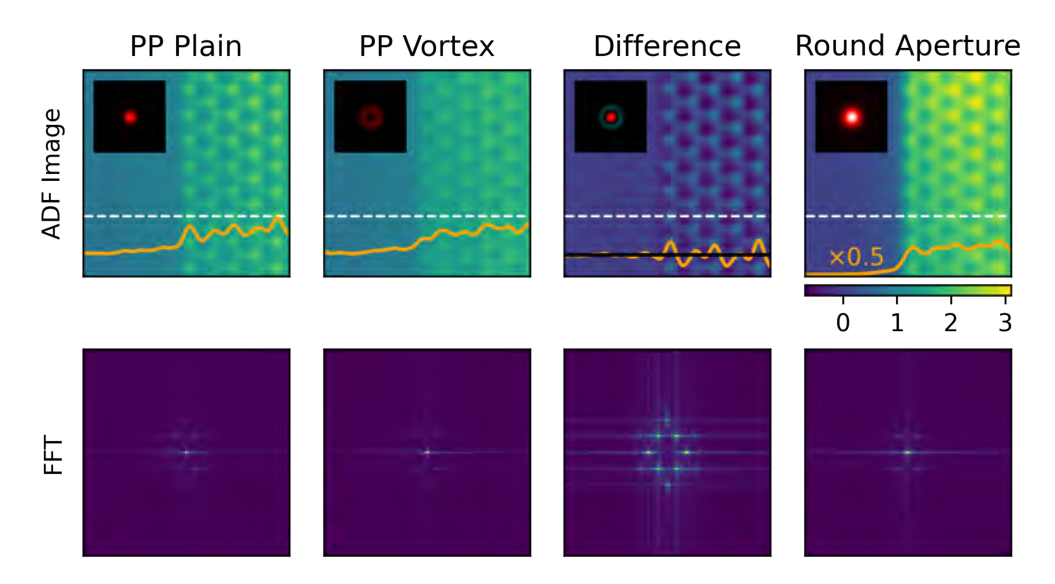


Figure 4.5: Simulated ADF images of various probe shapes (see the insets) and their Fourier transforms. The line profiles (orange lines) are taken at the position of the white dashed line in each image. Note that the intensity profile in the round aperture image is halved for better presentation and that the black line in the difference image indicates zero, while in other images, zero is set at the bottom of the figures.

The simulated images are juxtaposed to illustrate the effect of the tails, and an intensity profile (orange line) is drawn across each image (at the position of the white dashed lines). Both images from the phase plate have non-zero intensity in the vacuum area (the left half of the simulation box) due to the tails' interaction with the crystal. The profile from the image formed with the round aperture shows much faster decay as the intensity distribution of an aberrated Airy probe is more concentrated. The difference image demonstrates good cancellation of this background, and the intensity profile quickly converges to zero, with minor fluctuations due to slight differences between the tail configuration of the two probes. The resolution is significantly improved compared to the non-corrected round aperture, though this comes at the cost of some signal loss due to the fill factor and a reduction in low-frequency sample information. This showcases the potential for aberration correction using a device that is much smaller (less than 5 mm), lighter, faster (operating in microseconds), and more energy-efficient (less than 5 W, owing to the resistance of the tracks). Moreover, this device requires much less stringent control over the precision of the voltage and current sources than

current multipole correctors. This is because the phase profile is local and does not rely on meticulous adjustments of the boundary conditions across the entire numerical aperture.

4.3.3 Adaptive Optics

Using the fast and hysteresis-free phase programming offered by the electrostatic phase plate opens the attractive possibility of adaptive optics. As a proof of concept, such a setup is realized experimentally (fig. 4.6). An algorithm repeatedly reshapes the electron probe with the phase plate in order to reach a higher variance in the HAADF image, which is taken as a figure of merit that links with *image sharpness* [204].

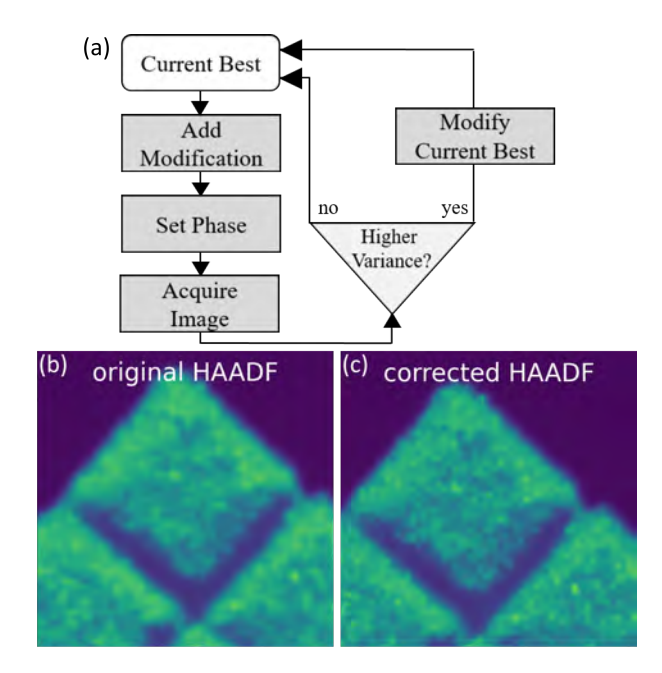


Figure 4.6: Schematic of the adaptive probe correction with phase plate. The flowchart displayed in (a) demonstrates the fundamental steps of the algorithm being employed. The HAADF images before (b) and after (c) the correction are shown below.

The algorithm sequentially adds phase modifications from a list of discretized low-order Zernike polynomials to the latest best-performing phase configuration. Zernike polynomials are chosen since they exhibit close similarity to common aberrations in the electron microscope and form a complete, orthogonal basis. An HAADF image is consequently recorded with every new probe. If the variance is higher in the new image, the current best is replaced with this new variation. Once all the configurations are tested, their magnitudes in terms of phase value are reduced by half for a further refinement step, in a binary search-like manner within the chosen set of Zernike polynomial coefficients. The process is demonstrated by inserting the phase plate in the C2 aperture of a probe- and image-corrected ¹ FEI Titan operating at 300 kV in microprobe mode with a convergence

 $^{{}^{1}\}text{In corrected instruments, aberration corrector modules are usually located either before the sample (probedies)}\\$

CHAPTER 4. QUANTUM WAVEFRONT SHAPING WITH A 48-ELEMENT PROGRAMMABLE PHASE PLATE FOR ELECTRONS

angle of 1 mrad (to minimize the effect of aberrations and partial coherence effects). The HAADF image is taken from a commonly used calibration sample in STEM (gold cross-grating) with a deliberately introduced initial defocus of approximately 1 μ m. The result of the correction is shown in fig. 4.6(c). The process converges after 32 iterations with a sharper resulting image, even though 1 μ m defocus cannot be entirely compensated by the phase plate due to the steep phase profile. The result shows the feasibility of counteracting the lens defocus automatically. The process takes approximately 1 minute, but this time is currently dominated by sub-optimal software communication between scan engine control, image readout, and phase plate control, and can be dramatically improved in the future. As an estimate, with the assumption that an update can be made by evaluating a minimum area of 100x100 scan points at 1 μ s dwell time (a reasonable dwell time to produce HAADF images with an acceptable noise level), the update rate for the correction scheme would be 1 kHz. This frequency is easily within reach of the phase plate, which currently offers a maximum update rate of 100 kHz, limited by the electronics. This would result in an adaptively optimized image within 10 ms, a small fraction of the time to take a full 1024x1024 frame. Of course, this time depends on the beam current, as enough image quality is required to make good decisions on the next step. Further work is needed to evaluate the best goal function and most optimum control loop, but the proof of concept demonstrates the scheme's feasibility.

This process could bring significant benefits for the automation of microscopy experiments. Automatic data acquisition and feature identification are widely used for life science [205–207] research and quality control in the semiconductor industry [208, 209]. With them, the analysis of large amounts of samples can be done without operator intervention, and the demonstrated probe correction scheme can be utilized to maintain the optical system's image quality over a much longer operation time.

This iterative optimization process can also be extended to any technique in electron microscopy where a specific quantifiable property is related to the shape or phase of the electron probe. For example, in electron energy loss spectroscopy, the intensity of a specific plasmon peak can be tracked while reshaping the electron probe until the optimal probe shape selectively highlights the corresponding plasmon mode [107,147].

4.3.4 Phase programmed Ptychography

Besides shaping a focused electron beam, the phase modulation capability of the phase plate operating under parallel-beam conditions can bring new opportunities for other microscopy applications. For example, coherent diffractive imaging (CDI) [210–212] and ptychography [213–215] can benefit from using the phase plate as a "modulator" or a "diffuser" to break symmetry in the illuminating beam and thus increase the robustness and convergence rate of the reconstruction. The benefit of a modulator has been widely reported and studied in the field of light microscopy [216] and electron microscopy [217–219]. Among the reported realizations of ptychography in electron microscopy, with or without a modulator, the reconstruction of the complex object relies on repeated sampling at different locations of the object, with the criterion that the illuminating beam partially overlaps with the sampling at a nearby position [220]. This overlap creates the so-called "information redundancy" [221, 222], which eliminates the twin-

corrected) or after the sample (image-corrected), and sometimes both are present, as illustrated in fig. 1.8.

4.3. APPLICATION EXAMPLES

image artifact [223] that originates from the central symmetry of the illuminating beam. On the other hand, such symmetry can be easily broken by a random phase configuration introduced by the phase plate instead of the displacement of the beam or the sample.

We hereby demonstrate this concept by performing phase reconstruction on simulated diffraction patterns from a target pure phase object (fig. 4.7a). The diffraction patterns are generated by different illuminating waves, formed with a round aperture, the phase plate without any phase (amplitude modulation only), and one randomly generated phase configuration. The phase reconstruction is again based on the GS algorithm, and the resolved objects are obtained after 50 iterations. The results are shown in fig. 4.7(b-d). Neither a round aperture nor a zero phase plate could generate a convincing reconstruction result, as the geometry of both apertures is centrosymmetric. However, introducing a random phase configuration increases the reconstruction quality significantly despite the sample being only illuminated at one beam position.

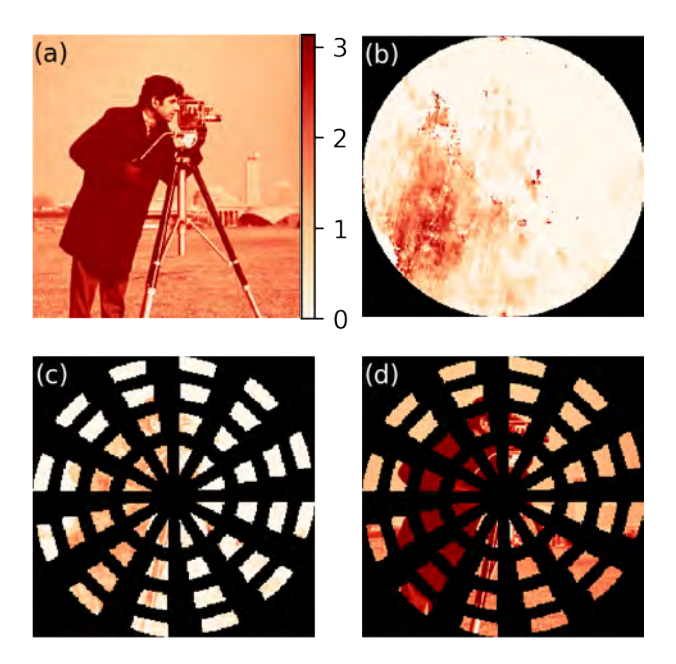


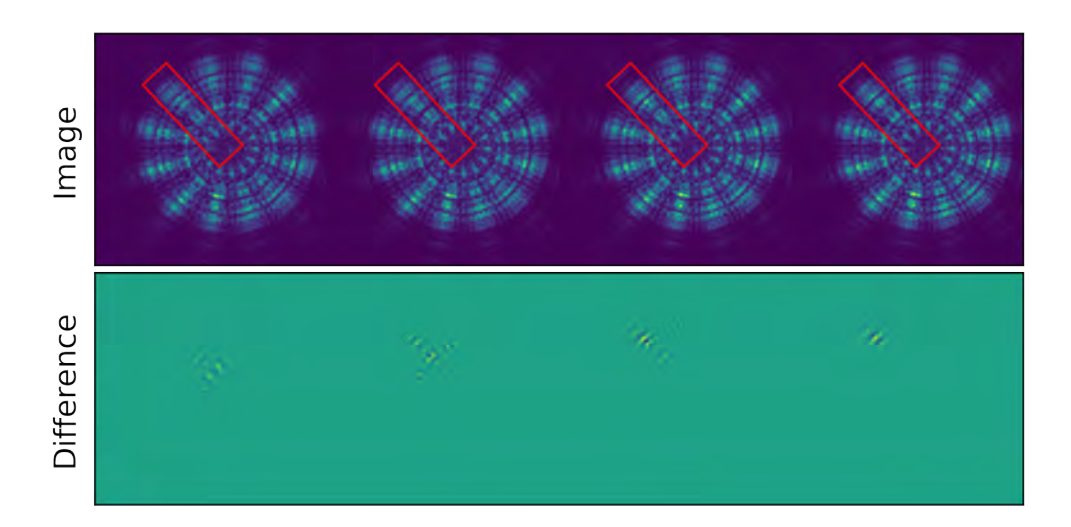
Figure 4.7: Simulated ptychographic phase reconstruction from recorded diffraction patterns with various illuminating beams. (a) The ground truth phase image of the object. (b-d) Reconstruction results from illuminating beams formed by a conventional round aperture, flat phase plate, and phase plate with random phase configuration, respectively. The dark region indicates the opaque part of the aperture. Note the significant improvement in phase reconstruction quality when the incoming beam is phase randomized. As the object is only illuminated once, reconstruction is only possible in those areas where the amplitude is not zero.

The amplitude modulation of the phase plate inevitably results in unsampled areas for the reconstructed object, which could be filled by moving the beam or the sample to illuminate the whole region of interest at least once. It should be noted here that the phase plate is placed in front of the sample, and all electrons interacting with it are recorded. This means that the limited fill factor does not reduce the dose-efficiency nor increase beam damage on the sample.

4.4 Conclusion

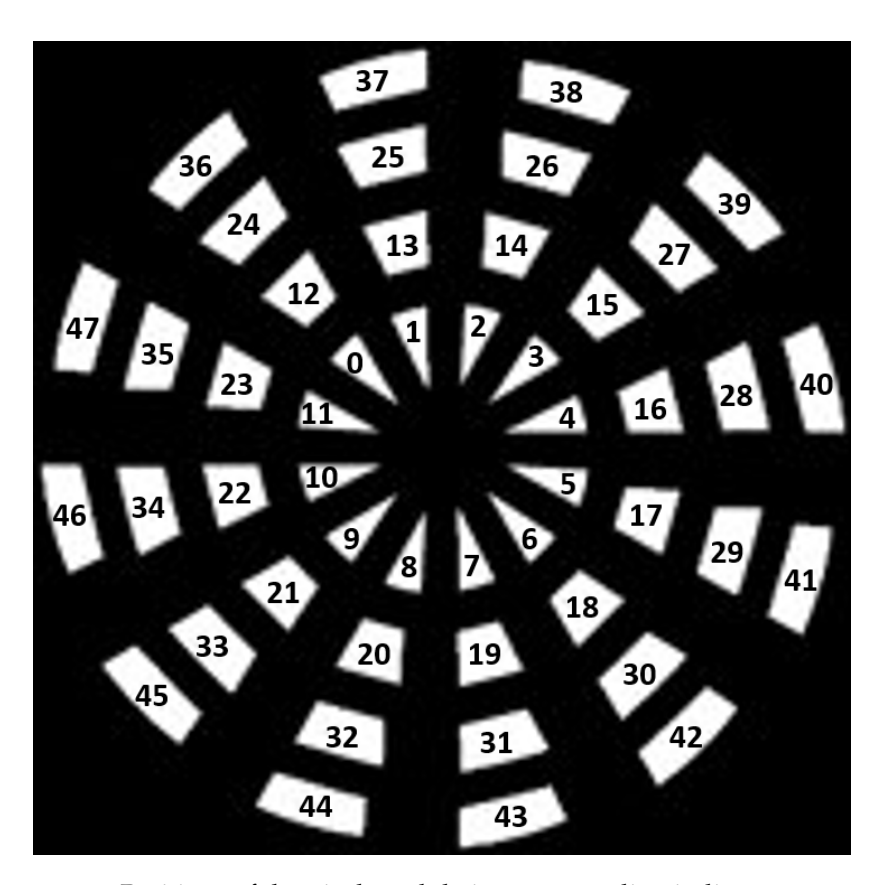
We report the successful realization of arbitrary wavefront shaping of electrons with a novel 48-pixel programmable electrostatic phase plate. The phase plate is capable of introducing a phase shift of more than 60π , as well as fine-tuning the phase value with step size as small as $3\cdot 10^{-3}$ π for 300 keV coherent electron beams. Cross-talk between pixels was shown to be < 15% and can be improved further with better shielding electrode geometries. This brings modern adaptive light optics concepts into the domain of electron beam instruments. The rapid response of the device allows up to 100 kHz update rates, making it possible to do on-the-fly auto-tuning of differential contrast schemes without a noticeable recording time penalty for the user. The examples demonstrate the potential for a rich field of emerging applications offered by the phase degree of freedom. Immediate use cases focus on electron microscopy, but other electron beam instruments, such as, e.g., e-beam lithography or semiconductor inspection tools, could also profit significantly from this realization. With an even broader perspective, we demonstrate here the arbitrary preparation of coherent quantum states that might be exploited in novel quantum information/computing schemes over a much wider range of electron energies than the ones demonstrated here.

4.A Defocused Images of the Phase Plate



The defocused images of the phase plate with a voltage applied to one pixel in each ring and the difference map between images with and without excited pixel. The changes in the interference patterns imply a local phase shift which is revealed by the phase reconstruction algorithm.

4.B Pixel Index



Positions of the pixels and their corresponding indices.

Chapter

Retrieval of phase information from low-dose electron microscopy experiments: are we at the limit yet?

This chapter is based on:

Vega Ibañez, F., & Verbeeck, J. (2025). Retrieval of phase information from low-dose electron microscopy experiments: are we at the limit yet? Accepted, Microscopy and Microanalysis,

Contents

Contents						
5.1	Introduction	68				
5.2	Setup	69				
5.3	Recovering the phase and estimating its precision	71				
	5.3.1 Zernike Phase Contrast	71				
	5.3.2 Phase Retrieval through inversion	78				
	5.3.3 Maximum Likelihood model under Poisson noise	80				
5.4	Numerical exercise for 4 unknown phases (1D)	82				
5.5	Numerical exercise for a small 2D case	82				
5.6	A more realistic 2D object					
5.7	Discussion	86				
	5.7.1 The role of dose	86				
	5.7.2 Is RPI the best we can do?	87				
	5.7.3 Technological difficulties to realize this	88				
	5.7.4 A note on re-normalisation	88				
5.8	Conclusion	89				

Summary

The challenge of imaging low-density objects in an electron microscope without causing beam damage is significant in modern TEM. This is especially true for life science imaging, where the sample, rather than the instrument, still determines the resolution limit. Here, we explore whether we have to accept this or can progress further in this area. To do this, we use numerical simulations to see how much information we can obtain from a weak phase object [224] at different electron doses. Starting from a model with four phase values, we compare Zernike phase contrast with measuring diffracted intensity under multiple random phase illuminations to solve the inverse problem. Our simulations have shown that diffraction-based methods perform better than the Zernike phase contrast method, as we have found and addressed a normalization issue that, in some other studies, led to an overly optimistic representation of the Zernike setup. We further validate this using more realistic 2D objects and found that random phase illuminated diffraction can be up to five times more efficient than an ideal Zernike implementation. These findings suggest that diffraction-based methods could be a promising approach for imaging beam-sensitive materials and that current low-dose imaging methods are not yet at the quantum limit.

5.1 Introduction

In this chapter, we aim to revisit the longstanding issue of phase reconstruction in TEM [189,210,225–228] and examine it from the perspective of information transfer. As mentioned in section 1.1.3, in electron microscopy we detect electron events as their wavefunction collapses onto an electron detector. More specifically, the amplitude squared of the wavefunction gives the distribution across camera space. The problem arises from the *loss* of the phase during the detection process, which significantly restricts the information obtainable from an electron microscope experiment. This issue is particularly challenging in electron diffraction experiments, as it hinders the extraction of the projected periodic potential of a crystal. Moreover, it is also highly relevant in imaging non-periodic thin objects in TEM, where the object's projected density information is predominantly encoded in the phase profile imparted on the coherent plane wave illumination. Recent attempts to apply diffraction-based imaging, e.g., to viruses [229] or in single particle analysis [230, 231] show great potential and are accompanied by promising simulation studies [232–234].

We will use the toolset of parameter estimation, which has shed light on similar problems in TEM, like investigating point resolution in the presence of noise [235], the advantage of a monochromator on the spatial resolution in TEM [236], determining the precision of measuring atomic positions from exit waves [237], or even determining elemental concentrations from electron energy loss experiments [238,239].

The issue of phase retrieval under dose-limited conditions has sparked significant debate within the scientific community. Egerton et al. conducted groundbreaking research to assess the instrument's limitations [240] and evaluated different commonly used TEM and STEM imaging methods on beam-sensitive specimens [241]. In the following years, more theory was incorporated to assess the efficiency of phase retrieval by incorporat-

ing robust mathematical concepts such as the Fischer Information (FI) and Cramér-Rao Lower Bound (CRLB) [242–244]. Based on these mathematical concepts, Koppell and Kasevich constructed a function to assess the inherent frequency transfer of the imaging system [245]. More recently, Dwyer and Paganin directly compared Zernike Phase Contrast (ZPC) and 4D-STEM with a phase-structured illumination [246]. All this notable work has paved the way and opened the debate for a more comprehensive assessment of phase retrieval in the TEM, with the general conclusion that ZPC seemed to be the best method to maximize information transfer. Ultimately, this conclusion has put limits on the hope for ptychographic methods to create a breakthrough in low-dose phase imaging [189,215,247–250]. Here, we revisit this problem by conducting a series of numerical exercises. Furthermore, we will carefully consider the normalization conditions to enable a fair comparison between image-based reconstruction using ZPC and phase retrieval through diffraction-based recording. We demonstrate that at least under the idealised conditions considered here, a significant improvement over ZPC in low-dose phase imaging is possible with diffraction-based detection.

5.2 Setup

In the following section, we want to present this process as a type of *game* where the sample is imagined to contain a hidden message consisting of N phase values, denoted as ϕ_i in fig. 5.1. We illuminate the sample with an electron wave and observe the outcome of this interaction on M ideal electron detectors, labeled as I_i in fig. 5.1. From this simple setup, two natural questions arise:

- How many electrons do we need to *fire* onto the sample to obtain the secret message at the required precision and accuracy?
- How can the experiment be set up to achieve the best precision and accuracy with the fewest electrons and, thus, the least beam damage?

These questions are fundamental in modern electron microscopy, as the resolution of EM is in many practical cases limited by beam damage and not anymore by the instrument [86, 230, 231, 251–255]. This means we must either learn new techniques to limit beam damage or utilize the most efficient imaging methods to maximize the use of the electron dose the sample can withstand [256] (preferably a combination of both).

In this study, we will avoid all complications regarding the scattering that happens within the sample, details of imperfect optical systems [257,258], propagation effects [259,260], multiple scattering in the sample [89, 261–264], inelastic scattering [265–270], partial coherence [221,271–275], and details of the algorithmic implementation [170,276] to gain some clarity on how far we are from fundamental limits.

We start with a conceptual exercise to estimate four hidden phases as sketched in fig. 5.1. We compare two typical setups: On the one hand, we use a Zernike Phase Plate (ZPP) for phase contrast imaging, which is commonly considered the golden standard in real-space phase imaging and is used extensively in, e.g., life science imaging [131, 132, 171, 172]. The benefit of this method is that it results directly in an image of the sample with a

contrast that relates approximately linearly to the phase shift, which is proportional to the projected electrostatic potential of a weakly scattering thin sample in a TEM.

On the other hand, we can detect the scattered electrons in the diffraction plane, as is commonly done to investigate symmetries and periodicity in crystals. This pattern also encodes the information of the specimen, albeit in a different way, and requires some inverse algorithm to link the recorded intensities to the projected sample potential we are interested in.

In either case, retrieving the *absolute phase* will be impossible as we have no unperturbed reference beam to compare. Due to this lack of a reference beam, only three of the four unknown phases are independent, somewhat simplifying the problem from N to (N-1) unknowns represented as $\phi_N = -\sum_1^{N-1} \phi_i$.

Because either a translation or an inversion of the object leaves the diffraction intensities unchanged, we have a good chance of ending up with a wrong guess of the secret sample for the diffraction-based setup [223,277]. A typical way to solve this is to oversample the diffraction plane (M > N), which stabilizes the solution at the expense of requiring more detector pixels. Another way to proceed is by introducing an amplitude [278–280] or phase [144,281,282] modulator capable of encoding the electron wavefront for $N_{config.}$ sets of conditions. In this section, we concentrate on pure phase modulation and do not examine the specifics of how to construct a programmable phase modulator, as that has already been covered in chapter 3 and chapter 4. We will assume the modulator works perfectly, similar to our assumption for the ZPP.

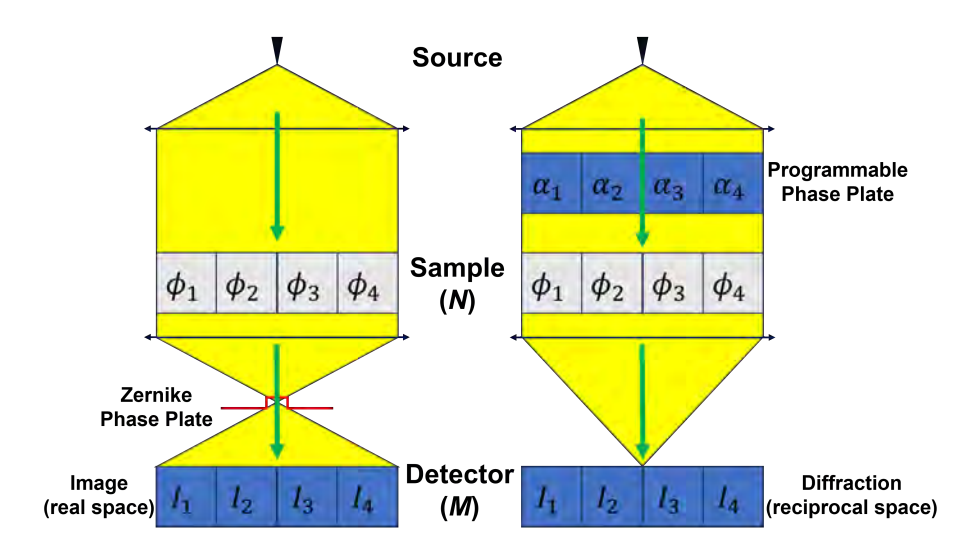


Figure 5.1: Sketch of the setup. The aim is to measure the N phases of the unknown object by illuminating it with a coherent electron wave and detecting the arrival of electrons with an ideal detector consisting of M independent pixels. The left-side setup shows the configuration with an ideal ZPP, while the right-side setup describes the detection in the diffraction plane with a programmable phase input wave. We will compare the performance of both setups in terms of phase error on the estimate as a function of the amount of electrons we have available in the experiment.

Suppose we choose a number of known Random Phase Illumination (RPI) conditions N_{RPI} , and we solve the inverse problem by taking into account the N_{RPI} independent measurements to resolve one unique estimate of the object phase. We now obtain some robustness against inversion and translation since the extra configurations yield $M \times N_{RPI}$ measurement points (far more than the N unknown phases we want to recover).

In order to implement this scheme, we use a non-linear Maximum Likelihood (ML) fitting algorithm with (N-1) unknown phases and a likelihood function assuming Poisson counting noise that describes how likely it is that a given experimental realization of $M \times N_{RPI}$ diffraction intensities could have been produced when assuming a given set of (N-1) sample phases [283,284]. This iterative non-linear fitting process is significantly slower than the more common Gerchberg-Saxton (GS) [187] algorithm. Still, it allows the correct treatment of the Poisson statistics and obtaining estimates for the connection between phase errors and the counting statistics through the use of the CRLB [284,285]. We can use this to compare the behavior of the GS algorithm with ML prediction, further confirming that it approaches the same fundamental limit while providing the significant speed-up necessary for realistic image sizes.

5.3 Recovering the phase and estimating its precision

Our objective is to accurately determine the unknown phase from either a real-space or diffraction-space intensity recording. We will use the ZPC method for real-space as a standard, and in the case of the diffraction experiment, we will need to solve the inversion problem. To do so, we will utilize parameter estimation to understand its statistical properties and, later, use a GS algorithm that can approach these while providing a significant numerical speed advantage.

5.3.1 Zernike Phase Contrast

In Zernike phase contrast [131, 132], a phase plate is placed in the BFP of the objective aperture, which shifts only the low-frequency component of the wave by $\pi/2$. As a result, the image contrast now reveals the phase of the object.

Although ZPC presents a seemingly straightforward process for image formation, accounting for its dose efficiency can be quite complex due to the various normalization factors that come into play. In this section, we will numerically derive the image formation process for ZPC and highlight the key assumptions that must be made to properly normalize it and evaluate its dose efficiency.

We begin by assuming a coherent circular area of illumination on a sample with radius *R*:

$$M(r) = \Pi\left(\frac{r}{2R}\right) \tag{5.1}$$

With $\Pi(x)$ the Heavyside Pi step function (or rect function) being one for $|x| < \frac{1}{2}$.

And the sample transmission function can be approximated as a phase object:

$$O(\mathbf{r}) = e^{i\phi(\mathbf{r})} \tag{5.2}$$

Illuminating a sample with a coherent circular electron wave in the BFP will then result in:

$$\Psi(\mathbf{k}) = \tilde{M}(\mathbf{k}) \otimes \tilde{O}(\mathbf{k}) = \frac{2J_1(kR)}{kR} \otimes \tilde{O}(\mathbf{k})$$
 (5.3)

With $\tilde{}$ designating the Fourier transformed function and J_1 a Bessel function of the first kind. Experimental implementations of a ZPP in the TEM, such as the Volta Phase Plate, typically exhibit a smooth phase profile resembling an Airy function [174, 286, 287]. Nonetheless, in our case, to create an idealized ZPP, we define a maximum passband frequency, k_{max} , which represents the highest spatial resolution achievable, and a minimum frequency, k_Z . Below this minimum frequency, we introduce a required phase shift of $\pi/2$, modeled as a Heaviside step function. An ideal ZPP would have $k_Z \to 0$ and $k_{max} \to \infty$. However, as we will discuss later, these parameters are crucial for normalization and play a significant role in the context of quantum information.

Following this, we can then write the maximum passband and the ZPP in the BFP as:

$$Z(\mathbf{k}) = \Pi\left(\frac{k}{2k_{max}}\right) \exp\left[i\frac{\pi}{2}\Pi\left(\frac{k}{2k_z}\right)\right]$$
 (5.4)

For $k_{max} > k_z$, and we can rewrite this as:

$$Z(\mathbf{k}) = \Pi\left(\frac{k}{2k_{max}}\right) + \Pi\left(\frac{k}{2k_z}\right)(i-1)$$
 (5.5)

Applying this phase plate in the BFP leads to:

$$\Psi_Z(\mathbf{k}) = \left[\frac{2J_1(kR)}{kR} \otimes \tilde{O}(\mathbf{k}) \right] Z(\mathbf{k})$$
 (5.6)

And, transforming this back to the image plane, we get:

$$\tilde{\Psi}_{Z}(\mathbf{r}) = [M(\mathbf{r})O(\mathbf{r})] \otimes \tilde{Z}(\mathbf{r})$$
(5.7)

Now, we can rewrite the Fourier transform of the ZPP as:

$$\tilde{Z}(\mathbf{r}) = \frac{2J_1(rk_{max})}{rk_{max}} + \frac{2J_1(rk_z)}{rk_z}(i-1)$$
(5.8)

The first term will produce a replica of the object with a spatial resolution limit of $1/k_{\rm max}$. In contrast, the second term will create a blurred version of the illuminated area, with the blurring determined by a Bessel function with a width of $R_Z = 1/k_Z$. This blurred version will act as a reference wave, enhancing the phase contrast when it interferes with the first term.

Notably, the blurring will draw intensity from the illuminated area as well as from the surrounding area, which does not carry any useful information. This aspect is crucial

for understanding the impact of counting noise since not all electrons will contribute to the desired ZPC signal.

The blurring reduces the local intensity by a factor C, which can be estimated in the center of the image as:

$$C = \int_0^{Rk_z} \frac{2J_1(k)}{k} dk {(5.9)}$$

$$= [\pi R k_z H_0(R k_z) - 2] J_1(R k_z)$$
 (5.10)

$$+ Rk_z[2 - \pi H_1(Rk_z)]J_0(Rk_z)$$
 (5.11)

$$C \approx Rk_z \tag{5.12}$$

With H_0 and H_1 Struve functions of zeroth and first order, respectively [288]. The simplification in the final step becomes an accurate approximation when $Rk_z < 1$. To ensure this condition is met, we can set $Rk_z = \frac{R}{R_z} \leq \frac{1}{2}$. This choice is essential to retain all frequency components except for the DC frequency, as choosing higher values would lead to the loss of low-frequency components. Under these conditions, the exit wave for $r \leq R$ can be rewritten as:

$$\Psi(\mathbf{r}, r \le R, R/R_7 \le 1/2) = O(\mathbf{r}) + (i - 1)C^2 \langle M(\mathbf{r})O(\mathbf{r}) \rangle$$
 (5.13)

With $C \approx R/R_z$ and $\langle M(\mathbf{r})O(\mathbf{r}) \rangle$ the averaged exit wave inside the illuminated patch M caused by the convolution of the Heavyside and Airy pattern with $radius\ R$ and R_z , respectively. This convolution will re-scale this reference wave by a factor C^2 because part of this wave now ends up outside the illumination patch in the image plane. Applying the Weak Phase Object Approximation (WPOA) and assuming the phase of the object does not contain spatial frequency variations above k_{max} we get:

$$O(\mathbf{r}) \approx 1 + i\phi(\mathbf{r})$$
 (5.14)

$$\Psi(\mathbf{r}, r \le R, R/R_z \le 1/2) \approx 1 + i\phi(\mathbf{r}) + (i-1)C^2$$
 (5.15)

$$I_{z}(\mathbf{r}, r \leq R, R/R_{z} \leq 1/2) \approx |\Psi(\mathbf{r}, r \leq R, C \leq 1/2)|^{2}$$

$$\approx (1 - C^{2})^{2} + (\phi(\mathbf{r}) + C^{2})^{2}$$

$$\approx 1 - 2C^{2} + 2C^{4} + 2C^{2}\phi(\mathbf{r})$$

$$+\phi(\mathbf{r})^{2}$$

$$\approx 1 - 2C^{2} + 2C^{4} + 2C^{2}\phi(\mathbf{r})$$

Where, due to the WPOA ($\phi(\mathbf{r}) < 1$) [224,289], we assume that a Taylor series expansion up to the linear term is sufficient to approximate our object. The $I_z(\mathbf{r}, r \le R, C \le 1/2)$ term represents the observed intensity in the image plane within the illuminated area, and the average intensity within the illuminated patch is $\overline{I_z(\mathbf{r}, r \le R, C \le 1/2)} \approx 1 - 2C^2 + 2C^4$.

We can recover the phase from the intensity as:

$$\phi(\mathbf{r}, r \le R) \approx \frac{I_z(\mathbf{r}, r \le R) - 1 + 2C^2 - 2C^4}{2C^2}$$
 (5.17)

Furthermore, in a practical implementation, the intensity will be recorded on a pixelated camera, where we assume I_z to be scaled so that, if the ZPP were removed, there would be an average of one electron per pixel. This allows us to estimate the standard deviation of the phase error as:

$$\sigma_{\phi} = \frac{1}{2\sqrt{N_e/n^2}} \frac{\sqrt{1 - 2C^2 + 2C^4}}{C^2}$$
 (5.18)

Where the last term is a correction term that takes care of the role of *C*, which depends on the parameters of both illumination size and scale of the phase shifting part of the phase plate.

The critical thing to note here is that section 5.3.1 only agrees with the conventional ZPC for C = 1. However, in that case, the formula is not valid, as crucial low-frequency information would be missing across the illuminated area because the reference wave generated by the central Zernike phase discontinuity would not be homogeneous. Only if we admit to being interested in a subregion of the illuminated area can we recover the conventional formula at C = 1. It is important to stress here that, in such a case, we create a situation that can no longer act as a fair comparison with the diffraction setup for the following reasons:

- We are illuminating and damaging areas of the sample outside the field of view. We might need those areas later on.
- We use electrons outside the field of view to help create a reference beam inside the field of view. This effectively creates a setup similar to an off-axis holography experiment [290–292] and results in an inappropriate counting of the incoming amount of electrons needed per area. Suppose such an external reference wave can be added at no penalty. In that case, this option should also be offered to the diffraction setup, i.e., by assuming that part of the illuminated field of view is known to be constant or of no interest. This would lower the amount of unknowns and increase the precision as well.
- Even if the area of the sample around the region of interest can be considered uninteresting or sacrificial, the electrons hitting there can still cause damage inside the area of interest via delocalized inelastic scattering [293–295] and diffusion effects [296–298]

Consequently, to recover all spatial frequencies within the illuminated area without creating an implicit reference wave, we choose to take the optimal value of C = 1/2 for the remainder of this work. With that normalization in mind, we can estimate the standard deviation of the phase error for N_e electrons as:

$$\sigma_{\phi,Z,2D} = \frac{\sqrt{1 - 2C^2 + 2C^4}}{2C^2 \sqrt{N_e/(N-1)}} \xrightarrow{C=1/2} \frac{\sqrt{10}}{2\sqrt{N_e/(N-1)}}$$
(5.19)

Which is $\sqrt{10} \approx 3.16$ times *higher* than what we would get assuming the wrongly normalized conventional solution. Note that, for a 1D case, the normalization penalty is less severe:

$$\sigma_{\phi,Z,1D} = \frac{\sqrt{1 - 2C + 2C^2}}{2C^2 \sqrt{N_e/(N - 1)}} \xrightarrow{C=1/2} \frac{\sqrt{2}}{2\sqrt{N_e/(N - 1)}}$$
(5.20)

Numerical implementation of Zernike contrast

In addition to the previous section's discussion, the numerical implementation of ZPC is essential for accurately estimating the method's dose efficiency. In the numerical case, an additional aliasing error often arises due to the incorrect assumption that both the illumination and the sample repeat periodically and indefinitely. In reality, this assumption presents challenges, as we typically do not work with perfectly periodic structures; otherwise, diffraction-based measurements would be more suitable. Even in scenarios where periodic structures are relevant, it is nearly impossible to align the illumination box with the periodic boundaries perfectly.

These assumptions create a situation similar to the C=1 case but without the disadvantage of losing low-frequency information. This ultimately leads to overestimating the information obtainable from a ZPC implementation. This subtle error may explain why previous numerical studies have provided an overly optimistic perspective on the influence of counting noise [246, 299]. To address this issue, we offer a numerical reference implementation alongside this work [300].

As the intensity recording involves a modulus squared, which relates to the autocorrelation in the image plane, proper zero padding is only guaranteed with at least n/2 padding on all sides for an $n \times n$ illumination area. Padding more will worsen the counting statistics further; padding less will lead to a nonphysical situation as it cannot be replicated in an actual experiment.

In a numerical experiment, we can use the crudest approximation of a ZPP by creating a $M = m \times m$ filter matrix in the discrete Fourier plane with all ones and only the DC component in the top left corner equal to the complex i. We can decompose this filter into a sum of a matrix with all ones and another matrix with all zeros except for the DC component, which we take as (i - 1). Fourier transforming this will result in the sum of two matrices, one of which has only a DC component equal to 1 and the other a flat matrix with elements (i - 1)/M (see fig. 5.2). We can now simulate the action of this filter by convolving this real space representation of the Zernike filter kernel with an object. If we choose the object first to be the same size as the filter kernel (M = N), we get:

$$\Psi_Z(\mathbf{r}) = O(\mathbf{r}) + M \frac{(i-1)}{M} < O(\mathbf{r}) >$$
 (5.21)

$$\Psi_Z(\mathbf{r}) = 1 + i\phi(\mathbf{r}) + i - 1 \tag{5.22}$$

$$\Psi_Z(\mathbf{r}) = \mathbf{i} + \mathbf{i}\phi(\mathbf{r}) \tag{5.23}$$

$$I_Z(\mathbf{r}) = 1 + 2\phi(\mathbf{r}) + \phi(\mathbf{r})^2 \tag{5.24}$$

$$I_Z(\mathbf{r}) \approx 1 + 2\phi(\mathbf{r})$$
 (5.25)

From which we can derive the phase unambiguously from the intensity:

$$\phi(\mathbf{r}) \approx \frac{I_Z - 1}{2} \tag{5.26}$$

And this looks exactly like we would expect from a ZPP. Consequently, the standard deviation on the phase now becomes:

$$std(\phi(\mathbf{r})) = \frac{1}{2\sqrt{N_e/M^2}}$$
(5.27)

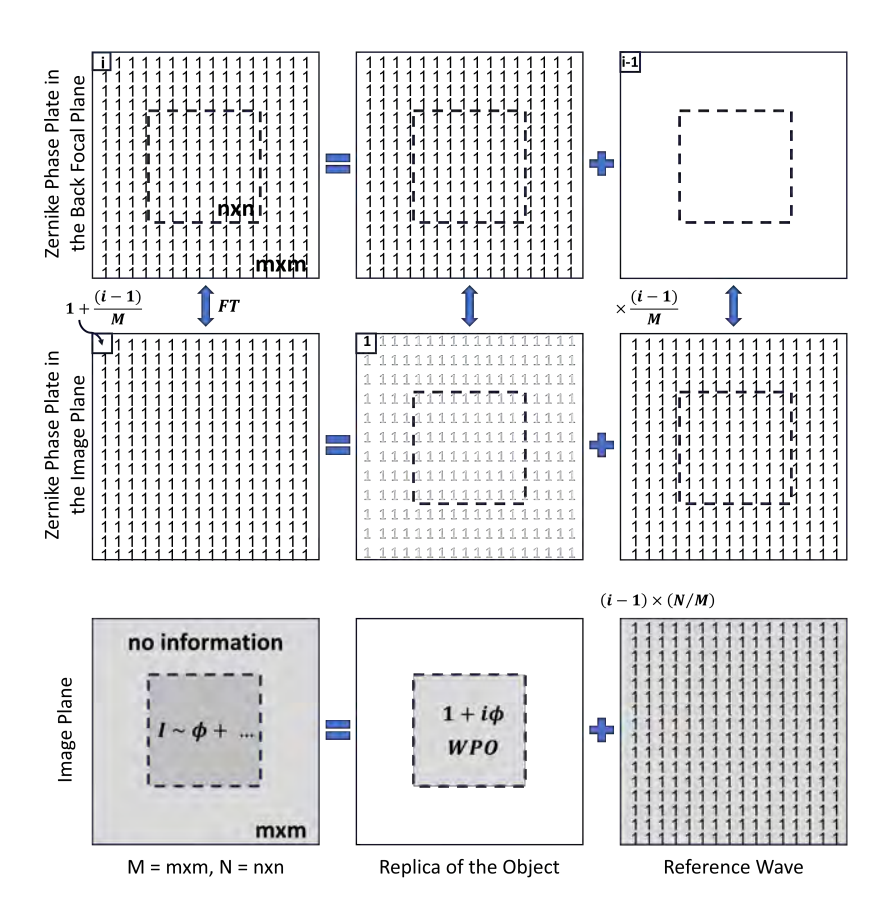


Figure 5.2: Sketch of a numerical 2D implementation of ZPC imaging that avoids aliasing effects that would lead to errors in estimating the quantum efficiency of the ZPC imaging process.

Again, this result is why ZPC is believed to outperform diffraction-based methods in [301].

If, on the other hand, we choose to limit the illumination of the object only to fill $N = n \times n$ pixels, we get a different result with $C = \sqrt{N/M}$, which is again the oversampling factor shown in section 5.3.1.

If $M \ge 4N$, the averaging kernel smears the object over the entire matrix but does not extend beyond its borders, thus avoiding aliasing. In physics terms, the reference wave used to reveal the phase is derived solely from the illuminated $n \times n$ patch rather than neighboring sample areas. This is an improvement over the N=M case, where the sample is incorrectly assumed to be periodic.

While it might seem acceptable that the averaging process does not require the sample to be perfectly periodic, the use of electrons from neighboring areas introduces issues, including potential damage to those regions. Additionally, the averaged reference wave spreads over a larger image plane area $(m \times m, \text{ provided } m \ge 2n)$, which exceeds the $n \times n$ illuminated region of interest. Consequently, a significant fraction of electrons falls outside the region of interest, contributing no meaningful information about the illuminated sample area.

We are now able to estimate what fraction of the illumination contributes to the ZPC phase signal. Outside and inside the illuminated area, we get an average intensity of:

$$\tilde{I}_{Z,out} \approx 2C^4$$
 (5.28)
 $\tilde{I}_{Z,in} \approx 1 - 2C^2 + 2C^4$ (5.29)

$$\tilde{I}_{Z,in} \approx 1 - 2C^2 + 2C^4$$
 (5.29)

For an oversampling of C = 1/2, the average intensity is 1 - 2/4 + 1/8 = 5/8 inside and 3/8 on the outside, as demonstrated in fig. 5.3. All intensity is now spread over 4 times more area in real space than before, and only the central quarter will contain information on the sample phase. That central patch only contains 5/8 of the illumination, but even that 5/8 contributes less than in the aliased (and therefore wrong) ZPC case because the strength of the averaged reference beam is also reduced.

For 1D, we have N = n, M = m, and C=1/2. This would be 1/2 inside and 1/2 outside, leading to half the intensity not contributing to the area of interest.

The standard deviation on the phase now becomes:

$$std(\phi_{Z,aliased}) = \frac{1}{2\sqrt{N_e/N}}$$
 (5.30)

$$\frac{std(\phi_{Z,2D})}{std(\phi_{aliased})} = \frac{\sqrt{1-2C^2+2C^4}}{C^2}$$
 (5.31)

$$\frac{std(\phi_{Z,1D})}{std(\phi_{aliased})} = \frac{\sqrt{1-2C+2C^2}}{C}$$
 (5.32)

For the minimal required oversampling of C = 1/2, we get

$$\frac{std(\phi_{Z,2D})}{std(\phi_{aliased})} = \sqrt{10}$$
 (5.33)

$$\frac{std(\phi_{Z,2D})}{std(\phi_{aliased})} = \sqrt{10}$$

$$\frac{std(\phi_{Z,1D})}{std(\phi_{aliased})} = \sqrt{2}$$
(5.33)

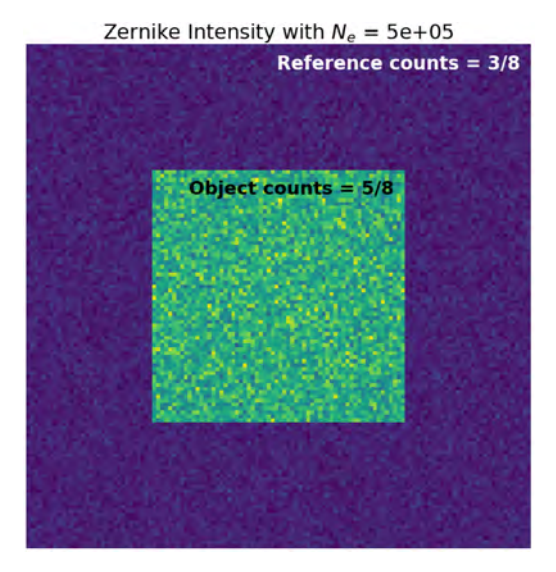


Figure 5.3: Example of a correctly sampled ZPC image of a random phase object of 64×64 zero-padded to 128×128 with $N_e = 5 \times 10^5$. The central 64×64 area contains the actual phase-related image and 5/8 of the total dose with which the object was illuminated. The other 3/8 lands outside the central area and does not contribute to the desired information.

Identical to the real space derivation as it should be.

5.3.2 Phase Retrieval through inversion

After discussing the implementation of ZPC from both physical and numerical perspectives, we will introduce a diffraction-based methodology as an alternative approach. As mentioned earlier, our main objective is to extract the hidden phase values from a model. This methodology allows for a fair comparison of different techniques, enabling us to evaluate the maximum amount of information each method can provide and how this aligns with the theoretical limit.

While dose efficiency remains a critical factor, if we set it aside, we can highlight another challenge: Interpreting diffraction data is inherently less straightforward than using the ZPC method, as it requires inversion to be meaningfully represented in real space. Therefore, it is essential to carefully describe our inversion method to fully understand how the phase is recovered from the diffraction measurements.

Inversion via parameter estimation

Estimating the parameters of a forward model is a simple method for determining the unknown phases from a recorded diffraction pattern [302]. We can model the object as

a discrete pure-phase object:

$$S_i = e^{i\phi_i} \tag{5.35}$$

Then, we can describe the illumination over this object with a wave function:

$$\Psi_i = A_i e^{i\alpha_i} \tag{5.36}$$

Where A_i represents the amplitude of the illuminating wave, and the exponential term accounts for the spatially encoded phase over the illumination patch ($\alpha_i \to \alpha_i(\mathbf{r})$). To enable both amplitude and phase modulation, although only phase is utilized here, we can express the exit wave of the object as:

$$\Psi_i = A_i e^{i(\phi_i + \alpha_i)} \tag{5.37}$$

Moreover, we record the diffraction intensities as follows:

$$I_{model,j} = |\mathcal{F}_j \Psi_i|^2 \tag{5.38}$$

With \mathcal{F}_j representing the Fourier transform operator, which projects the wave onto the BFP where the detection process occurs.

Inversion via the Gerchberg-Saxton algorithm

The GS algorithm and its variations are iterative methods used to recover phase information from intensity measurements of a complex-valued wave function [187, 188, 303–305]. In our case, starting from a set of intensity recordings in diffraction space $\hat{I} = \{I_1, I_2, \cdots, I_{N_{RPI}}\}$, and their corresponding known illumination patterns in real space $\hat{\Psi} = \{\Psi_1, \Psi_2, \cdots, \Psi_{N_{RPI}}\}$, we aim to retrieve the (N-1) missing phases of an object \hat{S} . To do this, we can start by guessing our solution \hat{S}_0^{\star} as a set of N complex numbers with amplitude 1 and random phases $\phi_i \in [-\pi, \pi)$, illuminated by the complex-valued waves from each N_{RPI} measurement in diffraction space. And, in general, for any given iteration:

$$\hat{\varphi}_{out,i}^{\star} = \mathcal{F}[\hat{S}_i^{\star} \hat{\Psi}] \tag{5.39}$$

From this, we can impose the constraint of our recording in diffraction space and reconstruct our guessed $\hat{\varphi}_{out,i+1}^{\star}$ as:

$$\hat{\varphi}_{out,i+1}^{\star} = \frac{\hat{\varphi}_{out,i}^{\star}}{\|\hat{\varphi}_{out,i}^{\star}\|} \sqrt{\hat{I}} \times \text{Phase}\left(\hat{\varphi}_{out,i}^{\star}\right)$$
 (5.40)

Where the Phase operator returns the phase of the given array, respectively. From this, we can back-propagate $\hat{\varphi}_{out,i+1}^{\star}$ to real space and obtain a new estimate for the object:

$$\hat{S}_{i+1}^{\star} = \text{Average}\left(\mathcal{F}^{-1}[\hat{\varphi}_{out,i+1}^{\star}]\hat{\Psi}_{in}^{\dagger}\right)$$
 (5.41)

With $\hat{\Psi}_{in}^{\dagger}$ being the complex conjugate of the transposed illumination pattern wave set. This process is then carried out iteratively until a set number of iterations or a convergence condition is met.

It is important to note that in eq. (5.41), the update takes the average contribution from each of the N_{RPI} illuminating patterns. This helps reduce the typical twin and translational artifacts in the Fourier transform when $N_{RPI} > 1$. For $N_{RPI} = 1$, we will encounter a similar problem to that of ZPC, where oversampling is needed to solve all N phase values in our object.

5.3.3 Maximum Likelihood model under Poisson noise

After establishing our inversion models for the interaction between our sample and object, we can define a maximum likelihood estimator (MLE) based on the assumption that detection in the diffraction plane is governed by counting noise and that each detector pixel is independent. By establishing this, we can assess our phase retrieval method's accuracy and dose efficiency, as it provides the ultimate limit in information transfer for a given electron budget (N_e).

We can write the log-likelihood *l* [306] as:

$$l = -\sum_{l}^{N} (I_{exp,l} \ln(I_{model,l}) - I_{model,l})$$
 (5.42)

With $I_{exp,l}$ the experimental observation and $I_{model,l}$ the model prediction, which is based on a set of detector pixel l parameters. We can derive $I_{model,l}$ from the exit wave as:

$$\Psi_i = A_i e^{i(\phi_i + \alpha_i)} \tag{5.43}$$

$$I_{model,l} = \left| \mathcal{F}_l A_i e^{i(\phi_i + \alpha_i)} \right|^2 \tag{5.44}$$

$$I_{model,l} = \left| \sum_{i} A_{i} e^{i(\phi_{i} + \alpha_{i})} e^{2\pi i \mathbf{r}_{i} \cdot \mathbf{k}_{l}} \right|^{2} = |\tilde{\Psi}_{l}|^{2}$$
 (5.45)

Differentiating the log-likelihood from the parameters of the model gives:

$$\frac{\partial l}{\partial \phi_i} = -\sum_{l} \left(\frac{I_{exp,l}}{I_{model,l}} - 1 \right) \frac{\partial I_{model,l}}{\partial \phi_i}$$
 (5.46)

By differentiating the model intensities from the model parameters, we get:

$$\frac{\partial I_{model,l}}{\partial \phi_i} = -2A_i \mathbf{R} \mathbf{e} \tilde{\Psi} \sin(\phi_i + \alpha_i + r_i k_l) + 2A_i \mathbf{I} \mathbf{m} \tilde{\Psi} \cos(\phi_i + \alpha_i + r_i k_l)$$
(5.47)

Suppose we constrain the last phase value ϕ_N to maintain an average phase of zero (the absolute phase has no meaning, and fitters typically struggle with duplicate parameters). In that case, we need to take into account this dependent variable. So, we proceed now with (N-1) independent parameters:

$$\frac{\partial I_{model,l}}{\partial \phi_i} = -2\mathbf{Re}\tilde{\Psi}_l[A_i \sin(\phi_i + r_i k_l + \alpha_i) - A_N \sin(\phi_n + r_n k_l + \alpha_n)] + 2\mathbf{Im}\tilde{\Psi}_l[A_i \cos(\phi_i + r_i k_l + \alpha_i) - A_N \cos(\phi_n + r_n k_l + \alpha_n)]$$
(5.48)

5.3. RECOVERING THE PHASE AND ESTIMATING ITS PRECISION

Using this analytical derivative as a Jacobian input for the non-linear fitter significantly speeds up the process and improves convergence.

We can now derive the Fisher information matrix [307]:

$$F_{i,j} = -E \left[\frac{\partial^2 l}{\partial \phi_i \partial \phi_j} \right]$$

$$= \sum_{l} \frac{\partial}{\partial \phi_j} \left(\frac{I_{exp,l}}{I_{model,l}} - 1 \right) \frac{\partial I_{model,l}}{\partial \phi_i}$$
(5.49)

$$+\left(\frac{I_{exp,l}}{I_{model,l}}-1\right)\frac{\partial I_{model,l}}{\partial^2 \phi_i \partial \phi_i} \tag{5.50}$$

$$= -\sum_{j} \frac{1}{I_{model,l}} \frac{\partial I_{model,l}}{\partial \phi_{i}} \frac{\partial I_{model,l}}{\partial \phi_{j}}$$
 (5.51)

Moreover, we can obtain the $(N-1) \times (N-1)$ covariance matrix:

$$cov = F^{-1} \tag{5.52}$$

From which the diagonal elements represent the CRLB [284,308] of the variance on the individual phase estimates $\tilde{\phi}_i$. This allows us to write a lower limit for the standard deviation on the estimated parameters as:

$$\sigma_{ML} \ge \sqrt{\frac{\text{Tr}(cov)}{N-1}} \tag{5.53}$$

With Tr() the Trace operator.

We can further estimate the CRLB from a more fundamental perspective. We detect in the reciprocal plane where, in principle, information related to the phase of the object is encoded in both amplitude and phase in that plane. As a result, we can, at best, obtain an average of half of the information, as we have assumed no prior information about the object. We could, therefore, assume that the CRLB will be close to the following:

$$CRLB \approx \frac{\sqrt{2}}{2\sqrt{N_e/(N-1)}} \tag{5.54}$$

This was also given in Eq. 5.20 as the correction for the 1D case in a ZPC system with C = 1/2. However, we will numerically test this idea further on.

This CRLB can estimate the optimal precision of a measurement for a given electron dose. In other words, it indicates the minimum standard deviation achievable from independent measurements of an unknown parameter. The CRLB can then be compared to the actual outcome of a numerical experiment to evaluate whether we can attain it in practice. It can also aid in comparing alternative algorithms (e.g., parameter estimation, GS, or ZPC) to evaluate how close they can approach this limit and check if bias is introduced.

5.4 Numerical exercise for 4 unknown phases (1D)

An example of an outcome of this numerical experiment is given in fig. 5.4 for $N_{RPI} = 16$. We note a logarithmic behavior between phase errors as a function of the total number of electrons, as expected. Furthermore, for this 1D case, both RPI and ZPC perform similarly. This performance also shows that the corrected error prediction for ZPC in section 5.3.1 describes the propagation of the counting noise to the estimated phase quite well. For higher doses (above $N_e = 10^4$ here), the ZPC phase error does not decrease anymore; This is because we have reached the limit of the linearization of the ZPC formula (Eq. section 5.3.1), which also depends on the range of phase modulation δ by the sample (here $\pm \pi/10$). We are, however, more interested in the low-dose performance. Both the ML and GS results are well predicted by the CRLB, showing that, on average, we approach the statistical limit for 100 repeated experiments per electron dose value. It also shows that our rough estimate in section 5.3.3 is reasonably accurate (in this case, it coincides with the ZPC corrected prediction) albeit slightly higher than the actual CRLB that is based on the detailed model. The fact that GS nearly attains the CRLB also gives confidence in this much faster algorithm, which will be needed for larger systems later. We investigated the role of N_{RPI} in the number of random phase illuminations and observed that from $N_{RPI} \ge 2$, we converge to the optimal phase error. This convergence confirms the theoretical prediction in reference [170]. Increasing N_{RPI} leads only to faster convergence, which might benefit larger systems. However, from here on, we will assume $N_{RPI} = 16$ unless otherwise noted. Furthermore, we found that convergence is best for random phases from a uniform distribution between 0 and π . However, other phase modulation ranges for the illumination were tested with similar results, provided that the object's phase range is fixed. Other phase patterns were attempted, such as illuminating with only 1 pixel at a random phase between $-\pi/2$ and $+\pi/2$ for each RPI configuration or using an orthogonal set of waves (e.g., a Hadamard basis set [190]), both of which also yielded good results.

5.5 Numerical exercise for a small 2D case

Changing to a more common 2D configuration, we attempt a 4×4 pixel phase object shown in fig. 5.5.

The diffraction-based recording performs better than the corrected ZPC intensity, increasing dose efficiency by 5. Comparing ML RPI with GS RPI shows that GS attains the CRLB rather well, which gives faith in the algorithm as a faster alternative to ML, allowing for reconstructing larger objects in a reasonable time. The higher number of unknowns also stabilizes the statistical errors, and the observed behavior for 100 random weak phase object realizations results in an average behavior that closely follows the CRLB and ZPC error predictions. In this case, we barely start appreciating the systematic linearization error for the ZPC setup as the overall error has increased due to the higher number of unknowns, which shifts this point to higher doses.

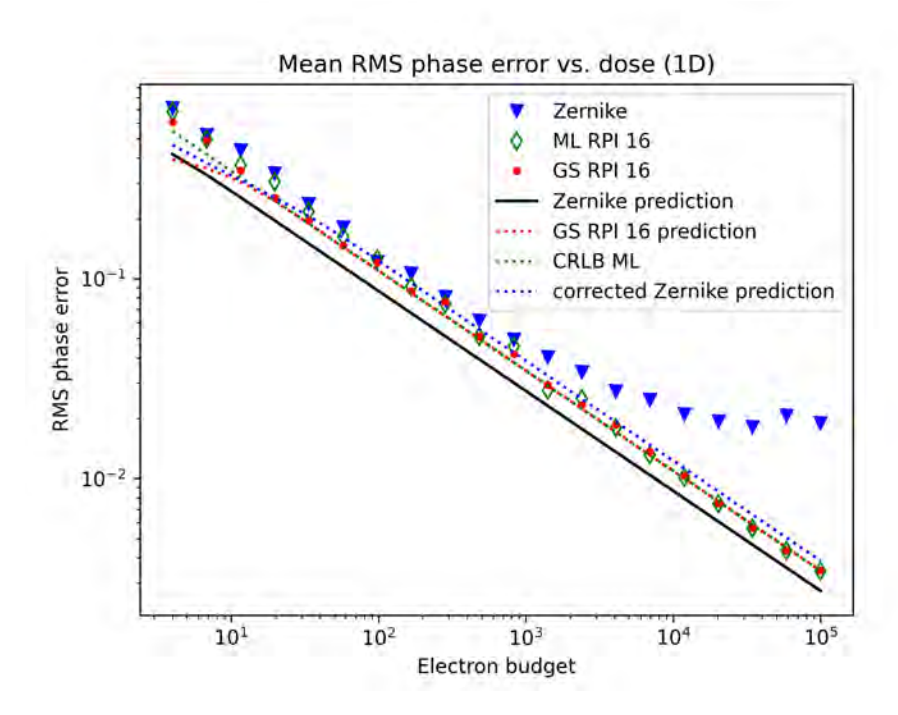


Figure 5.4: Numerical simulation of the average RMS phase error as a function of total electron dose. The object is considered a random phase object with four unknown phase values and a limited phase range of $\pm \pi/10$ to stay within the linear approximation of the ZPC formula. The simulation is repeated 100 times for each electron budget with a different random object. Random phase illumination is done with 16 random illumination patterns that stay the same throughout the simulation set. Note how ZPC and RPI's results closely follow the predicted statistical error and show a similar noise performance up to about $N_e = 10^4$, where systematic errors due to the linearization of the ZPC formula start to show. Note also how ML RPI and GS RPI perform remarkably similarly, giving confidence in the GS approach for larger systems.

5.6 A more realistic 2D object

Due to computational limitations, only the GS algorithm was used for larger objects. As observed in previous examples, it closely approximates the ML CRLB, in agreement with, i.e., ref. [309]. In fig. 5.6, we display the observed Root Mean Squared (RMS) phase error for a 64 × 64 random phase object with a $\pm \pi/10$ phase variation. Both methods effectively retrieve the object at high electron doses, but the standard deviation of the phase error remains about $\sqrt{5}$ higher for the correctly sampled ZPC case. We observe a similar systematic error when $N_e \geq 10^7$, which is expected at higher doses compared to the N=4 1D case. This is because we have to estimate approximately 1000 times more phases, so the experiment requires a dose 1000 times higher to have the same phase error in each pixel. On the low-dose end, we note a peculiar deviation from the error prediction for both ZPC and GS. This occurs because, in both cases, the phase error is bounded. For ZPC, this happens when we get zero counts in a pixel. In that case, the phase is fixed at $\phi_i = -10/8$ rad (for the 2D case), as is obvious from section 5.3.1.

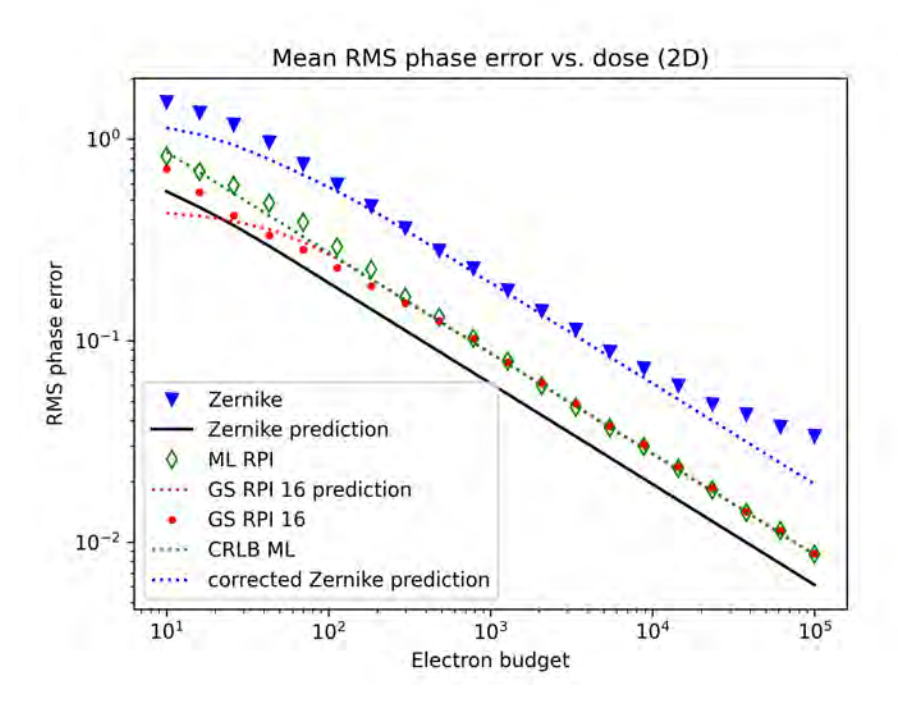


Figure 5.5: Numerical simulation of a 4×4 phase object encoding 100 different realizations of random phase noise with a range of $\pm \pi/10$ for each electron budget. The electron budget is divided over 16 random phase illumination patterns. Note the significant difference with ZPC due to the normalization correction and the close relation between the ML RPI and the much faster GS RPI.

Suppose we now calculate the standard deviation of a truncated normal distribution. In that case, we get an RMS value lower than expected from noise considerations only. This leads to a plateau at a very low dose. Note that this plateau does not mean we gained anything regarding information retrieval but is merely an effect of truncation. This effect is clearly visible in a ZPC image of the famous cameraman [310] (see the top rows of fig. 5.7). When using the lowest dose, most pixels are stuck at the lowest value (-10/8 for the ZPC case), resulting in a low phase error for an object with limited phase variation. However, these pixels do not contain exploitable information about the object either.

The situation is more complex for the RPI measurements. In a GS implementation, we consider RPI a series of N_{RPI} individual measurements. Each of these measurements will have only a fraction of the total dose and, therefore, show a higher error individually. The truncation described above now happens for each realization individually, leading to a phase error plateau lower by $\sqrt{N_{RPI}}$ for the low-dose cases. Naturally, this does not happen for the ML implementation because there is only one model with N phases that are bound between $-\pi$ and $+\pi$, and the $N \times N_{RPI}$ detected intensities are correctly dealt with through the Poisson log-likelihood function, which does not suffer from truncation issues. In order to get the most accurate recorded intensities, it is best to avoid working with dose levels that lead to this plateau. If we need to use GS for computational efficiency, we can do so by choosing $N_{RPI} = 2$ for low-dose cases. Another option is to

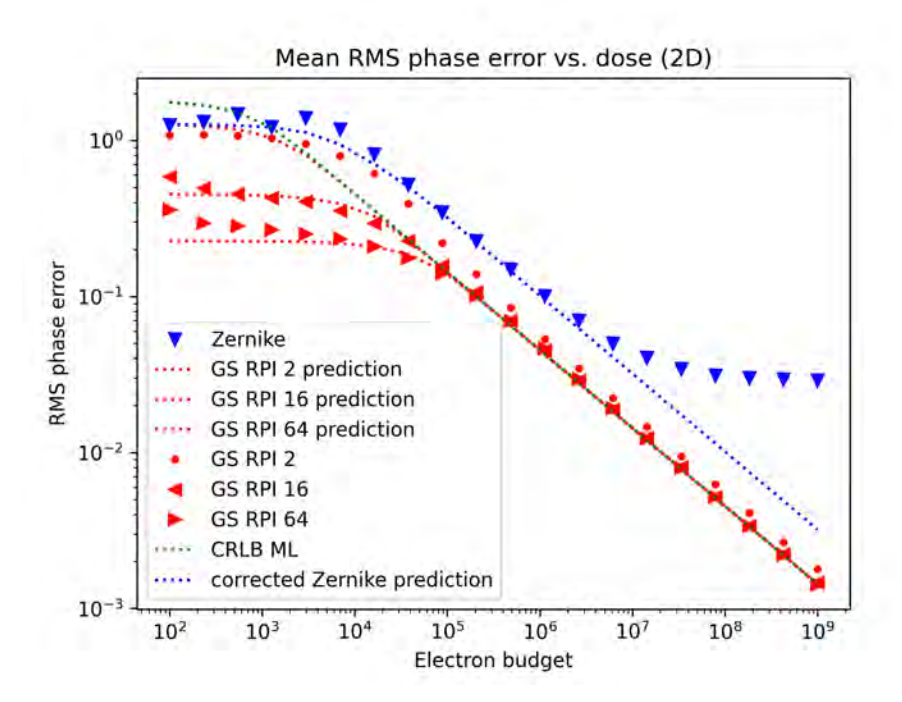


Figure 5.6: RMS phase error for a single 64×64 random phase object with $\pi/10$ phase range, illuminated with $N_{RPI} = 2$, 16, 64. We note that ZPC and GS closely follow their predicted error behavior as a function of the total dose. We note a remarkable trend at low doses where the phase error shows a plateau depending on N_{RPI} , which is a consequence of phase wrapping in the individual N_{RPI} realizations.

use ML and a higher value of N_{RPI} to use the available information fully. However, this will require a longer computation time and does not lead to a significant error reduction. Note that the plateau is also misleading here, as it could lead to the assumption that its lower value, when N_{RPI} is high, constitutes a desirable noise suppression. However, it is merely a truncation or phase-wrapping artifact that obfuscates the actual signal.

When we examine the visual output of the retrieved phase for the cameraman object in fig. 5.7, we can clearly see some significant differences between ZPC and RPI. At the highest dose, both methods accurately retrieve all object details. In the case of ZPC, the intensity is dispersed outside the region of interest, which makes it less effective than the diffraction-based method. We find that only 62.5% of the intensity is within the region of interest, with the remaining 37.5% not contributing useful information from the object. Now we see that, at low doses (marked with a \star in fig. 5.7), the ZPC displays a flat phase of -10/8 rad wherever no electron was detected. While this flat value may seem like low noise due to the absence of contrast variation, in reality, it indicates a lack of information in those areas. This is why we observe a plateau in fig. 5.6 for ZPC. In the case of GS RPI, this effect also arises from phase wrapping of the noise, but it is less prominent, which is also visible in the figure indicated with a \star in fig. 5.7 for RPI.

Furthermore, we also show the detected intensity for the ZPC case to demonstrate the normalization effect that was derived in this chapter. fig. 5.3 shows the detected intensity

of the random phase object of 64×64 . As mentioned above, with correct oversampling of C=1/2, we notice the intensity outside of the illuminated area to be 37.5% of the total illumination intensity. This effect occurs as a result of the phase discontinuity that is essential for ZPC to work but leads to a decrease in dose efficiency, as only a fraction of all electrons take part in the actual formation of the central phase-encoded part of the image and, even there, the contrast is lower. Omitting this oversampling by 2 in all directions will wrongly create an aliasing of the reference part of the wave, which will result in a seemingly 50/50 distribution between the object and the reference part of the wave. This distribution will result in apparently much better counting statistics but consists of an aliasing artifact that can not be reproduced in an actual experiment.

5.7 Discussion

Following the previous derivation and results, we can now extract common features from these numerical exercises and discuss the effect of each parameter on the reconstruction.

5.7.1 The role of dose

The role of dose follows the expected $1/\sqrt{N_e/N}$ trend, albeit with different pre-factors for either ZPC or diffraction-based measurements. This trend shows that the number of detector pixels M should be carefully balanced against the required sampling and desired field of view. We observe a deviating trend at a very low dose due to phase wrapping, which truncates the phase error and leads to a plateau in the error prediction. This plateau indicates a situation where noise is maximized, and it is unlikely that one

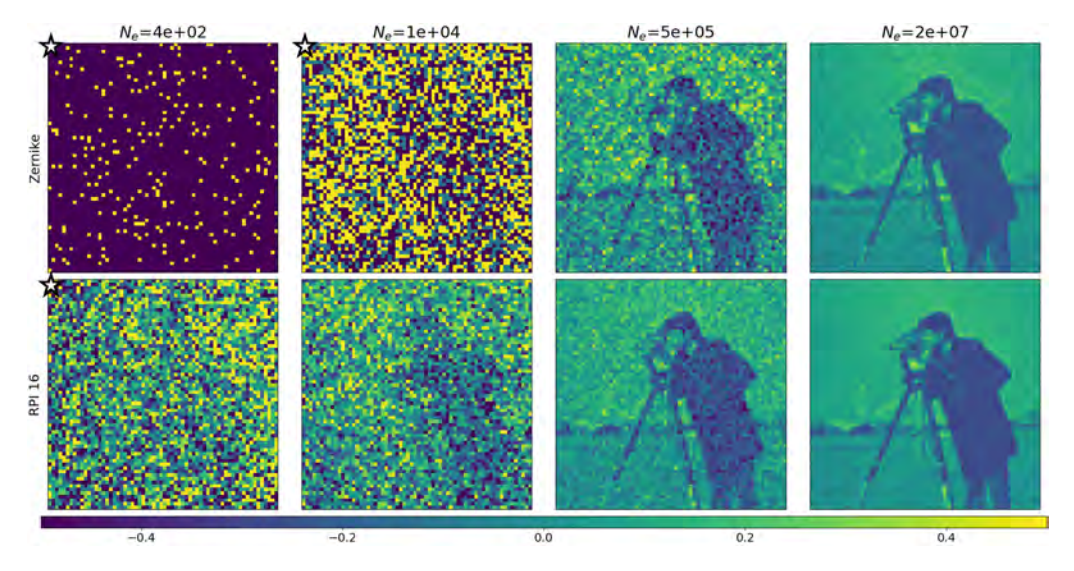


Figure 5.7: Comparison of ZPC and GS RPI phase retrieval as a function of dose on a more realistic 2D object. At high doses, both methods retrieve the object effectively. The top figures marked with a \star do not adhere to the color bar scaling to aid visualization.

would recover any meaningful signal in this range. This truncation effect is more severe for the GS RPI method as it acts on the N_{RPI} individual experiments, while this does not appear for the ML RPI method. This finding is significant, as it guides the experimenter to use a lower N_{RPI} for very low-dose imaging to optimally distribute the available dose among each phase configuration in the illumination. Ideally, ML RPI would always be used, but our current implementation is too slow to be practical on realistically sized objects. Further algorithm development in this direction would be useful. As a side note, we speculate that these effects also occur for ptychography with overlapping probes, as also here, one records multiple instances of the same part of the object with different phase encoding [255, 311–314].

5.7.2 Is RPI the best we can do?

In our study, we employed the RPI method to solve the issue of under-determination in the inverse problem, which helps eliminate translation and point symmetry uncertainties [170]. Although this method provides a five-fold improvement over ZPC, it raises the question of whether it would be more efficient to devise a new illumination scheme based on insights gained from previous experiments rather than recording 16 random phase illumination variants. We explored variations of this approach, such as using the complex conjugate of the current phase estimate, employing orthogonal basis sets like Hadamard and Fourier, and using only $\pm \pi$ phase illumination akin to a charge flipping algorithm [189]. However, these attempts yielded nearly identical results to our simpler random phase illumination scheme.

It is intriguing to consider how we can efficiently encode a phase message using N_e electrons. Assuming that each electron represents one bit of information, then N_e electrons could convey a message with 2^{N_e} variations. If we distribute this across the $N = (n \times n)$ independent pixels, we get:

$$\sigma_{\phi,binary} = \frac{2\pi}{2^{\frac{N_c}{n^2}}} \tag{5.55}$$

This encoding would be significantly more efficient in terms of electron dose, but assumes that:

- For each electron, we encode one bit of information in *one* detector bin (1), and for the rest, we get no reading (0).
- We have a way to control the phase of the incoming electron wave precisely.
- We have a way to set up an experiment to find out if the modulo of the phase shift of the sample with respect to the local incoming phase of the wave is higher or lower than some value.

Another approach involves arranging multiple *passes* of the electron wave through the sample, as proposed in the framework of the quantum microscope [315–318]. Further improvements are anticipated with the use of a beam splitter and *squeezed* or entangled electron states [319], where the wavefunction's distribution variation is only one quantum

number. This minimization of variation between electron states sets the theoretical limit down to Heisenberg uncertainty, resulting in higher contrast, as the redistribution of the weighted wavefunction (i.e., phase-shifted) becomes more pronounced. However, the practical implementation of this approach currently appears to be highly challenging, as any thermal noise and other physical effects could break most of the assumptions needed.

5.7.3 Technological difficulties to realize this

In this chapter, we have looked at the fundamental counting noise limits and have assumed that we can create an ideal phase plate acting on the phase of the illuminating wave and an ideal but correctly normalized version of the ZPC that acts on the exit wave in the BFP. Several technological obstacles have to be overcome to realize these ultimate predictions for the ZPC case:

- The ideal Airy disc-like Zernike phase profile is difficult to realize.
- The ideal Zernike phase shift may differ from $\pi/2$ (see Bellegia [320]).
- The ZPP profile should adapt in width to the illumination size to obtain the best performance while avoiding loss of low frequencies.

Also, for the RPI, several obstacles will hinder a straightforward implementation:

• As stated in previous chapters, a programmable phase plate has considerable limitations regarding the fill factor, meaning that we also imprint amplitude modulation into the probe. However, this may be beneficial in some cases [278, 280]. This could be overcome by scanning the amplitude and phase-modulated probe in focused-probe-ptychography-style to illuminate all the sample with some overlap between the probe positions.

Phase plate charging problems, gradual phase drift, and contamination are potential issues in both scenarios.

5.7.4 A note on re-normalisation

In this chapter, we have examined a sample as a collection of random phases without making any assumptions about the relationship between pixels or the probability of certain patterns occurring. In reality, the set of actual images is smaller than the total number of potential random phase formations. In other words, there is some underlying regularity in the sample. If we correctly describe this regularity, we can significantly gain in terms of signal-to-noise as this constitutes prior knowledge about the sample [275,321–323]. However, we need to be careful and compare similar situations. For example, if we use regularization in an RPI setup, we should use the same assumptions in the case of ZPC. Failing to do so will inevitably lead to biased results, as was the case in compressed sensing [324–326], which also relies on regularization arguments.

This makes it impossible to compare to a situation where normal sampling is applied unless the regularization prior is included [327]. For this reason, we will not discuss regularization here. However, significant gains can be achieved if such prior knowledge is available and valid [275].

5.8 Conclusion

We have demonstrated that there is a clear benefit in terms of dose-efficiency in recording multiple diffraction patterns over the more conventional ZPC imaging. We stress here that we have shown just one possible way of improving the dose efficiency of ZPC imaging without making claims on related ptychographic or other diffraction-based setups. Nevertheless, breaking this limit for one case demonstrates that ZPC is not the ultimate limit, and this should invite further research. Note also that we have assumed the weak phase object approximation throughout, which is known to be a very limiting assumption in practice. We found the benefit in terms of dose efficiency to be a factor of 5, which would allow a very significant shifting of the beam damage boundaries that are hindering progress in, e.g., life sciences, but also in many materials science areas such as battery materials, polymer science, zeolites, perovskites, metal-organic frameworks and many more.

This improvement factor is mainly attributed to a subtle normalization issue that occurs in ZPC imaging. This issue makes ZPC less dose-efficient, as it seems to be the case if we make a fair comparison where the sample is illuminated with exactly the same dose over exactly the same area of illumination. This chapter avoids discussing actual implementation details, and it might well be possible to improve this benefit further if, i.e., the illumination can be updated to take into account information from the partial experiment that was already performed. Whether the gain from the diffraction-based recordings proposed here can also be obtained in practice remains to be seen, as many practical details will influence the actual dose-efficiency. Nevertheless, there has been much promising progress in ptychography over the last few years, and it relies on diffraction-based detection, albeit with a different illumination scheme than the RPI suggested here.

One possible advantage of detecting in the diffraction plane while adjusting the phase of the probe is the potential for a simpler, smaller, and more cost-effective electron microscope specifically designed for life science imaging. In this scenario, the camera could have significantly fewer pixels, and the projector system could be removed entirely (along with the image corrector) as long as some form of scanning system or phase plate can quickly alter the illumination. This discovery shows promise for affordable tabletop instruments that could expand the information we can gather from beamsensitive nanoscale objects.

CHAPTER 5. RETRIEVAL OF PHASE INFORMATION FROM LOW-DOSE ELECTRON MICROSCOPY EXPERIMENTS: ARE WE AT THE LIMIT YET?

Chapter

Electron Wavefront Shaping for the End-User

Contents	
6.1	State of the Art Electrostatic Phase Plate for Electrons: AdaptEM
	WaveCrafter

Throughout this work, we have explored the potential applications of an EPP for electrons, with a particular focus on its comprehensive characterization in chapter 4. However, we have not yet delved into the practical operation of the EPP. To address this, we dedicate this brief chapter to provide the reader with insights into the *hands-on* operation of an EPP. Additionally, we will discuss the various designs offered by AdaptEM's Wave-Crafter [186], one of which was at the core of the experiments presented in chapter 4.

6.1 State of the Art Electrostatic Phase Plate for Electrons: AdaptEM WaveCrafter

The device showcased in chapter 4 consists of an array of 48 programmable Einzel lenses, contained within a circular area of approximately 50 μ m. However, the technology is designed to support different geometries, offering a significant advantage in terms of upgradeability. Furthermore, as discussed in chapter 3, the system can be customized for specific applications based on the required illumination parameters within the current technological limitations.

Different commercially available EPP designs were tested. These include the segmented device with 48 pixels, a Cartesian geometry design with a 6×6 grid of circular holes, and a simplified segmented design featuring 12 triangular segments. These configurations are presented in fig. 6.1, along with focused and defocused images of the probes they produce. Additionally, an overview of the main parameters for each geometry is provided in table 6.1.

Design	# of Elements	Fill Factor	Radial Sampling	Azimuthal Sampling
Segmented 48	48	≈30%	++	++
Cartesian 36	36	≈36%	+	-
Segmented 12	12	≈60%	_	++

Table 6.1: Comparison of EPP Designs. The last two columns refer to the phase plate capabilities to apply a phase profile along the azimuthal and radial coordinates of the condenser aperture, qualitatively ranging from very efficient (++) to unefficient (-).

As the technology is designed to operate with any geometry, the designs depicted in fig. 6.1 can be driven with the same controller setup and software, facilitating upgrades or replacements with relative ease. A screenshot of this user interface software is included in fig. 6.2. Additionally, regardless of the microscope type or manufacturer, the device operation remains the same once installed.

This brief chapter highlights that once the device is installed in the microscope, it can be operated intuitively, as it does not interact directly with its controls. Moreover, the software allows for incorporating routines that can, e.g., directly receive feedback from the detector or communicate with a scan engine. This feature offers significant versatility with relative ease, as demonstrated by the adaptive routines shown earlier in chapter 4. Notably, the development efforts invested in the controller provide a significant advantage for other users' adoption and testing, as the system can be efficiently designed and optimized for various applications in both hardware and software.

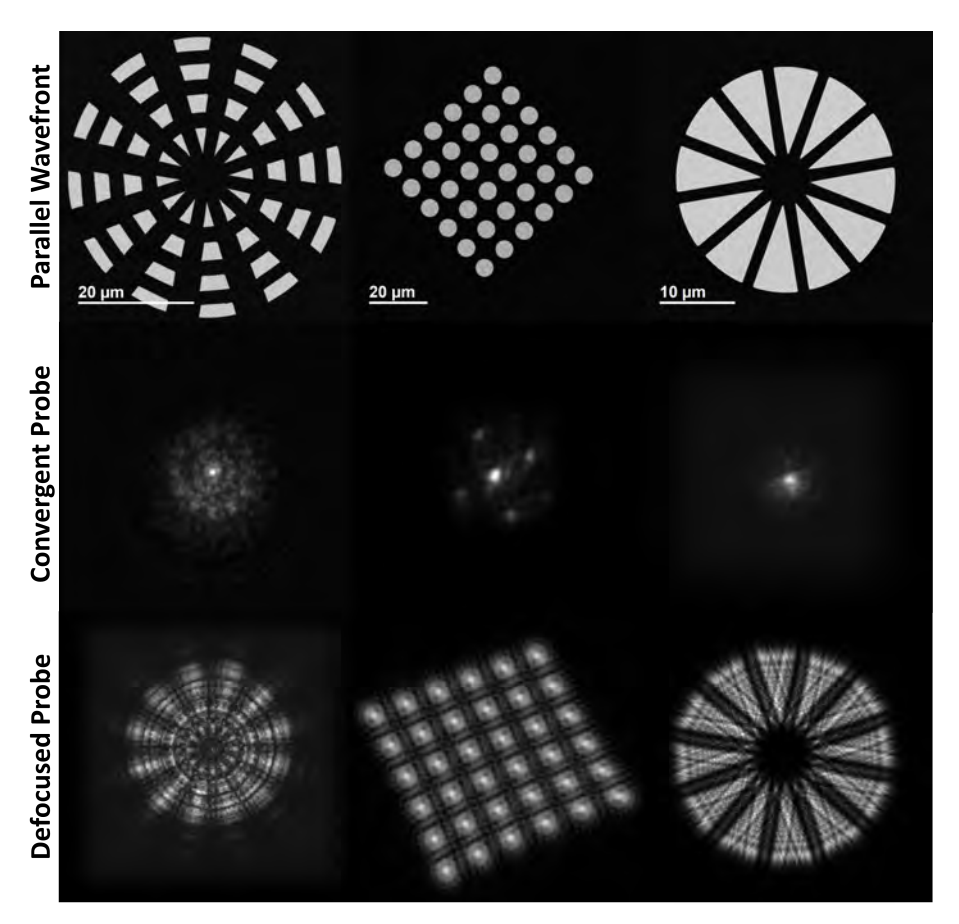


Figure 6.1: Commercially available EPP designs by AdaptEM [186]. The left column features the Segmented 48 design used to obtain the experimental results presented in chapter 4. The middle column displays the Cartesian 36 design, while the right column presents the Segmented 12 design. The electron wavefront resulting from each design, without any voltage applied to its phase pixels, is illustrated with three configurations: the top row shows the plane wave (CTEM), the middle row features the convergent probe (STEM), and the bottom row displays the defocused convergent probe (Defocused STEM).

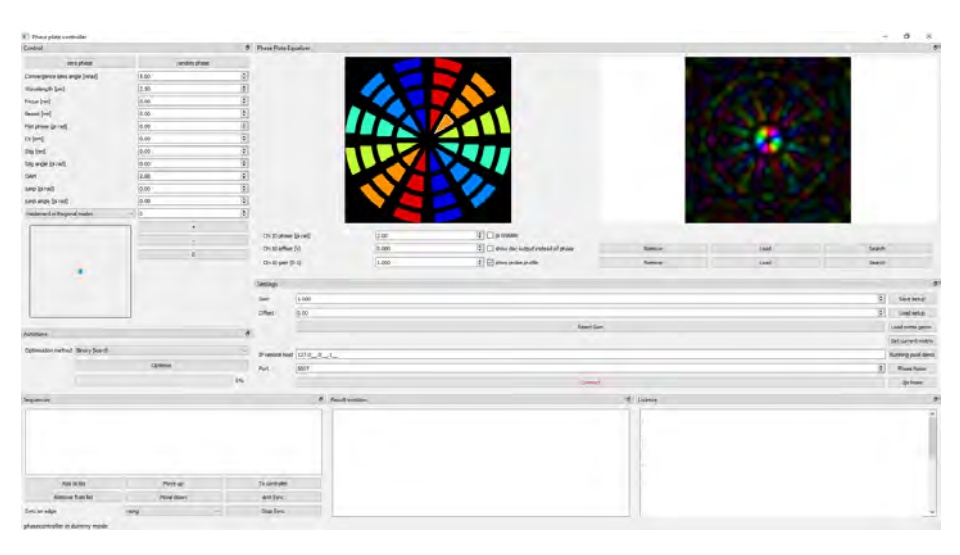


Figure 6.2: Snapshot of the Phase Plate controller software adapted for the Segmented 48 design. The Control panel on the left shows different presets for common probe geometries. On the top right, a display with the current geometry of the phase plate (condenser plane) and the probe (sample plane) is shown to serve as a reference to the user. Additional settings include each phase pixel's gain and offset values and dynamic routines that enable automatic correction.

Chapter

General Discussion and Conclusions

Contents		
7.1	Summary and Overview of this Work	96
7.2	Outlook and Future Prospects for Electron Wavefront Shaping	97
7.3	Conclusion	99

7.1 Summary and Overview of this Work

This thesis explores the potential of adaptive wavefront shaping in electron microscopy. The first chapter focuses on the *construction* of the instrument. Our aim in this chapter was to investigate the possibilities and limitations that may arise during the routine operation of a TEM, which then serves as the main framework for the rest of the work. Additionally, we discuss electron optics from a particle perspective, which helps us understand the fundamental principles of electron lenses and other active elements.

In Chapter Two, we delve deeper into the concepts of electron optics by exploring the potential of generalized wavefront shaping. We provide examples demonstrating how this approach has revolutionized various research fields. Next, we examine electron wavefront manipulation from the quantum mechanical perspective of matter waves. We now describe the propagation of electron waves through the Schrödinger equation and link its potential term to Young's double-slit experiment and the Aharonov-Bohm effect. These foundational concepts lead us to an understanding of the Einzel lens, which serves as a fundamental building block for our wavefront shaping strategy. Finally, we introduce the multi-element EPP for electrons, which will be the starting point for further exploration of the concept in the subsequent chapters.

After establishing the framework and discussing the benefits of electron wavefront shaping in electron microscopy, we proceeded with the main body of this work. There, we focus on the concept of multi-element EPPs, introduced by Verbeeck et al. [144], examining their design and functionality and the challenges that this technology may help overcome in the future.

To analyze EPP, we first assessed their capability to correct spherical aberration in the TEM. The framework outlined in chapter 3 guides the design for current and future EPPs, with spherical aberration serving as the primary example due to its significant impact on resolution, as highlighted early on by Scherzer [28]. This is particularly relevant for instruments without an aberration corrector, where the proposed EPP may, in the future, be a viable alternative. Generally, we could list the main findings from this design exercise:

- An EPP with zeroth-order order elements can potentially correct spherical aberration and enhance an uncorrected TEM.
- The main improvement for aberration correction involves incorporating a first-order phase profile, necessitating two electrodes for each phase segment. Although this increases the complexity due to the higher number of connections needed for each segment, it is a worthwhile upgrade, as this enhancement can significantly reduce the number of segments required to achieve sub-Å STEM probes.

After reviewing notions fundamental to an EPP's design, we tested its practical capabilities in a TEM. For this, we utilized AdaptEM's Segmented 48 device. Our primary objective was to characterize the phase and responsiveness of each segment within the device. We employed a Gerchberg-Saxton algorithm on several intensity recordings and obtained a phase sensitivity of 0.075 rad/mV at 300 kV, with a phase resolution of approximately $3\times10^{-3}~\pi$.

Furthermore, to demonstrate the device's wavefront shaping capabilities, we recorded a series of probes forming part of a Hadamard basis set and some well-known Hermite-Gaussian and Laguerre-Gaussian profiles. Furthermore, we realized an experimental setup where the device was set to enhance a HAADF-STEM image automatically. While not reaching any remarkable feat in terms of resolution, we achieved unprecedented automated correction while utilizing a phase plate for electrons. Notably, despite lacking a top ground and having a limited fill factor, the device was still fully capable of generating complex probe shapes in a repeatable manner. It is reasonable to expect that with further refinements in the manufacturing process and the adoption of more advanced techniques, the efficiency of these devices will significantly improve.

On the controller side, the speed at which we can manipulate the phase profile of the electron wavefront is primarily constrained by the electronics, particularly the settling time for the DAC. Addressing this issue (i.e., by pre-loading specific phase configurations into the controller's memory) could achieve much higher update speeds. This improvement presents a promising opportunity for adaptive TEM experiments, especially when coupled with emerging fast detector technology [328–332].

In chapter 5, we took a more theoretical approach to discussing electron wavefront shaping as a concept extending beyond any limitation of an EPP set. From an information perspective, we explored whether there is any possibility of surpassing the established limits set by the gold standard for phase imaging, which is Zernike phase contrast.

Interestingly, a small normalization error can lead to inaccurate conclusions regarding dose-efficient measurements. Minor misunderstandings can result in overly optimistic assumptions when we operate near the information limit. Specifically, the low-frequency scattering of electrons at the back focal plane by the finite-sized Zernike phase plate and the inherent creation of a reference beam creates a situation where the improper normalization of electrons that exit the boundaries of the object array is not considered in the overall assessment of dose efficiency. This oversight can lead to incorrect conclusions about the measurement's precision. The potential five-fold improvement in dose efficiency provided by a set of known, random phase-structured waves, compared to a Zernike phase contrast method, reignites the discussion around this topic. This positions electron wavefront shaping as a promising approach for enhancing diffraction-based measurements and improving low-dose experiments overall.

7.2 Outlook and Future Prospects for Electron Wavefront Shaping

The findings summarized in the previous section highlight the significant potential of a generalized electron wavefront-shaping device to transform electron microscopy. However, the widespread adoption of this technology is still hindered by several engineering challenges (i.e., contamination, fill factor, cross-talk, degradation) that require advanced technological and manufacturing solutions. While substantial progress has been made, as shown by the state-of-the-art multi-element EPP discussed in chapter 4, the technology is not yet capable of providing a comprehensive solution to the various challenges faced in electron microscopy.

While there are engineering challenges, physics offers a more optimistic outlook. These devices could significantly improve current technology regarding aberration correction, yielding a two-fold advantage over traditional aberration correctors. First, with a sufficient fill factor (i.e., above 70%), even a small number of segments can provide adequate correction for most applications. Such a device could reduce the cost and complexity of instruments needed for tasks like atomic resolution imaging. Second, the aberration correction provided by these devices would be more reliable regarding response, power consumption, and stability. Correcting aberrations with multipole correctors requires meticulous alignment and careful tuning of boundary conditions. In contrast, using an electrostatic phase plate only necessitates updating the voltage in the phase segments accordingly, with near-live update speeds. In summary, from the standpoint of aberration correction, such a device could *revive* previously limited instruments in line with modern standards or enable entirely new, cost-effective designs.

Additionally, improving dose efficiency can significantly decrease the electron dose needed to obtain information from dose-sensitive samples reliably. As electron microscopy becomes a crucial characterization method in biology and interest in the properties of 2D materials increases, adopting wavefront modulation strategies could lead to significant breakthroughs in both fields. Furthermore, structured illumination has recently emerged as a promising solution for many phase retrieval problems, as noted in several studies [278–281]. This indicates a growing trend towards using wavefront modulation to enhance convergence and efficiency in these experiments.

While not directly addressed in this work, various emerging applications investigate the potential of electron wavefront shaping. These include phenomena such as PSEELS [107, 147, 148, 333, 334], enhancements in X-ray radiation [66, 335], and even the manipulation of Rydberg atoms using free electrons [336], among others. This trend demonstrates how advancements in electron wavefront shaping technologies stimulate theoretical and practical developments, promoting further technological progress. This development *loop* is also evident throughout this work, tracing back to the initial demonstration of a multi-element EPP [144], which eventually led to the development of AdaptEM's WaveCrafter, which is commercially available for any microscopy user.

If we take a survey beyond electron microscopy or focused ion beam, advancements in the development of electron wavefront shaping technology have significant potential when integrated with Complementary Metal-Oxide-Semiconductor (CMOS) technology. For instance, dynamic random-access memory (DRAM) devices consist of millions of fast-switching gates made from capacitors and transistors [337]. While the connection may not be immediately apparent, the proposed design for a first-order phase segment functions similarly to a capacitor, as explained in chapter 3. It accumulates charge, creating a linear electric field across its surface, which translates into the potential field required to imprint localized phase-shift onto the electron beam. Moreover, controlling these miniaturized components is relatively straightforward because a grid-like voltage source can individually address each circuit through x and y lines, reducing the complexity of the controller's hardware. Therefore, despite any initial skepticism, DRAM technology presents a promising platform for developing future generations of programmable phase plates for electrons, given that it meets the necessary criteria for electron transparency (as CMOS technology is not designed to create an array of holes) and other specific requirements dictated by the intended instrumentation.

7.3 Conclusion

The central question we have been exploring throughout this work is whether electron wavefront shaping can enhance electron microscopy. The short answer to this question is *yes*. However, achieving this with sufficient versatility is quite challenging, as stressed by several realizations [144,179,183,317,338].

Advancing into a new field requires considerable effort, and the technology necessary for implementing electron wavefront shaping is developing alongside theoretical studies demonstrating its potential applications. Notably, many of the applications mentioned, especially low-dose imaging for biological specimens, suggest that the future of electron microscopy will involve greater flexibility in electron wavefront modulation and the use of adaptive optical devices.

In conclusion, approaching a problem from a different angle is often beneficial. For example, the assumption that only the smallest probes can achieve atomic resolution in STEM can lead us into an engineering *rabbit hole*, where it seems that only the most expensive tools are capable of making groundbreaking discoveries. Thankfully, this misconception is demonstrated by techniques such as electron ptychography [88, 222], described in section 1.2.3. The findings presented in this work could serve as a foundation for testing potential applications and a source of inspiration for further advancements, broadening the instrument's capabilities.

CHAPTER 7. GENERAL DISCUSSION AND CONCLUSIONS

List of Figures

1.1	The development of microscopes throughout history has been quite remarkable. The Nimrud lens (a), one of the oldest dating evidence of the use of artifacts to magnify objects, was found in modern-day Iraq, and it is dated to 750 B.C. (adapted from https://en.wikipedia.org/wiki/File:Nimrud_lens_British_Museum.jpg by Geni). In the 17 th century, Robert Hooke published some remarkable work on biology in his book "Micrographia," where he used a microscope manufactured by Christopher White, shown in (b), to observe biological specimens [5]. Modern optical microscopes, like the one shown in (c) by the Zeiss company (adapted from https://www.zeiss.com/microscopy/en/products/light-microscopes/super-resolution-microscopes/elyra-7.html), boast advanced optical and mechanical elements and computational integration for image processing. The first-ever prototype for an electron microscope was built by Ernst Ruska and is shown in (d) (adapted from https://commons.wikimedia.org/wiki/File:Ernst_Ruska_Electron_MicroscopeDeutsches_MuseumMunich-edit.jpg by J Brew). In contrast, one of EMAT's modern TEM by Thermo Fisher Scientific is shown in (e).	4
1.2	Diagram showing the main components of Thermionic (a) and Field Emission (b) electron sources. The simplified circuit in (a) (similar to (b), but not drawn for convenience) and (c) indicates the basic principle for extraction and acceleration of the electrons for each case (adapted from [8])	5
1.3	Typical ray representation of a convex lens, the light emitted from an object of width a_0 is bent and then replicated at a distance d_i , producing an image of size a_i . The bent rays form a crossover point on both foci on either side of the lens at a focal distance f_i .	7

1.4	The diagram illustrates the cross-section of an electron lens in 2D (left). When electrons enter the lens from a point in the focal plane (FP), they are deflected by the magnetic field created by the current passing through the coils. The current flowing into the page is represented by \otimes , while the current flowing out of the page is represented by \odot . This current magnetizes the soft-iron pole pieces, generating a toroidal magnetic field around the coils. The distance to the back focal plane (BFP) can be adjusted by increasing (f_a) or decreasing (f_b) the current flowing through the coils. The notation is similar to that in fig. 1.3 to emphasize the parallels between electron and optical lenses. The diagram is extended (right) to represent the electron velocity upon entering the lens $\mathbf{v} = (v_r, 0, v_z)$, the magnetic field within the lens $\mathbf{B} = (B_r, 0, B_z)$, and the azimuthal (F_ϕ) and radial (F_r) forces resulting from the interaction. (adapted from [8])	9
1.5	Ray diagram representation of different types of electrostatic lenses: convergent (a), divergent (b), two-electrode (c), and three-electrode (Einzel lens) (d). The figure dimensions are exaggerated to illustrate the effect of the lens	11
1.6	Simulated phase aberrations constructed from eq. (1.15). The coefficients used for the simulations are $C1 = A1 = 20nm$, $B2 = A2 = 2\mu m$, and $C3 = S3 = A3 = 75\mu m$. All phase profiles are over a semi-convergence angle $\alpha = 20 \ mrad$. The color bar on the right represents the phase, while the amplitude is equal to one throughout the array	12
1.7	The diagram in (a) depicts the magnetic field lines (in black) in a quadrupolar lens. As the electrons move into the page with a velocity represented by \mathbf{v} , they experience a radial Lorentz force $F_{\hat{r}}$. This force can be adjusted by regulating the current in each solenoid (adapted from http://commons.wikimedia.org/w/index.php?curid=11117039 by Geek3). In (b), there is an image of a hexapole corrector used in a TEM (source http://commons.wikimedia.org/w/index.php?curid=16445968 by Materialscientist). Finally, (c) shows a simplified ray diagram of a double-hexapole aberration corrector, including the transfer lenses	14
1.8	Diagram showing the main optical elements of a FEI Titan ¹ . The diagram labels each component and groups them by modules, whose names are shown with braces on the right. Most of the experimental results contained in this thesis were obtained with this microscope	17
1.9	The diagram below illustrates TEM's most common operation modes. In addition to adjusting the optical elements above the sample, a projection system (not shown) is typically employed to magnify the image and switch between diffraction and imaging modes. The most frequently used mode for STEM is HAADF, where an intensity signal I_{β} is captured for each probe position (x, y) on the sample plane. More recently, there has been growing interest in 4D-STEM applications, where a pixelated detector in reciprocal space acquires spatially resolved intensity (I_{k_x}, I_{k_y}) . These applications are gaining attention due to their dose efficiency and ability to withstand some optical imperfections in the microscope	20

2.1	Young's double slit experiment simulation: as the number of photon counts increases on the far-field detector, the interference pattern emerges, suggesting the wave-like behavior of light	25
2.2	Schematics of experiments proposed by Aharonov and Bohm demonstrating interference with a magnetic vector potential (a) and electric scalar potential (b). (a) elements A, B, and C split the electron beam into two paths and interfere at F after being influenced by the vector potential produced around a solenoid. (b) devices A, B, C, D, and E divert and guide wave packets W1 and W2 through cylindrical metal tubes M1 and M2 inside which we apply a scalar potential, resulting in interference at F. Schematics are adapted from Fig. 1 and 2 of Ref. [125]	27
2.3	Young's double-slit experiment (top) contrasted with a setup where one of the slits is subjected to an electric scalar potential (bottom), resulting in a variation of the interference pattern.	28
2.4	Diagram of an electrostatic phase shifting element, as proposed by Börsch, adapted from [126]. Implementations of a Zernike Phase Plate are shown using a thin film (a) and a small Faraday cage (b). A different setup of (b) is shown in (c), where the central and surrounding beams travel inside the cage. The miniaturized realization of Börsch's Einzel lens concept, as demonstrated by Matsumoto and Tonomura, adapted from [127] (d), with a more detailed view of the layers in (e)	29
2.5	Demonstration of a 2x2 Electrostatic Phase Plate for Electrons. The diagram in (a) illustrates the operational principle of the device, where different voltages are applied to each of the individual conductive cylinders. This configuration creates a 4-slit aperture Aharonov-Bohm device. Part (b) presents an SEM image of the device mounted on the Dens Solutions Wildfire in-situ heating chip holder. Figure adapted from [144]	30
3.1	Sketch of a conventional round aperture versus an array of phase-shifting elements occupying a similar area as in the round aperture case. Parameters such as fill factor (ζ) and angular range ($\Delta\theta$) are indicated along with the relation between maximum aperture (θ_{max}) and radius ($r(m)$). We show where the interconnections and supports are allocated in the aperture, thus reducing the fill factor.	36
3.2	Representation of the effect of the Fill Factor (ζ) on probe intensity. Due to the amplitude modulation, the resulting probe intensity, represented as $ \Psi_{pp} ^2$, will have a portion of its intensity in the central lobe, with maximum intensity (I_{max}) proportional to ζ . The contrast of the probe arrays shown on the right has been adjusted arbitrarily to enhance the visibility of the much lower-intensity tails. Additionally, a cumulative integrated intensity is shown below. The shaded areas roughly indicate the <i>wanted</i> sharp probe section (green) and the <i>unwanted</i> longer-range tails (red), with a diffraction-limited probe shown in black for comparison	39

3.3	Sketch of zeroth- and first-order phase element as the main building blocks of an array of programmable phase-shifting segments	41
3.4	Minimum $\Delta\theta$ needed to correct for C_s as a percentage of the total aperture for different phase errors ϵ (left axis, log scale). These can be translated to minimum segment feature sizes when assuming a total aperture diameter of 70 μ m (right axis). The shaded regions (green, violet, red) show the approximated region where photolithography, extreme ultraviolet (EUV) lithography, and electron beam lithography (EBL) would be required to make such features [161]	42
3.5	Simulated performance of different apertures at 300 keV. (a) The aberrations over a corrected round aperture at 21 mrad with $C_s=1\mu m$ and Scherzer's defocus. The aberrations for (b,c,d) are 1.2 mm C_s with Scherzer's defocus as well. (b) A zeroth-order phase plate with 19 segments and $\approx 77\%$ fill factor at 15 mrad opening angle, (c) and (d) hybrid correction phase plates with four central zeroth-order segments followed by eight first-order segments and $\approx 89\%$ fill factor at 21 mrad in the case of (c), and one central zeroth-order hole followed by eight first-order segments and $\approx 92\%$ fill factor at 18 mrad for (d). (e-h) The simulated probe intensities below the corresponding phase plate responsible for them; the simulation box is $6x6\text{Å}$. (i) A radially integrated profile for each of the abovementioned figures. The proposed alternatives improve the spot size compared with the aberrated instrument. However, it is important to mention that the feature size of the smallest segment in (b) is $\approx 270nm$, whereas the hybrid plates' segments are $1.5\mu m$ wide. The color wheel inset in (a) shows the scale used to represent both phase (hue) and amplitude (intensity)	43
3.6	Simulated probe size d_{50} assuming 300 keV, $C_s = 1.2$ mm, and Scherzer defocus for the phase plates and non-corrected aperture. The black line shows the 1Å limit. All proposed phase plate designs are capable of a probe size below this limit (blue, yellow, green lines). However, they are still outperformed by a multipole corrector (red line)	44
3.7	Current density J_{50} for the different phase plate designs at different θ_{max} assuming a total incoming current up to 50 pA. All proposed designs significantly improve compared with a non-corrected aperture; the red (dotted) line shows the corrected instrument's performance	45
3.8	d_{50} value for different ζ using a zeroth-order phase plate. We kept the same design as in fig. 3.5 b. for the segments, only increasing the width of the lines going outwards in the radial direction and thus keeping the sampling on θ the same. We can observe how the d_{50} is heavily affected by ζ , making it difficult for a zeroth-order phase plate to obtain a sub-Å probe for $\zeta < 0.70$	46

3.9	Average probe size a_{50} including different levels of phase noise ϵ for the zeroth-order ring phase plate. The shaded area represents the 2σ variation for 10 random realizations of the phase noise, and the black line shows the performance of the phase plate without any phase noise (lower limit). The plot shows that sub-Å performance is possible for all but the highest noise level simulated here.	47
4.1	Sketch of the working principle of the phase plate (a). Only 2 pixels are drawn. 3D render of the setup (b) and the main components, including the phase plate (c), the voltage sources (d), and the phase controller computer (e). A reference bar of 30 μ m is presented in (c)	54
4.2	Phase sensitivity matrix and the corresponding root mean squared error of the linear fitting	56
4.3	Realization of various electron quantum states. The three rows of figures, from top to bottom, are the phase configurations set on the phase plate, the simulated probe shapes, and the resulting experimental probe images, respectively. Note the excellent agreement between expected and obtained results showing successful arbitrary wavefront shaping	57
4.4	Defocused probes formed by defocusing the microscope lenses (top row) and the phase plate (bottom row) at 300 kV acceleration voltage and an opening angle of 1 mrad. Note the close similarity of both, showing that the phase plate can mimic the action of a round lens to up to 200 nm defocus	58
4.5	Simulated ADF images of various probe shapes (see the insets) and their Fourier transforms. The line profiles (orange lines) are taken at the position of the white dashed line in each image. Note that the intensity profile in the round aperture image is halved for better presentation and that the black line in the difference image indicates zero, while in other images, zero is set at the bottom of the figures	60
4.6	Schematic of the adaptive probe correction with phase plate. The flowchart displayed in (a) demonstrates the fundamental steps of the algorithm being employed. The HAADF images before (b) and after (c) the correction are shown below.	61
4.7	Simulated ptychographic phase reconstruction from recorded diffraction patterns with various illuminating beams. (a) The ground truth phase image of the object. (b-d) Reconstruction results from illuminating beams formed by a conventional round aperture, flat phase plate, and phase plate with random phase configuration, respectively. The dark region indicates the opaque part of the aperture. Note the significant improvement in phase reconstruction quality when the incoming beam is phase randomized. As the object is only illuminated once, reconstruction is only possible in those areas where the amplitude is not zero	63

5.1	Sketch of the setup. The aim is to measure the N phases of the unknown object by illuminating it with a coherent electron wave and detecting the arrival of electrons with an ideal detector consisting of M independent pixels. The left-side setup shows the configuration with an ideal ZPP, while the right-side setup describes the detection in the diffraction plane with a programmable phase input wave. We will compare the performance of both setups in terms of phase error on the estimate as a function of the amount of electrons we have available in the experiment
5.2	Sketch of a numerical 2D implementation of ZPC imaging that avoids aliasing effects that would lead to errors in estimating the quantum efficiency of the ZPC imaging process
5.3	Example of a correctly sampled ZPC image of a random phase object of 64×64 zero-padded to 128×128 with $N_e = 5 \times 10^5$. The central 64×64 area contains the actual phase-related image and $5/8$ of the total dose with which the object was illuminated. The other $3/8$ lands outside the central area and does not contribute to the desired information
5.4	Numerical simulation of the average RMS phase error as a function of total electron dose. The object is considered a random phase object with four unknown phase values and a limited phase range of $\pm \pi/10$ to stay within the linear approximation of the ZPC formula. The simulation is repeated 100 times for each electron budget with a different random object. Random phase illumination is done with 16 random illumination patterns that stay the same throughout the simulation set. Note how ZPC and RPI's results closely follow the predicted statistical error and show a similar noise performance up to about $N_e = 10^4$, where systematic errors due to the linearization of the ZPC formula start to show. Note also how ML RPI and GS RPI perform remarkably similarly, giving confidence in the GS approach for larger systems.
5.5	Numerical simulation of a 4×4 phase object encoding 100 different realizations of random phase noise with a range of $\pm\pi/10$ for each electron budget. The electron budget is divided over 16 random phase illumination patterns. Note the significant difference with ZPC due to the normalization correction and the close relation between the ML RPI and the much faster GS RPI
5.6	RMS phase error for a single 64×64 random phase object with $\pi/10$ phase range, illuminated with $N_{RPI} = 2, 16, 64$. We note that ZPC and GS closely follow their predicted error behavior as a function of the total dose. We note a remarkable trend at low doses where the phase error shows a plateau depending on N_{RPI} , which is a consequence of phase wrapping in the individual N_{RPI} realizations
5.7	Comparison of ZPC and GS RPI phase retrieval as a function of dose on a more realistic 2D object. At high doses, both methods retrieve the object effectively. The top figures marked with a \star do not adhere to the color bar scaling to aid visualization.

6.1	Commercially available EPP designs by AdaptEM [186]. The left column	
	features the Segmented 48 design used to obtain the experimental results	
	presented in chapter 4. The middle column displays the Cartesian 36	
	design, while the right column presents the Segmented 12 design. The	
	electron wavefront resulting from each design, without any voltage ap-	
	plied to its phase pixels, is illustrated with three configurations: the top	
	row shows the plane wave (CTEM), the middle row features the conver-	
	gent probe (STEM), and the bottom row displays the defocused convergent	
	probe (Defocused STEM).	93
6.2	Snapshot of the Phase Plate controller software adapted for the Segmented	
	48 design. The Control panel on the left shows different presets for	
	common probe geometries. On the top right, a display with the current	
	geometry of the phase plate (condenser plane) and the probe (sample	
	plane) is shown to serve as a reference to the user. Additional settings	
	include each phase pixel's gain and offset values and dynamic routines	
	that enable automatic correction	94

List of Tables

1.1	Operational and optical parameters of some of the most commonly used electron sources [9,10]	6
6.1	Comparison of EPP Designs. The last two columns refer to the phase plate capabilities to apply a phase profile along the azimuthal and radial coordinates of the condenser aperture, qualitatively ranging from very efficient (++) to unefficient (-)	92

LIST OF TABLES

List of Abbreviations

TEM Transmission Electron Microscope

FEG Field Emission Gun

EELS Electron Energy Loss Spectroscopy
EDX Energy Dispersive X-ray Spectroscopy

OP Object Plane
BFP Back Focal Plane
IP Image Plane
FP Focal Plane

PSF Point Spread Function

C_s Spherical Aberration

SBR Signal-to-Background Ratio

GS Gerchberg-Saxton

DAC Digital to Analog ConverterMTF Modulation Transfer FunctionDQE Detective Quantum Efficiency

CTEM Conventional Transmission Electron Microscopy
STEM Scanning Transmission Electron Microscopy
HRTEM High-Resolution Transmission Electron Microscopy

CTF Contrast Transfer Function HAADF High-Angle Annular Dark Field

ABF Annular Bright Field

CBED Convergent Beam Electron Diffraction

4D-STEM Four Dimensional STEM
SLM Spatial Light Modulator
EPP Electrostatic Phase Plate
PSEELS Phase-Shaped EELS

FWHM Full Width at Half Maximum

EUV Extreme Ultra Violet

EBL Electron Beam Lithography

GS Gerchberg-Saxton

STED Stimulated Emission-Depletion
SLAM Switching Laser Mode Microscopy

CRLB Cramér-Rao Lower Bound

FI Fisher Information
ZPC Zernike Phase Contrast
ZPP Zernike Phase Plate

WPOA Weak Phase Object Approximation

RPI Random Phase Illumination

MLMaximum Likelihood

MLE Maximum Likelihood Estimator

One Dimensional 1D 2D Two Dimensional Root Mean Squared RMS

Complementary Metal-Oxide-Semiconductor Dynamic Random-Access memory **CMOS**

DRAM

List of Author's Contributions

7.4 Peer Reviewed Articles

- Vega Ibáñez, F., Béché, A., & Verbeeck, J. (2023). Can a programmable phase plate serve as an aberration corrector in the transmission electron microscope (TEM)? Microscopy and Microanalysis, 29(1), 341-351.
- Yu, C. P., **Vega Ibáñez, F.**, Béché, A., & Verbeeck, J. (2023). Quantum wavefront shaping with a 48-element programmable phase plate for electrons. SciPost Physics, 15(6), 223.
- **Vega Ibáñez, F.**, & Verbeeck, J. (2024). Retrieval of phase information from low-dose electron microscopy experiments: are we at the limit yet? M&M,
- Overview of Electron Wavefront Shaping, in preparation

7.5 Conference Talks and Poster Presentations

- **Vega Ibáñez, F.**, Béché, A., & Verbeeck, J. (2021, October 5). *Prospects for using a pro-grammable phase plate to correct for lens aberrations in TEM* [Conference presentation]. eBEAM Colloquium, Online.
- **Vega Ibáñez, F.**, Béché, A., & Verbeeck, J. (2022, May 8–12). *Can a Programmable Phase Plate serve as an Aberration Corrector in the TEM?* [Poster presentation]. PICO 2022 Conference, Kasteel Vaalsbroek, Vaals, Netherlands.
- **Vega Ibáñez, F.**, Béché, A., & Verbeeck, J. (2023, February 26–March 2). *Can we enhance the depth of focus/depth resolution in STEM with an electrostatic phase plate?* [Conference presentation]. Microscopy Conference 2023, Darmstadt, Germany.
- **Vega Ibáñez, F.,** Yu, C.-P., Béché, A., & Verbeeck, J. (2023, October 11–13). *Quantum wavefront shaping with a 48-element programmable phase plate for electrons* [Conference presentation]. Electron Beam Spectroscopy for Nanophotonics (EBSN) 2023, Antwerp, Belgium.
- **Vega Ibáñez, F.**, Yu, C.-P., Béché, A., & Verbeeck, J. (2023, October 11–13). *Ultra- Fast Beam Shaping for Differential Imaging in HAADF-STEM* [Poster presentation]. Electron Beam Spectroscopy for Nanophotonics (EBSN) 2023, Antwerp, Belgium.
- **Vega Ibáñez, F.**, Yu, C.-P., Béché, A., & Verbeeck, J. (2024, April 21–25). *Electron Ptychography with an Electrostatic Phase Plate for Electrons* [Poster presentation]. PICO 2024 Conference, Kasteel Vaalsbroek, Vaals, Netherlands. **Best Poster Award.**

- **Vega Ibáñez, F.**, Yu, C.-P., Béché, A., & Verbeeck, J. (2024, August 25–30). *Wavefront Shaping for Phase Retrieval from low-dose experiments: are we at the limit yet?* [Conference presentation]. European Microscopy Conference (EMC) 2024, Copenhagen, Denmark.
- **Vega Ibáñez, F.**, Yu, C.-P., Béché, A., & Verbeeck, J. (2024, September 10). *Demonstration of Adaptive Wavefront Shaping with AdaptEM's WaveCrafter* [Conference presentation]. eBEAM Colloquium, Paris, France.

7.6 Repositories

• **Vega Ibáñez, F.** (2024). *PP_PhaseRetrieval_SciPost* [GitHub repository]. GitHub. https://github.com/FVegaIbanez/PP_PhaseRetrieval_SciPost

7.7 Non-peer reviewed contributions

• Vega Ibáñez, F., Béché, A., & Verbeeck, J. (2024, August 25). Wavefront Shaping the Future of Electron Microscopy. Electron Microscopy Society, 25th Anniversary.

Acknowledgements

Nearly five years ago, I had an interview with Jo, followed by meetings with Armand and Giulio. During a time of uncertainty, I encountered an opportunity to return to somewhat familiar territory (or so I thought) with an intriguing and ambitious offer for a PhD project. At that moment, it was hard to imagine when I would be sitting down to write the acknowledgments for this work, but here I am now.

Indeed, I have experienced different times, realities, and versions of myself, but throughout these changes, I have felt a significant amount of support from many people.

Mary, Bego, Fede, no hay palabras suficientes para expresar el apoyo invaluable que me han brindado desde mis años como estudiante en México y ahora en esta etapa en Europa.

Mary, tus cuidados han sido mi refugio en los momentos más desafiantes. Desde esas llamadas antes de dormir hasta nuestras conversaciones durante cenas viajando por Europa, siempre has estado presente. Admiro profundamente tu labor como madre, y este logro es, en gran medida, fruto de la educación que recibí en casa, donde siempre me motivaste a ser un hombre responsable y perseverante.

Bego, quizá no lo sepas del todo, pero tu orgullo y alegría al verme avanzar han sido un motor en los momentos más difíciles. Saber que cuento con una hermana que confía en mí me ha dado la fuerza para seguir adelante con determinación y entusiasmo.

Fede, desde los inicios de mi carrera, has sido un guía constante. Me ayudaste a mantener el enfoque en mi profesión y a encontrar calma y seguridad en mis decisiones. Gracias a ti, entendí que seguir este camino no solo me haría sentir realizado, sino también en paz conmigo mismo.

En conjunto, reconozco la suerte que he tenido en la vida por tener una familia tan maravillosa que me ha podido brindar apoyo constante a lo largo de mi vida, sin importar lo difícil que parezcan las cosas. Siempre son y serán mi Norte, los quiero mucho.

Jo, receiving guidance from such a brilliant and creative mind was a pleasure. It was sometimes challenging to keep up, but every short or long discussion opened my eyes to new perspectives and prompted me to return with answers or, perhaps, even more questions. Additionally, I thoroughly enjoyed the less scientific side of your mentorship. Though not as preachy as you might think, our philosophical conversations and talks about life outside of science, politics, or even pizza led to fun insights that I cherish as memorable moments from my PhD experience.

Armand, I am grateful for the work we shared and the opportunity to learn from you. Your positive attitude always shone through, no matter how late we were at Osiris or

how well things were going. As I don't speak French, I may have missed some of the words during the less successful results, but I truly value your teachings. Each session we had at the lab provided a valuable opportunity for me to ask questions and gain knowledge from you.

I would like to express my gratitude to my Doctoral committee members: Prof. Dr. Bart Partoens, Prof. Dr. Jan De Beenhouwer, Prof. Dr. Thomas Juffmann, and Prof. Dr. Nahid Talebi, for their thorough readings of this work and for providing valuable insights and suggestions for improvement.

Chu-Ping, the moment you inquired about the phase plate was one of the most significant moments of my PhD journey. You truly guided me through the EMAT process and were always open and helpful with both scientific and non-scientific questions I had. Furthermore, it was thanks to you that I realized I needed to build more confidence to complete my PhD, which encouraged me to be more myself around the office. I truly value our friendship, and I look forward to the random (or not-so-random) experiences we might share.

Another great thing I got to experience during my PhD (and hopefully the years to come) is the PICO band, making it the third time this group has been mentioned in the acknowledgment section of an EMAT thesis. The immediate connection I felt with this incredible group provided support during rainy days and challenging moments in Antwerp, often in a room where time seemed to pass unusually quickly. Furthermore, they helped me rediscover my passion for music, which may have contributed to my tendency to acquire too many instruments.

Anna, has sido la mejor compañera de piso que podría haber pedido, tanto en los momentos difíciles como en los más ligeros. Desde los pleitos con la vecina hasta nuestras discusiones políticas, pasando por tu infinita paciencia al aguantar mis *conciertos* de guitarra, a pesar de mi falta total de conocimiento del instrumento. Espero que sigamos compartiendo momentos de salseo con mi madre y disfrutando de muchos viajes y momentos juntos en el futuro.

Christoph, perhaps I can summarize everything as 10/10, but I will extend more. From Korsakov nights to running out of people to jam with, hanging out with you is always fun. You are the most annoying vegan I have had the pleasure of debating with, but always with some fun and joking between the lines. Keep up the cheerful motivation and constant willingness to rock; I'm looking forward to more music (and perhaps less so for debates about veganism).

Chu-Ping, this is my second acknowledgment: it's time to consider some naming rights. I want to take some extra space to thank you for the fantastic experiences we shared as members of the PICO band. We had amazing times while making music: bass, guitar, piano, trumpet, kazoo, and pretty much anything else we could (or could not yet-) play. I'm looking forward to creating more music together and sharing wonderful stages in the future.

Tereza, finally, Fran is sharing some feelings with you, even though it's hard to match the love you bring into our daily lives. You are among the kindest people I know, always spreading contagious laughter and offering never-ending hugs. You also have a remarkable ability to keep everyone in the band organized and help us create some amazing music together. I am happy to have such an awesome friend; I am looking forward to more awesome moments together.

Thomas, I had a wonderful time with you. Although it felt a bit odd at first, once I got to know you, I realized you are one of the kindest and funniest guys to hang out with. I'm so happy to be learning guitar using your old instrument and to learn from listening to you play. For those who haven't heard you yet, I can only describe the experience by quoting Jack Black: "Check this out, this guy's insane! [339]." I truly appreciate the time we've spent together, musical or not, and I'm looking forward to all the moments we will share in the future.

I would also like to acknowledge all the amazing people I shared moments with at EMAT, who were exceptional at work but even more so during after-work moments. You are all truly exceptional at what you do, but I would like to acknowledge the person I got to know through fun times outside of work:

- Dani: Preemoh, ha sido un verdadero placer conocerte y forjar una gran amistad. Es muy típico rajar del sol y de la lluvia, pero lo que realmente he disfrutado es charlar contigo sobre la vida, siempre con esa perspectiva tan clara y profunda sobre la ciencia. Agradezco enormemente tu vocación por ayudar y enseñar, siempre acompañada de un chistorete o alguna historia para sacar una sonrisa.
- **Zezhong**: You are a truly honorary member of the PICO band and one of our most enthusiastic listeners, known for your quirky sense of humor. As I got to know you better, I realized how enjoyable our conversations became, especially when sarcasm was involved. I also felt like an honorary member of the Chinese gang in Antwerp, often surpassing your spice tolerance levels. I wish you the best, and I hope to see you again soon!
- Saleh: Ugh, you again... Now, I purposely asked for it. I truly appreciate the distraction, time, and chaos you brought to our office whenever you felt like interrupting people, which seemed to be quite often. However, I believe your actions were more motivated by the fun we had when you came to hang out in the office. I really enjoyed our conversations, filled with questionable humor. While they sometimes had little depth, they consistently made me smile and helped me get through the day.
- Tim: What a guy! As both an office neighbor and a neighbor at home, I truly enjoyed all our time together, both at work and outside of it. you really helped me feel less like a lost sheep in EMAT. Whether it was barbecues, dwarf campaigns, random nights out, or pub quiz nights, I always appreciated our time together. Our conversations, filled with depth and humor, made every moment memorable.
- Hoelen: It has been a pleasure to learn from you. From the science talks to the nonsense discussions about France and the French, always accompanied by a sarcastic sense of humor (is that French?). I am thankful for all your advice and help to improve this work and my understanding of physics. I am confident that you will achieve great things in science, always demonstrating strong work ethics and a willingness to help others.
- Arno: Now you have to handle Saleh on your own. However, I believe you'll be able to make your code even slower for him. Overall, it was really enjoyable to

have you as a desk neighbor, always ready to discuss complex quantum mechanics misunderstandings or simply update the chart (which I hope you can continue to do).

- Luca: You have been an excellent office mate, helping to bring order to the chaos while also participating enough for everyone to have a great time. It was wonderful to have a half-Latin American colleague to share alfajores with and to discuss that other surreal side of the world.
- Tama: You are the most passionate scientist-baker I know. I believe that your enthusiasm for any task you undertake inspires many of us to move forward. Additionally, you played a crucial role in maintaining balance within the office, helping to keep all of us in the not-so-evil range (even though it was challenging).
- Lars and Alex: I truly appreciate having the best lab team! You are always willing to help and curious about the weird setups I created with the phase plate, helping me obtain some beautiful data. Whether at an EMAT party or during after-work drinks, I have always enjoyed discussing various topics with you.
- **Gert**: A true music lover who isn't afraid to be the first on the dance floor. Thank you for all the kindness and support you've provided throughout this project, whether it was a 3D print or a TikTok-style video showcasing cool physics. You always added a fantastic creative touch with your stunning graphics.
- Miek, Lydia, and Catherine: I am truly grateful for all the support from the
 administrative team. It was reassuring to return from a conference knowing that
 we had very little to worry about because you always had our backs. Additionally, I
 thoroughly enjoyed the music-related activities we organized for retirement parties
 and after-work events. Without your help, I wouldn't have been able to work so
 smoothly.

I could likely include many names in this acknowledgment section, but ultimately, EMAT is defined by its people. Without them, nothing would be possible. As long as we maintain a positive environment among colleagues, I am confident that the PhD and post-doc experiences will continue to yield success stories and impressive results, all thanks to the contributions of the people involved.

Bibliography

- [1] DH Sliney. What is light? the visible spectrum and beyond. *Eye*, 30(2):222–229, 2016. 2
- [2] Ernst Abbe. Beiträge zur theorie des mikroskops und der mikroskopischen wahrnehmung. *Archiv für mikroskopische Anatomie*, 9(1):413–468, 1873. 2
- [3] Louis De Broglie. *Recherches sur la théorie des quanta*. PhD thesis, Migration-université en cours d'affectation, 1924. 2, 24
- [4] Max Knoll and Ernst Ruska. Das elektronenmikroskop. *Zeitschrift für physik*, 78:318–339, 1932. 3
- [5] Robert Hooke. Micrographia: or some physiological descriptions of minute bodies made by magnifying glasses, with observations and inquiries thereupon. Courier Corporation, 2003. 4, 101
- [6] Horace C Beck. Early magnifying glasses. *The Antiquaries Journal*, 8(3):327–330, 1928. 3
- [7] Oxford. Microscope. Oxford English Dictionary Online. Accessed: September 19, 2024. 3
- [8] David B Williams, C Barry Carter, David B Williams, and C Barry Carter. *The transmission electron microscope*. Springer, 1996. 5, 9, 101, 102
- [9] Ludwig Reimer. *Transmission electron microscopy: physics of image formation and microanalysis*, volume 36. Springer, 2013. 6, 9, 15, 109
- [10] C Barry Carter and David B Williams. *Transmission electron microscopy: Diffraction, imaging, and spectrometry.* Springer, 2016. 6, 109
- [11] Alistair Kwan, John Dudley, and Eric Lantz. Who really discovered snell's law? *Physics World*, 15(4):64, 2002. 6
- [12] Max Born and Emil Wolf. *Principles of optics: electromagnetic theory of propagation, interference and diffraction of light*. Elsevier, 2013. 6
- [13] P. Kruit. Introduction to Charged Particle Optics: AP 3401. TU Delft, 2010. 9
- [14] Peter W Hawkes and Erich Kasper. *Principles of electron optics: Wave Optics*, volume 2. Academic press, 1996. 9
- [15] Marc De Graef. *Introduction to conventional transmission electron microscopy*. Cambridge University Press, 2003. 9, 57

- [16] Harald Rose and Dirk Preikszas. Outline of a versatile corrected leem. *Optik* (*Stuttgart*), 92:31–44, 1992. 10
- [17] R. M. Tromp, J. B. Hannon, A. W. Ellis, W. Wan, A. Berghaus, and O. Schaff. A new aberration-corrected, energy-filtered leem/peem instrument. i. principles and design. *Ultramicroscopy*, 110:852–861, 6 2010. 10
- [18] R. M. Tromp, J. B. Hannon, W. Wan, A. Berghaus, and O. Schaff. A new aberration-corrected, energy-filtered leem/peem instrument ii. operation and results. *Ultramicroscopy*, 127:25–39, 4 2013. 10
- [19] Hideto Dohi and Pieter Kruit. Design for an aberration corrected scanning electron microscope using miniature electron mirrors. *Ultramicroscopy*, 189:1–23, 2018. 10
- [20] Navid Abedzadeh, MAR Krielaart, Chung-Soo Kim, John Simonaitis, Richard Hobbs, Pieter Kruit, and Karl K Berggren. Electrostatic electron mirror in sem for simultaneous imaging of top and bottom surfaces of a sample. *Ultramicroscopy*, 226:113304, 2021. 10
- [21] Ibn Al-Haytham and Al Sabra. Kitāb al-manāzir. *I-III, edited by Al Sabra (Al-Majlis al-watanī li'l-thaqāfa wa'l-funn wa'l-ādāb, Kuwait, 1983), 1983.* 11
- [22] Philipp Ludwig Seidel. *Ueber die Theorie der Fehler, mit welchen die durch optische Instrumente gesehenen Bilder behaftet sind, und über die mathematischen Bedingungen ihrer Aufhebung.* Cotta, 1857. 11
- [23] Rik Brydson. *Aberration-corrected analytical transmission electron microscopy*, volume 280. Wiley Online Library, 2011. 11
- [24] Stephan Uhlemann and Maximilian Haider. Residual wave aberrations in the first spherical aberration corrected transmission electron microscope. *Ultramicroscopy*, 72(3-4):109–119, 1998. 11
- [25] Ernst Brüche and O Scherzer. Geometrische elektronenoptik. (No Title), 1934. 12
- [26] Otto Scherzer. Über einige fehler von elektronenlinsen. Zeitschrift für Physik, 101(9):593–603, 1936. 13
- [27] Roger Waters, David Gilmour, Richard Wright, Nick Mason, and Syd Barret. The dark side of the moon [vinyl recording]. In *The dark side of the moon*. EMI Studios (now Abbey Road Studios), 3 Abbey Rd., London NW8 9AY, United Kingdom, 1973. 13
- [28] Otto Scherzer. Spharische und chromatische korrektur von elektronen-linsen. *Optik*, 2:114–132, 1947. 13, 96
- [29] O Scherzer. The theoretical resolution limit of the electron microscope. *Journal of Applied Physics*, 20(1):20–29, 1949. 13
- [30] R Seeliger. Die spharische korrektur von elektronenlinsen mittels nichtrotationssymmetrischer abbildungselemente. *Optik*, 8:311–317, 1951. 13
- [31] GD Archard. Requirements contributing to the design of devices used in correcting electron lenses. *British Journal of Applied Physics*, 5(8):294, 1954. 13

- [32] G Mollenstedt. Elektronenmikroskopische bilder mit einem nach o. scherzer spharisch korrigierten objektiv. In *Proc. Int. Conf. on Electr. Micr.*, pages 694–698, 1954. 13
- [33] WE Meyer. Das praktische auflösungsvermögen von elektronenmikroskopen. *Optik*, 18:101–114, 1961. 13
- [34] VM Kelman and S Ya Yavor. Achromatic quadrupole electron lenses. *Soviet Physics-Technical Physics*, 6(12):1052, 1962. 13
- [35] AD Dymnikov and S Ya Yavor. Quadrupole lenses analogous to an axially symmetric system. *Zh. Tekhn. Fiz.*, 33, 1963. 13
- [36] DF Hardy. *Combined magnetic and electrostatic quadrupole electron lenses*. PhD thesis, University of Cambridge, 1969. 13
- [37] H Rose. Elektronenoptische aplanate. Optik, 34:285–311, 1971. 13
- [38] H Koops, G Kuck, and O Scherzer. Test of an electron-optical achromator. *Optik*, 48(2):225–236, 1977. 13
- [39] Wilfried Bernhard. Erprobung eines sphärisch und chromatisch korrigierten elektronenmikroskopes. *Optik*, 57:73–94, 1980. 13
- [40] H Rose. Outline of a spherically corrected semiaplanatic medium-voltage transmission electron microscope. *Optik*, 85:19–24, 1990. 13, 34
- [41] Maximilian Haider, Gerhard Braunshausen, and Eugen Schwan. Correction of the spherical aberration of a 200 kv tem by means of a hexapole-corrector. *Optik*, 99:167–179, 1995. 13, 34
- [42] Maximilian Haider, Stephan Uhlemann, Eugen Schwan, Harald H. Rose, Bernd C. Kabius, and Knut W. Urban. Electron microscopy image enhanced. *Nature*, 392:768–769, 1998. 13, 34
- [43] Harald H Rose. Historical aspects of aberration correction. *Journal of electron microscopy*, 58(3):77–85, 2009. 13
- [44] Shigeyuki Morishita, Ryo Ishikawa, Yuji Kohno, Hidetaka Sawada, Naoya Shibata, and Yuichi Ikuhara. Attainment of 40.5 pm spatial resolution using 300 kv scanning transmission electron microscope equipped with fifth-order aberration corrector. *Microscopy*, 67(1):46–50, 2018. 14
- [45] Harald Rose. Aberration correction in electron microscopy. *International journal of materials research*, 97(7):885–889, 2022. 14
- [46] Takeo Sasaki, Hidetaka Sawada, Fumio Hosokawa, Yuji Kohno, Takeshi Tomita, Toshikatsu Kaneyama, Yukihito Kondo, Koji Kimoto, Yuta Sato, and Kazu Suenaga. Performance of low-voltage stem/tem with delta corrector and cold field emission gun. *Journal of Electron Microscopy*, 59(S1):S7–S13, 2010. 14
- [47] H Sawada, T Sasaki, F Hosokawa, S Yuasa, M Terao, M Kawazoe, T Nakamichi, T Kaneyama, Y Kondo, K Kimoto, et al. Higher-order aberration corrector for an image-forming system in a transmission electron microscope. *Ultramicroscopy*, 110(8):958–961, 2010. 14

- [48] Takeo Sasaki, Hidetaka Sawada, Fumio Hosokawa, Yuta Sato, and Kazu Suenaga. Aberration-corrected stem/tem imaging at 15 kv. *Ultramicroscopy*, 145:50–55, 2014. 14
- [49] D Van Dyck. Persistent misconceptions about incoherence in electron microscopy. *Ultramicroscopy*, 111(7):894–900, 2011. 14
- [50] Christian Dwyer, Rolf Erni, and Joanne Etheridge. Measurement of effective source distribution and its importance for quantitative interpretation of stem images. *Ultramicroscopy*, 110(8):952–957, 2010. 14
- [51] George R Bird, R Clark Jones, and Allan E Ames. The efficiency of radiation detection by photographic films: State-of-the-art and methods of improvement. *Applied Optics*, 8(12):2389–2405, 1969. 15
- [52] PTE Roberts, JN Chapman, and AM MacLeod. A ccd-based image recording system for the ctem. *Ultramicroscopy*, 8(4):385–396, 1982. 15
- [53] JCH Spence and JM Zuo. Large dynamic range, parallel detection system for electron diffraction and imaging. *Review of Scientific Instruments*, 59(9):2102–2105, 1988. 15
- [54] AR Faruqi and G McMullan. Direct imaging detectors for electron microscopy. Nuclear Instruments and Methods in Physics Research Section A: Accelerators, Spectrometers, Detectors and Associated Equipment, 878:180–190, 2018. 15
- [55] Knut W Urban. Studying atomic structures by aberration-corrected transmission electron microscopy. *Science*, 321(5888):506–510, 2008. 16
- [56] Christian Kisielowski, B Freitag, M Bischoff, H Van Lin, S Lazar, Georg Knippels, Peter Tiemeijer, Maarten van der Stam, Sebastian von Harrach, Michael Stekelenburg, et al. Detection of single atoms and buried defects in three dimensions by aberration-corrected electron microscope with 0.5-å information limit. *Microscopy and Microanalysis*, 14(5):469–477, 2008. 16
- [57] Werner Brandt. Channeling in crystals. Scientific American, 218(3):90–101, 1968. 17
- [58] P Geuens and D Van Dyck. The s-state model for electron channeling in high-resolution electron microscopy. *Advances in Imaging and Electron Physics*, 136:111–226, 2005. 17
- [59] Ray F Egerton. Electron energy-loss spectroscopy in the tem. *Reports on Progress in Physics*, 72(1):016502, 2008. 18
- [60] Satoshi Utsunomiya and Rodney C Ewing. Application of high-angle annular dark field scanning transmission electron microscopy, scanning transmission electron microscopy-energy dispersive x-ray spectrometry, and energy-filtered transmission electron microscopy to the characterization of nanoparticles in the environment. *Environmental science & technology*, 37(4):786–791, 2003. 18
- [61] NR Lugg, Gerald Kothleitner, N Shibata, and Y Ikuhara. On the quantitativeness of eds stem. *Ultramicroscopy*, 151:150–159, 2015. 18

- [62] Thomas JA Slater, Arne Janssen, Pedro HC Camargo, M Grace Burke, Nestor J Zaluzec, and Sarah J Haigh. Stem-edx tomography of bimetallic nanoparticles: A methodological investigation. *Ultramicroscopy*, 162:61–73, 2016. 18
- [63] Nahid Talebi. Interaction of electron beams with optical nanostructures and metamaterials: from coherent photon sources towards shaping the wave function. *Journal of Optics*, 19(10):103001, 2017. 18
- [64] Michael Shentcis, Adam K Budniak, Xihang Shi, Raphael Dahan, Yaniv Kurman, Michael Kalina, Hanan Herzig Sheinfux, Mark Blei, Mark Kamper Svendsen, Yaron Amouyal, et al. Tunable free-electron x-ray radiation from van der waals materials. *Nature Photonics*, 14(11):686–692, 2020. 18
- [65] Liang Jie Wong and Ido Kaminer. Prospects in x-ray science emerging from quantum optics and nanomaterials. *Applied Physics Letters*, 119(13), 2021. 18
- [66] Lee Wei Wesley Wong, Xihang Shi, Aviv Karnieli, Jeremy Lim, Suraj Kumar, Sergio Carbajo, Ido Kaminer, and Liang Jie Wong. Free-electron crystals for enhanced x-ray radiation. *Light: Science & Applications*, 13(1):29, 2024. 18, 98
- [67] Francisco Javier García de Abajo. Optical excitations in electron microscopy. *Reviews of modern physics*, 82(1):209–275, 2010. 18
- [68] Luiz Fernando Zagonel, Stefano Mazzucco, Marcel Tencé, Katia March, Romain Bernard, Benoît Laslier, Gwénolé Jacopin, Maria Tchernycheva, Lorenzo Rigutti, Francois H Julien, et al. Nanometer scale spectral imaging of quantum emitters in nanowires and its correlation to their atomically resolved structure. *Nano letters*, 11(2):568–573, 2011. 18
- [69] DRG Mitchell and G Casillas. Secondary electron imaging in an aberration-corrected stem. *Microscopy Today*, 24(5):22–27, 2016. 18
- [70] Evgenii Vlasov, Alexander Skorikov, Ana Sánchez-Iglesias, Luis M Liz-Marzán, Johan Verbeeck, and Sara Bals. Secondary electron induced current in scanning transmission electron microscopy: an alternative way to visualize the morphology of nanoparticles. ACS Materials Letters, 5(7):1916–1921, 2023. 18
- [71] GG Hembree, JS Drucker, FCH Luo, M Krishnamurthy, and JA Venables. Auger electron spectroscopy and microscopy with probe-size limited resolution. *Applied physics letters*, 58(17):1890–1892, 1991. 18
- [72] 24_S J Pennycook. Z-contrast stem for materials science. *Ultramicroscopy*, 30(1-2):58–69, 1989. 18
- [73] Yiping Peng, Peter D Nellist, and Stephen J Pennycook. Haadf-stem imaging with sub-angstrom probes: a full bloch wave analysis. *Journal of electron microscopy*, 53(3):257–266, 2004. 18
- [74] Sandra Van Aert, Jo Verbeeck, Rolf Erni, Sara Bals, M Luysberg, D Van Dyck, and Gustaaf Van Tendeloo. Quantitative atomic resolution mapping using high-angle annular dark field scanning transmission electron microscopy. *Ultramicroscopy*, 109(10):1236–1244, 2009. 18

- [75] PD Nellist and SJ Pennycook. The principles and interpretation of annular darkfield z-contrast imaging. In *Advances in imaging and electron physics*, volume 113, pages 147–203. Elsevier, 2000. 18
- [76] KE MacArthur, AJ D'Alfonso, D Ozkaya, LJ Allen, and PD Nellist. Optimal adf stem imaging parameters for tilt-robust image quantification. *Ultramicroscopy*, 156:1–8, 2015. 18
- [77] Eiji Okunishi, Isamu Ishikawa, Hidetaka Sawada, Fumio Hosokawa, Madoka Hori, and Yukihito Kondo. Visualization of light elements at ultrahigh resolution by stem annular bright field microscopy. *Microscopy and Microanalysis*, 15(S2):164–165, 2009. 18
- [78] Eiji Okunishi, Hidetaka Sawada, and Yukihito Kondo. Experimental study of annular bright field (abf) imaging using aberration-corrected scanning transmission electron microscopy (stem). *Micron*, 43(4):538–544, 2012. 18
- [79] Hans Bethe. Zur theorie des durchgangs schneller korpuskularstrahlen durch materie. *Annalen der Physik*, 397(3):325–400, 1930. 18
- [80] Nevill Francis Mott. The scattering of electrons by atoms. *Proceedings of the Royal Society of London. Series A, Containing Papers of a Mathematical and Physical Character*, 127(806):658–665, 1930. 18
- [81] John M Cowley. Image contrast in a transmission scanning electron microscope. *Applied Physics Letters*, 15(2):58–59, 1969. 19
- [82] Florian F Krause and Andreas Rosenauer. Reciprocity relations in transmission electron microscopy: A rigorous derivation. *Micron*, 92:1–5, 2017. 19
- [83] Knut Müller, Henning Ryll, Ivan Ordavo, Sebastian Ihle, Lothar Strüder, Kerstin Volz, Josef Zweck, Heike Soltau, and Andreas Rosenauer. Scanning transmission electron microscopy strain measurement from millisecond frames of a direct electron charge coupled device. *Applied Physics Letters*, 101(21), 2012. 19
- [84] Knut Müller, Florian F Krause, Armand Béché, Marco Schowalter, Vincent Galioit, Stefan Löffler, Johan Verbeeck, Josef Zweck, Peter Schattschneider, and Andreas Rosenauer. Atomic electric fields revealed by a quantum mechanical approach to electron picodiffraction. *Nature communications*, 5(1):5653, 2014. 19
- [85] Karen C Bustillo, Steven E Zeltmann, Min Chen, Jennifer Donohue, Jim Ciston, Colin Ophus, and Andrew M Minor. 4d-stem of beam-sensitive materials. *Accounts of chemical research*, 54(11):2543–2551, 2021. 19
- [86] Knut Müller-Caspary, Florian F Krause, Florian Winkler, Armand Béché, Johan Verbeeck, Sandra Van Aert, and Andreas Rosenauer. Comparison of first moment stem with conventional differential phase contrast and the dependence on electron dose. *Ultramicroscopy*, 203:95–104, 2019. 19, 69
- [87] H Yang, L Jones, H Ryll, M Simson, H Soltau, Y Kondo, R Sagawa, H Banba, I MacLaren, and PD Nellist. 4d stem: High efficiency phase contrast imaging using a fast pixelated detector. In *Journal of Physics: Conference Series*, volume 644, page 012032. IOP Publishing, 2015. 19

- [88] Kayla X Nguyen, Yi Jiang, Chia-Hao Lee, Priti Kharel, Yue Zhang, Arend M van der Zande, and Pinshane Y Huang. Achieving sub-0.5-angstrom–resolution ptychography in an uncorrected electron microscope. *Science*, 383(6685):865–870, 2024. 19, 99
- [89] Zhen Chen, Yi Jiang, Yu-Tsun Shao, Megan E Holtz, Michal Odstrčil, Manuel Guizar-Sicairos, Isabelle Hanke, Steffen Ganschow, Darrell G Schlom, and David A Muller. Electron ptychography achieves atomic-resolution limits set by lattice vibrations. *Science*, 372(6544):826–831, 2021. 20, 69
- [90] Guinness World Records. Highest resolution microscope. Accessed: 2024-11-06. 20
- [91] François Roddier. *Adaptive optics in astronomy*. Cambridge University Press, 1999. 22
- [92] Cecilia Barnbaum and Richard F Bradley. A new approach to interference excision in radio astronomy: Real-time adaptive cancellation. *The astronomical journal*, 116(5):2598, 1998. 22
- [93] Lawrence E Brennan and LS Reed. Theory of adaptive radar. *IEEE transactions on Aerospace and Electronic Systems*, AES-9(2):237–252, 1973. 22
- [94] Ulf Michel. History of acoustic beamforming. In 1st. Berlin Beamforming Conference, 2006. 22
- [95] N Davids, EG Thurston, and RE Mueser. The design of optimum directional acoustic arrays. *The Journal of the Acoustical Society of America*, 24(1):50–56, 1952. 22
- [96] John Billingsley and R Kinns. The acoustic telescope. *Journal of Sound and Vibration*, 48(4):485–510, 1976. 22
- [97] Martijn PA van den Ende and Jean-Paul Ampuero. Evaluating seismic beamforming capabilities of distributed acoustic sensing arrays. *Solid Earth*, 12(4):915–934, 2021. 22
- [98] PS Hall and SJ Vetterlein. Review of radio frequency beamforming techniques for scanned and multiple beam antennas. In *IEE Proceedings H (Microwaves, Antennas and Propagation)*, volume 137, pages 293–303. IET, 1990. 22
- [99] Hang Yu, Lin Zhong, Ashutosh Sabharwal, and David Kao. Beamforming on mobile devices: A first study. In *Proceedings of the 17th annual international conference on Mobile computing and networking*, pages 265–276, 2011. 22
- [100] AD Fisher. A review of spatial light modulators. *Optical Computing*, page TuC1, 1985. 22
- [101] Christian Maurer, Alexander Jesacher, Stefan Bernet, and Monika Ritsch-Marte. What spatial light modulators can do for optical microscopy. *Laser & Photonics Reviews*, 5(1):81–101, 2011. 22
- [102] Yiqian Yang, Andrew Forbes, and Liangcai Cao. A review of liquid crystal spatial light modulators: devices and applications. *Opto-Electronic Science*, 2(8):230026–1, 2023. 22

- [103] Knut W Urban, Chun-Lin Jia, Lothar Houben, Markus Lentzen, Shao-Bo Mi, and Karsten Tillmann. Negative spherical aberration ultrahigh-resolution imaging in corrected transmission electron microscopy. *Philosophical Transactions of the Royal Society A: Mathematical, Physical and Engineering Sciences*, 367(1903):3735– 3753, 2009. 23
- [104] PW Hawkes. Aberration correction past and present. *Philosophical Transactions of the Royal Society A: Mathematical, Physical and Engineering Sciences*, 367(1903):3637–3664, 2009. 23
- [105] CL Jia, Lothar Houben, A Thust, and J Barthel. On the benefit of the negative-spherical-aberration imaging technique for quantitative hrtem. *Ultramicroscopy*, 110(5):500–505, 2010. 23
- [106] Giulio Guzzinati, Laura Clark, Armand Béché, Roeland Juchtmans, Ruben Van Boxem, Michael Mazilu, and Jo Verbeeck. Prospects for versatile phase manipulation in the tem: Beyond aberration correction. *Ultramicroscopy*, 151:85–93, 2015. 23
- [107] Giulio Guzzinati, Armand Béché, Hugo Lourenço-Martins, Jérôme Martin, Mathieu Kociak, and Jo Verbeeck. Probing the symmetry of the potential of localized surface plasmon resonances with phase-shaped electron beams. *Nature Communications*, 8(1):14999, 2017. 23, 31, 48, 62, 98
- [108] Paul Adrien Maurice Dirac. The quantum theory of the electron. *Proceedings of the Royal Society of London. Series A, Containing Papers of a Mathematical and Physical Character*, 117(778):610–624, 1928. 24
- [109] Mark Srednicki. Quantum field theory. Cambridge University Press, 2007. 24
- [110] David J Griffiths and Darrell F Schroeter. *Introduction to quantum mechanics*. Cambridge university press, 2019. 24
- [111] Kunio Fujiwara. Relativistic dynamical theory of electron diffraction. *Journal of the Physical Society of Japan*, 16(11):2226–2238, 1961. 24
- [112] William Rowan Hamilton. *On a general method in dynamics*. Richard Taylor United Kindom, 1834. 24
- [113] Werner Heisenberg. Über quantentheoretische Umdeutung kinematischer und mechanischer Beziehungen. Springer, 1985. 24
- [114] Earl J Kirkland. Advanced Computing in Electron Microscopy. Springer, 2010. 24
- [115] D Van Dyck. Is the frozen phonon model adequate to describe inelastic phonon scattering? *Ultramicroscopy*, 109(6):677–682, 2009. 24
- [116] Isaac Newton. *Opticks, or, a treatise of the reflections, refractions, inflections & colours of light*. Courier Corporation, 1952. 25
- [117] Christiaan Huygens. Traité de la lumiere; ou y sont expliquées les causes de ce qui luy arrive dans la reflexion et dans la refraction et particulierement dans l'étrange refraction du cristal d'islande. Gressner & Schramm, 1885. 25

- [118] Thomas Young. I. the bakerian lecture. experiments and calculations relative to physical optics. *Philosophical transactions of the Royal Society of London*, 94(94):1–16, 1804. 25
- [119] Geoffrey Ingram Taylor. Interference fringes with feeble light. In *Proceedings of the Cambridge Philosophical Society*, volume 15, pages 114–115, 1909. 25
- [120] Paul Adrien Maurice Dirac. *The principles of quantum mechanics*. Number 27 in International Series of Monographs on Physics. Oxford university press, 1981. 25
- [121] Clinton Davisson and Lester H Germer. Diffraction of electrons by a crystal of nickel. *Physical review*, 30(6):705, 1927. 25
- [122] Claus Jönsson. Elektroneninterferenzen an mehreren künstlich hergestellten feinspalten. Zeitschrift für Physik, 161(4):454–474, 1961. 25
- [123] Pier Giorgio Merli, Gian Franco Missiroli, and Giulio Pozzi. On the statistical aspect of electron interference phenomena. *Am. J. Phys*, 44(3):306–307, 1976. 25
- [124] Akira Tonomura, J Endo, T Matsuda, T Kawasaki, and H Ezawa. Demonstration of single-electron buildup of an interference pattern. *Am. J. Phys*, 57(2):117–120, 1989. 25
- [125] Yakir Aharonov and David Bohm. Significance of electromagnetic potentials in the quantum theory. *Physical Review*, 115(3):485, 1959. 26, 27, 103
- [126] Hans Boersch. Über die kontraste von atomen im elektronenmikroskop. *Zeitschrift für Naturforschung A*, 2(11-12):615–633, 1947. 28, 29, 103
- [127] Takao Matsumoto and Akira Tonomura. The phase constancy of electron waves traveling through boersch's electrostatic phase plate. *Ultramicroscopy*, 63(1):5–10, 1996. 28, 29, 34, 54, 103
- [128] E Majorovits, Bastian Barton, K Schultheiss, F Perez-Willard, D Gerthsen, and Rasmus R Schröder. Optimizing phase contrast in transmission electron microscopy with an electrostatic (boersch) phase plate. *Ultramicroscopy*, 107(2-3):213–226, 2007. 28, 52
- [129] Jessie Shiue, Chia-Seng Chang, Sen-Hui Huang, Chih-Hao Hsu, Jin-Sheng Tsai, Wei-Hau Chang, Yi-Min Wu, Yen-Chen Lin, Pai-Chia Kuo, Yang-Shan Huang, et al. Phase tem for biological imaging utilizing a boersch electrostatic phase plate: theory and practice. *Journal of electron microscopy*, 58(3):137–145, 2009. 28
- [130] Frits Zernike. Diffraction theory of the knife-edge test and its improved form, the phase-contrast method. *Monthly Notices of the Royal Astronomical Society, Vol. 94, p.* 377-384, 94:377–384, 1934. 28, 57
- [131] Frits Zernike. Phase contrast, a new method for the microscopic observation of transparent objects. *Physica*, 9(7):686–698, 1942. 28, 69, 71
- [132] Frits Zernike. Phase contrast, a new method for the microscopic observation of transparent objects part ii. *Physica*, 9(10):974–986, 1942. 28, 69, 71
- [133] K Schultheiss, F Pérez-Willard, B Barton, D Gerthsen, and RR Schröder. Fabrication of a boersch phase plate for phase contrast imaging in a transmission electron microscope. *Review of scientific instruments*, 77(3):033701, 2006. 29, 34, 52

- [134] Ko-Feng Chen, Chia-Seng Chang, Jessie Shiue, Yeukuang Hwu, Wei-Hau Chang, Ji-Jung Kai, and Fu-Rong Chen. Study of mean absorptive potential using lenz model: Toward quantification of phase contrast from an electrostatic phase plate. *Micron*, 39(6):749–756, 2008. 29
- [135] D Alloyeau, WK Hsieh, EH Anderson, L Hilken, G Benner, X Meng, FR Chen, and C Kisielowski. Imaging of soft and hard materials using a boersch phase plate in a transmission electron microscope. *Ultramicroscopy*, 110(5):563–570, 2010. 29
- [136] Bastian Barton, Daniel Rhinow, Andreas Walter, R Schröder, Gerd Benner, Endre Majorovits, Marko Matijevic, H Niebel, H Müller, Maximilian Haider, et al. Infocus electron microscopy of frozen-hydrated biological samples with a boersch phase plate. *Ultramicroscopy*, 111(12):1696–1705, 2011. 29
- [137] H Tamaki, H Kasai, K Harada, Y Takahashi, and R Nishi. Development of a contact-potential-type phase plate. *Microscopy and Microanalysis*, 19(S2):1148–1149, 2013.
- [138] Joachim Zach. Phase plate, imaging method, and electron microscope, April 19 2011. US Patent 7,928,379. 29
- [139] Katrin Schultheiss, Joachim Zach, Bjoern Gamm, Manuel Dries, Nicole Frindt, Rasmus R Schröder, and Dagmar Gerthsen. New electrostatic phase plate for phase-contrast transmission electron microscopy and its application for wavefunction reconstruction. *Microscopy and Microanalysis*, 16(6):785–794, 2010. 29, 52
- [140] Simon Hettler, Björn Gamm, Manuel Dries, Nicole Frindt, Rasmus R Schröder, and Dagmar Gerthsen. Improving fabrication and application of zach phase plates for phase-contrast transmission electron microscopy. *Microscopy and Microanalysis*, 18(5):1010–1015, 2012. 29, 34
- [141] Simon Hettler, Jochen Wagner, Manuel Dries, Marco Oster, Christian Wacker, Rasmus R Schröder, and Dagmar Gerthsen. On the role of inelastic scattering in phase-plate transmission electron microscopy. *Ultramicroscopy*, 155:27–41, 2015. 29
- [142] Nicole Frindt, Marco Oster, Simon Hettler, Björn Gamm, Levin Dieterle, Wolfgang Kowalsky, Dagmar Gerthsen, and Rasmus R Schröder. In-focus electrostatic zach phase plate imaging for transmission electron microscopy with tunable phase contrast of frozen hydrated biological samples. *Microscopy and Microanalysis*, 20(1):175–183, 2014. 29, 52
- [143] Simon Hettler, Manuel Dries, J Zeelen, Marco Oster, Rasmus R Schröder, and Dagmar Gerthsen. High-resolution transmission electron microscopy with an electrostatic zach phase plate. *New Journal of Physics*, 18(5):053005, 2016. 29
- [144] Jo Verbeeck, Armand Béché, Knut Müller-Caspary, Giulio Guzzinati, Minh Anh Luong, and Martien Den Hertog. Demonstration of a 2x2 programmable phase plate for electrons. *Ultramicroscopy*, 190:58–65, 7 2018. 30, 46, 52, 57, 70, 96, 98, 99, 103

- [145] Pooja Thakkar, Vitaliy A Guzenko, Peng-Han Lu, Rafal E Dunin-Borkowski, Jan Pieter Abrahams, and Soichiro Tsujino. Fabrication of low aspect ratio three-element boersch phase shifters for voltage-controlled three electron beam interference. *Journal of Applied Physics*, 128(13), 2020. 30
- [146] Pooja Thakkar, Vitaliy A Guzenko, Peng-Han Lu, Rafal E Dunin-Borkowski, Jan Pieter Abrahams, and Soichiro Tsujino. Electrostatic interference control of a high-energy coherent electron beam using a three-element boersch phase shifter. arXiv preprint arXiv:2407.06554, 2024. 30
- [147] Hugo Lourenço-Martins. Development of phase-shaped electron energy-loss spectroscopy for nano-optics. In *Advances in Imaging and Electron Physics*, volume 222, pages 139–235. Elsevier, 2022. 31, 48, 62, 98
- [148] Franck Aguilar, Hugo Lourenço-Martins, Damián Montero, Xiaoyan Li, Mathieu Kociak, and Alfredo Campos. Selective probing of longitudinal and transverse plasmon modes with electron phase-matching. *The Journal of Physical Chemistry C*, 127(45):22252–22264, 2023. 31, 98
- [149] Vincenzo Grillo, Ebrahim Karimi, Gian Carlo Gazzadi, Stefano Frabboni, Mark R Dennis, and Robert W Boyd. Generation of nondiffracting electron bessel beams. *Physical Review X*, 4(1):011013, 2014. 34
- [150] F Javier García de Abajo and Andrea Konečná. Optical modulation of electron beams in free space. *Physical Review Letters*, 126(12):123901, 2021. 34, 52
- [151] Kangpeng Wang, Raphael Dahan, Michael Shentcis, Yaron Kauffmann, Adi Ben Hayun, Ori Reinhardt, Shai Tsesses, and Ido Kaminer. Coherent interaction between free electrons and a photonic cavity. *Nature*, 582(7810):50–54, 2020. 34
- [152] Jared Maxson, Hyeri Lee, Adam C Bartnik, Jacob Kiefer, and Ivan Bazarov. Adaptive electron beam shaping using a photoemission gun and spatial light modulator. *Physical Review Special Topics-Accelerators and Beams*, 18(2):023401, 2015. 34
- [153] Marius Constantin Chirita Mihaila, Philipp Weber, Matthias Schneller, Lucas Grandits, Stefan Nimmrichter, and Thomas Juffmann. Transverse electron-beam shaping with light. *Physical Review X*, 12(3):031043, 2022. 34
- [154] Andrea Konečná and F Javier García de Abajo. Electron beam aberration correction using optical near fields. *Physical Review Letters*, 125(3):030801, 2020. 34
- [155] Kuniaki Nagayama and Radostin Danev. Phase-plate electron microscopy: a novel imaging tool to reveal close-to-life nano-structures. *Biophysical reviews*, 1(1):37–42, 2009. 34
- [156] Rossana Cambie, Kenneth H Downing, Dieter Typke, Robert M Glaeser, and Jian Jin. Design of a microfabricated, two-electrode phase-contrast element suitable for electron microscopy. *Ultramicroscopy*, 107(4-5):329–339, 2007. 34
- [157] Armand Béché, R Juchtmans, and J Verbeeck. Efficient creation of electron vortex beams for high resolution stem imaging. *Ultramicroscopy*, 178:12–19, 2017. 34, 57

- [158] H Kohl and H Rose. Theory of image formation by inelastically scattered electrons in the electron microscope. In *Advances in electronics and electron physics*, volume 65, pages 173–227. Elsevier, 1985. 35
- [159] JR Michael and DB Williams. A consistent definition of probe size and spatial resolution in the analytical electron microscope. *Journal of Microscopy*, 147(3):289–303, 1987. 35
- [160] HS Von Harrach. Instrumental factors in high-resolution feg stem. *Ultramicroscopy*, 58(1):1–5, 1995. 35
- [161] Daniel S Engstrom, B Porter, M Pacios, and H Bhaskaran. Additive nanomanufacturing–a review. *Journal of Materials Research*, 29(17):1792–1816, 2014. 42, 46, 104
- [162] Karl Strehl. Aplanatische und fehlerhafte abbildung im fernrohr. Zeitschrift für Instrumentenkunde, 15(7):362–370, 1895. 48, 56
- [163] Virendra N Mahajan. Strehl ratio for primary aberrations: some analytical results for circular and annular pupils. *JOSA*, 72(9):1258–1266, 1982. 48
- [164] Virendra N Mahajan. Strehl ratio for primary aberrations in terms of their aberration variance. *JOSA*, 73(6):860–861, 1983. 48, 56
- [165] Narupon Chattrapiban, Elizabeth A Rogers, David Cofield, Wendell T Hill III, and Rajarshi Roy. Generation of nondiffracting bessel beams by use of a spatial light modulator. *Optics letters*, 28(22):2183–2185, 2003. 48
- [166] SH Tao, WM Lee, and X-C Yuan. Dynamic optical manipulation with a higher-order fractional bessel beam generated from a spatial light modulator. *Optics letters*, 28(20):1867–1869, 2003. 48
- [167] Fucai Zhang, Giancarlo Pedrini, and Wolfgang Osten. Phase retrieval of arbitrary complex-valued fields through aperture-plane modulation. *Physical Review A*, 75(4):043805, 2007. 48
- [168] Fucai Zhang and JM Rodenburg. Phase retrieval based on wave-front relay and modulation. *Physical Review B*, 82(12):121104, 2010. 48
- [169] Claas Falldorf, Mostafa Agour, Christoph von Kopylow, and Ralf B Bergmann. Design of an optical system for phase retrieval based on a spatial light modulator. In *AIP Conference Proceedings*, volume 1236, pages 259–264. American Institute of Physics, 2010. 48
- [170] Albert Fannjiang and Wenjing Liao. Phase retrieval with random phase illumination. *Journal of the Optical Society of America A*, 29(9):1847, 9 2012. 48, 69, 82, 87
- [171] Radostin Danev and Kuniaki Nagayama. Transmission electron microscopy with zernike phase plate. *Ultramicroscopy*, 88(4):243–252, 2001. 52, 69
- [172] Radostin Danev and Kuniaki Nagayama. Single particle analysis based on zernike phase contrast transmission electron microscopy. *Journal of structural biology*, 161(2):211–218, 2008. 52, 69

- [173] Radostin Danev and Wolfgang Baumeister. Cryo-em single particle analysis with the volta phase plate. *elife*, 5:e13046, 2016. 52
- [174] Radostin Danev, Bart Buijsse, Maryam Khoshouei, Jürgen M Plitzko, and Wolfgang Baumeister. Volta potential phase plate for in-focus phase contrast transmission electron microscopy. *Proceedings of the National Academy of Sciences*, 111(44):15635–15640, 2014. 52, 72
- [175] Bart Buijsse, Piet Trompenaars, Veli Altin, Radostin Danev, and Robert M Glaeser. Spectral dge of the volta phase plate. *Ultramicroscopy*, 218:113079, 2020. 52
- [176] Meeri Kim. Large electron vortex beams produced by mems-based device, 2022. 52
- [177] Colin Ophus, Jim Ciston, Jordan Pierce, Tyler R Harvey, Jordan Chess, Benjamin J McMorran, Cory Czarnik, Harald H Rose, and Peter Ercius. Efficient linear phase contrast in scanning transmission electron microscopy with matched illumination and detector interferometry. *Nature communications*, 7(1):10719, 2016. 52
- [178] Hao Yang, Peter Ercius, Peter D Nellist, and Colin Ophus. Enhanced phase contrast transfer using ptychography combined with a pre-specimen phase plate in a scanning transmission electron microscope. *Ultramicroscopy*, 171:117–125, 2016. 52
- [179] Amir H Tavabi, Paolo Rosi, Enzo Rotunno, Alberto Roncaglia, Luca Belsito, Stefano Frabboni, Giulio Pozzi, Gian Carlo Gazzadi, Peng-Han Lu, Robert Nijland, et al. Experimental demonstration of an electrostatic orbital angular momentum sorter for electron beams. *Physical review letters*, 126(9):094802, 2021. 52, 99
- [180] Vincenzo Grillo, Amir H Tavabi, Federico Venturi, Hugo Larocque, Roberto Balboni, Gian Carlo Gazzadi, Stefano Frabboni, Peng-Han Lu, Erfan Mafakheri, Frédéric Bouchard, et al. Measuring the orbital angular momentum spectrum of an electron beam. *Nature Communications*, 8(1):15536, 2017. 52
- [181] AH Tavabi, P Rosi, A Roncaglia, E Rotunno, M Beleggia, P-H Lu, L Belsito, G Pozzi, S Frabboni, P Tiemeijer, et al. Generation of electron vortex beams with over 1000 orbital angular momentum quanta using a tunable electrostatic spiral phase plate. *Applied Physics Letters*, 121(7):073506, 2022. 52
- [182] B Barwick and Herman Batelaan. Aharonov–bohm phase shifts induced by laser pulses. *New Journal of Physics*, 10(8):083036, 2008. 52
- [183] Marius Constantin Chirita Mihaila, Philipp Weber, Matthias Schneller, Lucas Grandits, Stefan Nimmrichter, and Thomas Juffmann. Transverse electron-beam shaping with light. *Physical Review X*, 12(3):031043, 2022. 52, 99
- [184] Holger Mueller, Jian Jin, Radostin Danev, John Spence, Howard Padmore, and Robert M Glaeser. Design of an electron microscope phase plate using a focused continuous-wave laser. *New journal of physics*, 12(7):073011, 2010. 52
- [185] Osip Schwartz, Jeremy J Axelrod, Sara L Campbell, Carter Turnbaugh, Robert M Glaeser, and Holger Müller. Laser phase plate for transmission electron microscopy. *Nature methods*, 16(10):1016–1020, 2019. 52

- [186] AdaptEM eu. Adaptem, 2021. https://adaptem.eu/. 54, 92, 93, 107
- [187] Ralph W Gerchberg. A practical algorithm for the determination of plane from image and diffraction pictures. *Optik*, 35(2):237–246, 1972. 54, 71, 79
- [188] RW Gerchberg. Super-resolution through error energy reduction. *Optica Acta: International Journal of Optics*, 21(9):709–720, 1974. 54, 79
- [189] J. R. Fienup. Phase retrieval algorithms: a comparison. *Applied Optics*, 21(15):2758, 8 1982. 55, 68, 69, 87
- [190] Jacques Hadamard. Resolution d'une question relative aux determinants. *Bull. des sciences math.*, 2:240–246, 1893. 57, 82
- [191] Johan Verbeeck, He Tian, and Peter Schattschneider. Production and application of electron vortex beams. *Nature*, 467(7313):301–304, 2010. 57
- [192] Erich Zauderer. Complex argument hermite–gaussian and laguerre–gaussian beams. *JOSA A*, 3(4):465–469, 1986. 57
- [193] Akira Tonomura. Applications of electron holography. *Reviews of modern physics*, 59(3):639, 1987. 58
- [194] WMJ Coene, A Thust, M Op De Beeck, and D Van Dyck. Maximum-likelihood method for focus-variation image reconstruction in high resolution transmission electron microscopy. *Ultramicroscopy*, 64(1-4):109–135, 1996. 58
- [195] C Ozsoy-Keskinbora, CB Boothroyd, RE Dunin-Borkowski, PA Van Aken, and CT Koch. Hybridization approach to in-line and off-axis (electron) holography for superior resolution and phase sensitivity. *Scientific reports*, 4(1):1–10, 2014. 58
- [196] Robert Hovden, Huolin L Xin, and David A Muller. Extended depth of field for high-resolution scanning transmission electron microscopy. *Microscopy and Microanalysis*, 17(1):75–80, 2011. 59
- [197] Klaus van Benthem, Andrew R Lupini, Mark P Oxley, Scott D Findlay, Leslie J Allen, and Stephen J Pennycook. Three-dimensional adf imaging of individual atoms by through-focal series scanning transmission electron microscopy. *Ultramicroscopy*, 106(11-12):1062–1068, 2006. 59
- [198] DT Nguyen, SD Findlay, and J Etheridge. A menu of electron probes for optimising information from scanning transmission electron microscopy. *Ultramicroscopy*, 184:143–155, 2018. 59
- [199] Hans Blom and Jerker Widengren. Stimulated emission depletion microscopy. *Chemical reviews*, 117(11):7377–7427, 2017. 59
- [200] Birka Hein, Katrin I Willig, and Stefan W Hell. Stimulated emission depletion (sted) nanoscopy of a fluorescent protein-labeled organelle inside a living cell. *Proceedings of the National Academy of Sciences*, 105(38):14271–14276, 2008. 59
- [201] Javad N Farahani, Matthew J Schibler, and Laurent A Bentolila. Stimulated emission depletion (sted) microscopy: from theory to practice. *Microscopy: science, technology, applications and education*, 2(4):1539–1547, 2010. 59

- [202] Louis Thibon, Michel Piché, and Yves De Koninck. Resolution enhancement in laser scanning microscopy with deconvolution switching laser modes (d-slam). *Optics Express*, 26(19):24881–24903, 2018. 59
- [203] Harold Dehez, Michel Piché, and Yves De Koninck. Resolution and contrast enhancement in laser scanning microscopy using dark beam imaging. *Optics express*, 21(13):15912–15925, 2013. 59
- [204] Frans CA Groen, Ian T Young, and Guido Lightart. A comparison of different focus functions for use in autofocus algorithms. *Cytometry: The Journal of the International Society for Analytical Cytology*, 6(2):81–91, 1985. 61
- [205] Bridget Carragher, Nick Kisseberth, David Kriegman, Ronald A Milligan, Clinton S Potter, James Pulokas, and Amy Reilein. Leginon: an automated system for acquisition of images from vitreous ice specimens. *Journal of structural biology*, 132(1):33–45, 2000. 62
- [206] William V Nicholson and Robert M Glaeser. Automatic particle detection in electron microscopy. *Journal of Structural Biology*, 133(2-3):90–101, 2001. 62
- [207] Jianlin Lei and Joachim Frank. Automated acquisition of cryo-electron micrographs for single particle reconstruction on an fei tecnai electron microscope. *Journal of structural biology*, 150(1):69–80, 2005. 62
- [208] David N Mastronarde. Serialem: a program for automated tilt series acquisition on tecnai microscopes using prediction of specimen position. *Microscopy and Microanalysis*, 9(S02):1182–1183, 2003. 62
- [209] Martin Schorb, Isabella Haberbosch, Wim JH Hagen, Yannick Schwab, and David N Mastronarde. Software tools for automated transmission electron microscopy. *Nature methods*, 16(6):471–477, 2019. 62
- [210] AJJ Drenth, AMJ Huiser, and HA Ferwerda. The problem of phase retrieval in light and electron microscopy of strong objects. *Optica Acta: International Journal of Optics*, 22(7):615–628, 1975. 62, 68
- [211] James R Fienup. Reconstruction of an object from the modulus of its fourier transform. *Optics letters*, 3(1):27–29, 1978. 62
- [212] Jianwei Miao, David Sayre, and HN Chapman. Phase retrieval from the magnitude of the fourier transforms of nonperiodic objects. *JOSA A*, 15(6):1662–1669, 1998.
 62
- [213] RHT Bates and JM Rodenburg. Sub-ångström transmission microscopy: a fourier transform algorithm for microdiffraction plane intensity information. *Ultramicroscopy*, 31(3):303–307, 1989. 62
- [214] JM Rodenburg and RHT Bates. The theory of super-resolution electron microscopy via wigner-distribution deconvolution. *Philosophical Transactions of the Royal Society of London. Series A: Physical and Engineering Sciences*, 339(1655):521–553, 1992. 62
- [215] H. M. L. Faulkner and J. M. Rodenburg. Movable Aperture Lensless Transmission Microscopy: A Novel Phase Retrieval Algorithm. *Physical Review Letters*, 93(2):023903, 7 2004. 62, 69

- [216] Michal Odstrčil, Maxime Lebugle, Manuel Guizar-Sicairos, Christian David, and Mirko Holler. Towards optimized illumination for high-resolution ptychography. *Optics express*, 27(10):14981–14997, 2019. 62
- [217] Frederick Allars, Peng-Han Lu, Maximilian Kruth, Rafal E Dunin-Borkowski, John M Rodenburg, and Andrew M Maiden. Efficient large field of view electron phase imaging using near-field electron ptychography with a diffuser. *Ultramicroscopy*, 231:113257, 2021. 62
- [218] W Van den Broek, M Schloz, TC Pekin, PM Pelz, P-H Lu, M Kruth, V Grillo, RE Dunin-Borkowski, RJD Miller, and CT Koch. Towards ptychography with structured illumination, and a derivative-based reconstruction algorithm. *Microscopy and Microanalysis*, 25(S2):58–59, 2019. 62
- [219] Philipp Pelz, Hannah DeVyldere, Peter Ercius, and Mary Scott. Structured illumination electron ptychography at the atomic scale. *Microscopy and Microanalysis*, 28(S1):388–390, 2022. 62
- [220] Oliver Bunk, Martin Dierolf, Søren Kynde, Ian Johnson, Othmar Marti, and Franz Pfeiffer. Influence of the overlap parameter on the convergence of the ptychographical iterative engine. *Ultramicroscopy*, 108(5):481–487, 2008. 62
- [221] Pierre Thibault and Andreas Menzel. Reconstructing state mixtures from diffraction measurements. *Nature*, 494(7435):68–71, 2013. 62, 69
- [222] John Rodenburg and Andrew Maiden. Ptychography. Springer Handbook of Microscopy, pages 819–904, 2019. 62, 99
- [223] Manuel Guizar-Sicairos and James R Fienup. Understanding the twin-image problem in phase retrieval. *JOSA A*, 29(11):2367–2375, 2012. 63, 70
- [224] JM t Cowley and Sumio Iijima. Electron microscope image contrast for thin crystal. *Zeitschrift für Naturforschung A*, 27(3):445–451, 1972. 68, 73
- [225] Wim Coene, Guido Janssen, Marc Op de Beeck, and Dirk Van Dyck. Phase retrieval through focus variation for ultra-resolution in field-emission transmission electron microscopy. *Physical Review Letters*, 69(26):3743, 1992. 68
- [226] BC McCallum and JM Rodenburg. Two-dimensional demonstration of wigner phase-retrieval microscopy in the stem configuration. *Ultramicroscopy*, 45(3-4):371–380, 1992. 68
- [227] JM Rodenburg, BC McCallum, and PD Nellist. Experimental tests on double-resolution coherent imaging via stem. *Ultramicroscopy*, 48(3):304–314, 1993. 68
- [228] BC McCallum and JM Rodenburg. Simultaneous reconstruction of object and aperture functions from multiple far-field intensity measurements. *JOSA A*, 10(2):231–239, 1993. 68
- [229] Liqi Zhou, Jingdong Song, Judy S. Kim, Xudong Pei, Chen Huang, Mark Boyce, Luiza Mendonça, Daniel Clare, Alistair Siebert, Christopher S. Allen, Emanuela Liberti, David Stuart, Xiaoqing Pan, Peter D. Nellist, Peijun Zhang, Angus I. Kirkland, and Peng Wang. Low-dose phase retrieval of biological specimens using cryo-electron ptychography. *Nature Communications*, 11(1):2773, 6 2020. 68

- [230] Xudong Pei, Liqi Zhou, Chen Huang, Mark Boyce, Judy S. Kim, Emanuela Liberti, Yiming Hu, Takeo Sasaki, Peter D. Nellist, Peijun Zhang, David I. Stuart, Angus I. Kirkland, and Peng Wang. Cryogenic electron ptychographic single particle analysis with wide bandwidth information transfer. *Nature Communications*, 14(1):3027, 5 2023. 68, 69
- [231] Berk Küçükoğlu, Inayathulla Mohammed, Ricardo C Guerrero-Ferreira, Massimo Kube, Julika Radecke, Stephanie M Ribet, Georgios Varnavides, Max Leo Leidl, Kelvin Lau, Sergey Nazarov, et al. Low-dose cryo-electron ptychography of proteins at sub-nanometer resolution. *bioRxiv*, pages 2024–02, 2024. 68, 69
- [232] Philipp Michael Pelz, Wen Xuan Qiu, Robert Bücker, Günther Kassier, and R. J. Dwayne Miller. Low-dose cryo electron ptychography via non-convex Bayesian optimization. *Scientific Reports*, 7(1):9883, 8 2017. 68
- [233] Max Leo Leidl, Carsten Sachse, and Knut Müller-Caspary. Dynamical scattering in ice-embedded proteins in conventional and scanning transmission electron microscopy. *IUCrJ*, 10(4):475–486, 7 2023. 68
- [234] Wei Mao, Weiyang Zhang, Chen Huang, Liqi Zhou, Judy. S. Kim, Si Gao, Yu Lei, Xiaopeng Wu, Yiming Hu, Xudong Pei, Weina Fang, Xiaoguo Liu, Jingdong Song, Chunhai Fan, Yuefeng Nie, Angus. I. Kirkland, and Peng Wang. Multi-Convergence-Angle Ptychography with Simultaneous Strong Contrast and High Resolution. arXiv preprint arXiv:2403.16902, 3 2024. 68
- [235] E. Bettens, D. Van Dyck, A.J. den Dekker, J. Sijbers, and A. van den Bos. Model-based two-object resolution from observations having counting statistics. *Ultramicroscopy*, 77(1-2):37–48, 5 1999. 68
- [236] A.J. den Dekker, S. Van Aert, D. Van Dyck, A. van den Bos, and P. Geuens. Does a monochromator improve the precision in quantitative HRTEM? *Ultramicroscopy*, 89(4):275–290, 11 2001. 68
- [237] A. De Backer, S. Van Aert, and D. Van Dyck. High precision measurements of atom column positions using model-based exit wave reconstruction. *Ultramicroscopy*, 111(9-10):1475–1482, 8 2011. 68
- [238] J. Verbeeck and S. Van Aert. Model based quantification of EELS spectra. *Ultramicroscopy*, 101(2-4):207–224, 11 2004. 68
- [239] J. Verbeeck. https://github.com/joverbee/pyEELSMODEL, 2024. 68
- [240] RF Egerton. Limits to the spatial, energy and momentum resolution of electron energy-loss spectroscopy. *Ultramicroscopy*, 107(8):575–586, 2007. 68
- [241] RF Egerton. Control of radiation damage in the tem. *Ultramicroscopy*, 127:100–108, 2013. 68
- [242] C Radhakrishna Rao. Information and the accuracy attainable in the estimation of statistical parameters. In *Breakthroughs in Statistics: Foundations and basic theory*, pages 235–247. Springer, 1992. 69
- [243] Xukang Wei, H Paul Urbach, and Wim MJ Coene. Cramér-rao lower bound and maximum-likelihood estimation in ptychography with poisson noise. *Physical Review A*, 102(4):043516, 2020. 69

- [244] Dorian Bouchet, Jonathan Dong, Dante Maestre, and Thomas Juffmann. Fundamental bounds on the precision of classical phase microscopes. *Phys. Rev. Applied*, 15:24047, 2 2021. 69
- [245] Stewart Koppell and Mark Kasevich. Information transfer as a framework for optimized phase imaging. *Optica*, 8:493–501, 4 2021. 69
- [246] Christian Dwyer. Quantum Limits of Transmission Electron Microscopy. *Physical Review Letters*, 130(5):056101, 1 2023. 69, 75
- [247] Andrew M. Maiden and John M. Rodenburg. An improved ptychographical phase retrieval algorithm for diffractive imaging. *Ultramicroscopy*, 109(10):1256–1262, 9 2009. 69
- [248] P. D. Nellist, B. C. McCallum, and J. M. Rodenburg. Resolution beyond the 'information limit' in transmission electron microscopy. *Nature*, 374(6523):630–632, 4 1995. 69
- [249] Hao Yang, Timothy J. Pennycook, and Peter D. Nellist. Efficient phase contrast imaging in STEM using a pixelated detector. Part II: Optimisation of imaging conditions. *Ultramicroscopy*, 151:232–239, 4 2015. 69
- [250] A. Parvizi, J. Müller, S.A. Funken, and C.T. Koch. A practical way to resolve ambiguities in wavefront reconstructions by the transport of intensity equation. *Ultramicroscopy*, 154:1–6, 7 2015. 69
- [251] Robert M Glaeser. Limitations to significant information in biological electron microscopy as a result of radiation damage. *Journal of ultrastructure research*, 36(3-4):466–482, 1971. 69
- [252] James Z Chen, Carsten Sachse, Chen Xu, Thorsten Mielke, Christian MT Spahn, and Nikolaus Grigorieff. A dose-rate effect in single-particle electron microscopy. *Journal of structural biology*, 161(1):92–100, 2008. 69
- [253] Takanori Nakane, Abhay Kotecha, Andrija Sente, Greg McMullan, Simonas Masiulis, Patricia MGE Brown, Ioana T Grigoras, Lina Malinauskaite, Tomas Malinauskas, Jonas Miehling, et al. Single-particle cryo-em at atomic resolution. *Nature*, 587(7832):152–156, 2020. 69
- [254] Ashwin Chari and Holger Stark. Prospects and limitations of high-resolution single-particle cryo-electron microscopy. *Annual Review of Biophysics*, 52(1):391–411, 2023. 69
- [255] Max Leo Leidl, Benedikt Diederichs, Carsten Sachse, and Knut Müller-Caspary. Influence of loss function and electron dose on ptychography of 2D materials using the Wirtinger flow. *Micron*, 185:103688, 10 2024. 69, 87
- [256] RF Egerton. Dose measurement in the tem and stem. *Ultramicroscopy*, 229:113363, 2021. 69
- [257] Robert A Gonsalves. Phase retrieval and diversity in adaptive optics. *Optical Engineering*, 21(5):829–832, 1982. 69
- [258] James R Fienup. Phase-retrieval algorithms for a complicated optical system. *Applied optics*, 32(10):1737–1746, 1993. 69

- [259] Cheng Liu, T Walther, and JM Rodenburg. Influence of thick crystal effects on ptychographic image reconstruction with moveable illumination. *Ultramicroscopy*, 109(10):1263–1275, 2009. 69
- [260] HL Robert, I Lobato, FJ Lyu, Q Chen, S Van Aert, D Van Dyck, and K Müller-Caspary. Dynamical diffraction of high-energy electrons investigated by focal series momentum-resolved scanning transmission electron microscopy at atomic resolution. *Ultramicroscopy*, 233:113425, 2022. 69
- [261] Andrew M Maiden, Martin J Humphry, and John M Rodenburg. Ptychographic transmission microscopy in three dimensions using a multi-slice approach. *JOSA A*, 29(8):1606–1614, 2012. 69
- [262] Hamish G Brown, Zhen Chen, Matthew Weyland, Colin Ophus, Jim Ciston, Les J Allen, and Scott D Findlay. Structure retrieval at atomic resolution in the presence of multiple scattering of the electron probe. *Physical Review Letters*, 121(26):266102, 2018. 69
- [263] Michael Chen, David Ren, Hsiou-Yuan Liu, Shwetadwip Chowdhury, and Laura Waller. Multi-layer born multiple-scattering model for 3d phase microscopy. *Optica*, 7(5):394–403, 2020. 69
- [264] David Ren, Colin Ophus, Michael Chen, and Laura Waller. A multiple scattering algorithm for three dimensional phase contrast atomic electron tomography. *Ultramicroscopy*, 208:112860, 2020. 69
- [265] Hide Yoshioka. Effect of inelastic waves on electron diffraction. *Journal of the Physical Society of Japan*, 12(6):618–628, 1957. 69
- [266] Christian Dwyer. Multislice theory of fast electron scattering incorporating atomic inner-shell ionization. *Ultramicroscopy*, 104(2):141–151, 2005. 69
- [267] Christian Dwyer, Scott David Findlay, and Leslie J Allen. Multiple elastic scattering of core-loss electrons in atomic resolution imaging. *Physical Review B—Condensed Matter and Materials Physics*, 77(18):184107, 2008. 69
- [268] Leslie J Allen, SD Findlay, et al. Modelling the inelastic scattering of fast electrons. *Ultramicroscopy*, 151:11–22, 2015. 69
- [269] Andreas Beyer, Florian F Krause, Hoel L Robert, Saleh Firoozabadi, Tim Grieb, Pirmin Kükelhan, Damien Heimes, Marco Schowalter, Knut Müller-Caspary, Andreas Rosenauer, et al. Influence of plasmon excitations on atomic-resolution quantitative 4d scanning transmission electron microscopy. *Scientific reports*, 10(1):17890, 2020. 69
- [270] HL Robert, B Diederichs, and Knut Müller-Caspary. Contribution of multiple plasmon scattering in low-angle electron diffraction investigated by energy-filtered atomically resolved 4d-stem. *Applied Physics Letters*, 121(21), 2022. 69
- [271] PD Nellist and JM Rodenburg. Beyond the conventional information limit: the relevant coherence function. *Ultramicroscopy*, 54(1):61–74, 1994. 69
- [272] Timur E Gureyev, Ya I Nesterets, DM Paganin, A Pogany, and SW Wilkins. Linear algorithms for phase retrieval in the fresnel region. 2. partially coherent illumination. *Optics communications*, 259(2):569–580, 2006. 69

- [273] AV Martin, F-R Chen, W-K Hsieh, J-J Kai, SD Findlay, and LJ Allen. Spatial incoherence in phase retrieval based on focus variation. *Ultramicroscopy*, 106(10):914–924, 2006. 69
- [274] Mark P Oxley and Ondrej E Dyck. The importance of temporal and spatial incoherence in quantitative interpretation of 4d-stem. *Ultramicroscopy*, 215:113015, 2020. 69
- [275] Benedikt Diederichs, Ziria Herdegen, Achim Strauch, Frank Filbir, and Knut Müller-Caspary. Exact inversion of partially coherent dynamical electron scattering for picometric structure retrieval. *Nature Communications*, 15(1):101, 2024. 69, 88, 89
- [276] Veit Elser, Ti-Yen Lan, and Tamir Bendory. Benchmark problems for phase retrieval. *SIAM Journal on Imaging Sciences*, 11(4):2429–2455, 2018. 69
- [277] Richard Tolimieri, Myoung An, and Chao Lu. *Mathematics of multidimensional Fourier transform algorithms*. Springer Science & Business Media, 2012. 70
- [278] Frederick Allars, Peng-Han Lu, Maximilian Kruth, Rafal E Dunin-Borkowski, John M Rodenburg, and Andrew M Maiden. Efficient large field of view electron phase imaging using near-field electron ptychography with a diffuser. *Ultramicroscopy*, 231:113257, 7 2021. 70, 88, 98
- [279] Timothy JT Abregana and Percival F Almoro. Phase retrieval by amplitude modulation using digital micromirror device. *Optics and Lasers in Engineering*, 150:106851, 2022. 70, 98
- [280] Shengbo You, Peng-Han Lu, Thomas Schachinger, András Kovács, Rafal E Dunin-Borkowski, and Andrew M Maiden. Lorentz near-field electron ptychography. *Applied Physics Letters*, 123(19), 2023. 70, 88, 98
- [281] Chu-Ping Yu, Francisco Vega Ibañez, Armand Béché, and Johan Verbeeck. Quantum wavefront shaping with a 48-element programmable phase plate for electrons. *SciPost Physics*, 15(6):223, 12 2023. 70, 98
- [282] Francisco Vega Ibáñez, Armand Béché, and Johan Verbeeck. Can a Programmable Phase Plate Serve as an Aberration Corrector in the Transmission Electron Microscope (TEM)? *Microscopy and Microanalysis*, 29(1):341–351, 2 2023. 70
- [283] R. J. Barlow. *A Guide to the Use of Statistical Methods in the Physical Sciences*. John Wiley & Sons, Chichester, 1991. 71
- [284] Harold Cramer. Mathematical methods of statistics, princeton univ. *Press, Princeton, NJ*, 27, 1946. 71, 81
- [285] C. R. Rao. Information and the accu-racy attainable in the estimation of statistical parameters. *Bulletin of the Calcutta Mathematical Society*, 37:81–89, 1945. 71
- [286] Radostin Danev, Dimitry Tegunov, and Wolfgang Baumeister. Using the volta phase plate with defocus for cryo-em single particle analysis. *Elife*, 6:e23006, 2017.

- [287] Marek Malac, Simon Hettler, Misa Hayashida, Emi Kano, Ray F Egerton, and Marco Beleggia. Phase plates in the transmission electron microscope: operating principles and applications. *Microscopy*, 70(1):75–115, 2021. 72
- [288] Hermann Struve. Beitrag zur theorie der diffraction an fernröhren. *Annalen der Physik*, 253(13):1008–1016, 1882. 73
- [289] Miloš Vulović, Lenard M Voortman, Lucas J van Vliet, and Bernd Rieger. When to use the projection assumption and the weak-phase object approximation in phase contrast cryo-em. *Ultramicroscopy*, 136:61–66, 2014. 73
- [290] Dennis Gabor. A new microscopic principle. Nature, 161:777–778, 1948. 74
- [291] Akira Tonomura, Tsuyoshi Matsuda, and Tsutomu Komoda. Two beam interference with field emission electron beam. *Japanese Journal of Applied Physics*, 17(6):1137, 1978. 74
- [292] Hannes Lichte and Michael Lehmann. Electron holography—basics and applications. *Reports on Progress in Physics*, 71(1):016102, 2007. 74
- [293] R F Egerton. Mechanisms of radiation damage in beam-sensitive specimens, for tem accelerating voltages between 10 and 300 kv. *Microscopy Research and Technique*, 75(11):1550–1556, 11 2012. 74
- [294] R.F. Egerton. Scattering delocalization and radiation damage in STEM-EELS. *Ultramicroscopy*, 0:1–10, 4 2017. 74
- [295] RF Egerton, AM Blackburn, RA Herring, L Wu, and Y Zhu. Direct measurement of the psf for coulomb delocalization—a reconsideration. *Ultramicroscopy*, 230:113374, 2021. 74
- [296] D. Jannis, A. Velazco, A. Béché, and J. Verbeeck. Reducing electron beam damage through alternative STEM scanning strategies, Part II: Attempt towards an empirical model describing the damage process. *Ultramicroscopy*, 240:113568, 10 2022.
- [297] A. Velazco, A. Béché, D. Jannis, and J. Verbeeck. Reducing electron beam damage through alternative STEM scanning strategies, Part I: Experimental findings. *Ultramicroscopy*, 232:113398, 1 2022. 74
- [298] Erich Müller, Katharina Adrion, Milena Hugenschmidt, and Dagmar Gerthsen. Reaction-diffusion study of electron-beam-induced contamination growth. *Ultramicroscopy*, page 113995, 2024. 74
- [299] Stewart Koppell and Mark Kasevich. Information transfer as a framework for optimized phase imaging. *Optica*, 8(4):493–501, 2021. 75
- [300] Jo Verbeeck and Francisco Vega. Python phase retrieval module, August 2024. 75
- [301] Christian Dwyer and David M Paganin. Quantum and classical fisher information in four-dimensional scanning transmission electron microscopy. *Physical Review B*, 110(2):024110, 2024. 77
- [302] Richard C Aster, Brian Borchers, and Clifford H Thurber. *Parameter estimation and inverse problems*. Elsevier, 2018. 78

- [303] Guo-zhen Yang, Bi-zhen Dong, Ben-yuan Gu, Jie-yao Zhuang, and Okan K Ersoy. Gerchberg–saxton and yang–gu algorithms for phase retrieval in a nonunitary transform system: a comparison. *Applied optics*, 33(2):209–218, 1994. 79
- [304] Zeev Zalevsky, David Mendlovic, and Rainer G Dorsch. Gerchberg–saxton algorithm applied in the fractional fourier or the fresnel domain. *Optics Letters*, 21(12):842–844, 1996. 79
- [305] Guoqiang Huang, Daixuan Wu, Jiawei Luo, Liang Lu, Fan Li, Yuecheng Shen, and Zhaohui Li. Generalizing the gerchberg–saxton algorithm for retrieving complex optical transmission matrices. *Photonics Research*, 9(1):34–42, 2020. 79
- [306] Adriaan Van den Bos. Estimation of fourier coefficients. *IEEE transactions on instrumentation and measurement*, 38(5):1005–1007, 1989. 80
- [307] Ronald Aylmer Fisher. Theory of statistical estimation. In *Mathematical proceedings of the Cambridge philosophical society*, volume 22, pages 700–725. Cambridge University Press, 1925. 81
- [308] AJ Den Dekker, S Van Aert, A Van den Bos, and D Van Dyck. Maximum likelihood estimation of structure parameters from high resolution electron microscopy images. part i: A theoretical framework. *Ultramicroscopy*, 104(2):83–106, 2005. 81
- [309] Oleh Melnyk. Convergence properties of gradient methods for blind ptychography. *arXiv preprint arXiv:2306.08750*, 2023. 83
- [310] Unknown. https://hdl.handle.net/1721.3/195767, 1978. 84
- [311] Pierre Godard, Marc Allain, Virginie Chamard, and John Rodenburg. Noise models for low counting rate coherent diffraction imaging. *Optics express*, 20(23):25914–25934, 2012. 87
- [312] Peng Li, Tega B Edo, and John M Rodenburg. Ptychographic inversion via wigner distribution deconvolution: noise suppression and probe design. *Ultramicroscopy*, 147:106–113, 2014. 87
- [313] CM O'Leary, CS Allen, C Huang, JS Kim, E Liberti, PD Nellist, and AI Kirkland. Phase reconstruction using fast binary 4d stem data. *Applied Physics Letters*, 116(12), 2020. 87
- [314] Colum M O'Leary, Gerardo T Martinez, Emanuela Liberti, Martin J Humphry, Angus I Kirkland, and Peter D Nellist. Contrast transfer and noise considerations in focused-probe electron ptychography. *Ultramicroscopy*, 221:113189, 2021. 87
- [315] P. Kruit, R.G. Hobbs, C-S. Kim, Y. Yang, V.R. Manfrinato, J. Hammer, S. Thomas, P. Weber, B. Klopfer, C. Kohstall, T. Juffmann, M.A. Kasevich, P. Hommelhoff, and K.K. Berggren. Designs for a quantum electron microscope. *Ultramicroscopy*, 164:31–45, 5 2016. 87
- [316] Thomas Juffmann, Stewart A Koppell, Brannon B Klopfer, Colin Ophus, Robert M Glaeser, and Mark A Kasevich. Multi-pass transmission electron microscopy. *Scientific reports*, 7(1):1699, 2017. 87

- [317] Stewart A Koppell, Marian Mankos, Adam J Bowman, Yonatan Israel, Thomas Juffmann, Brannon B Klopfer, and Mark A Kasevich. Design for a 10 kev multipass transmission electron microscope. *Ultramicroscopy*, 207:112834, 2019. 87, 99
- [318] Amy E. Turner, Cameron W. Johnson, Pieter Kruit, and Benjamin J. McMorran. Interaction-Free Measurement with Electrons. *Physical Review Letters*, 127(11):110401, 9 2021. 87
- [319] Stewart A Koppell, Yonatan Israel, Adam J Bowman, Brannon B Klopfer, and Mark A Kasevich. Transmission electron microscopy at the quantum limit. *Applied Physics Letters*, 120(19), 2022. 87
- [320] Marco Beleggia. A formula for the image intensity of phase objects in Zernike mode. *Ultramicroscopy*, 108(9):953–958, 2008. 88
- [321] Pierre Thibault and Manuel Guizar-Sicairos. Maximum-likelihood refinement for coherent diffractive imaging. *New Journal of Physics*, 14(6):063004, 2012. 88
- [322] Marcel Schloz, Thomas Christopher Pekin, Zhen Chen, Wouter Van den Broek, David Anthony Muller, and Christoph Tobias Koch. Overcoming information reduced data and experimentally uncertain parameters in ptychography with regularized optimization. *Optics Express*, 28(19):28306, 9 2020. 88
- [323] Andrew Maiden, Daniel Johnson, and Peng Li. Further improvements to the ptychographical iterative engine. *Optica*, 4(7):736, 7 2017. 88
- [324] David L Donoho. Compressed sensing. *IEEE Transactions on information theory*, 52(4):1289–1306, 2006. 88
- [325] Rowan Leary, Zineb Saghi, Paul A Midgley, and Daniel J Holland. Compressed sensing electron tomography. *Ultramicroscopy*, 131:70–91, 2013. 88
- [326] Xin Li, Ondrej Dyck, Sergei V Kalinin, and Stephen Jesse. Compressed sensing of scanning transmission electron microscopy (stem) with nonrectangular scans. *Microscopy and Microanalysis*, 24(6):623–633, 2018. 88
- [327] Wouter Van den Broek, Bryan W. Reed, Armand Beche, Abner Velazco, Johan Verbeeck, and Christoph T. Koch. Various Compressed Sensing Setups Evaluated Against Shannon Sampling Under Constraint of Constant Illumination. *IEEE Transactions on Computational Imaging*, 5(3):502–514, 9 2019. 89
- [328] Timepix Poikela, J Plosila, T Westerlund, M Campbell, M De Gaspari, X Llopart, V Gromov, R Kluit, M Van Beuzekom, F Zappon, et al. Timepix3: a 65k channel hybrid pixel readout chip with simultaneous toa/tot and sparse readout. *Journal of instrumentation*, 9(05):C05013, 2014. 97
- [329] Xavier Llopart, Jerome Alozy, Rafael Ballabriga, Michael Campbell, Raimon Casanova, Vladimir Gromov, EHM Heijne, Tuomas Poikela, Edinei Santin, Viros Sriskaran, et al. Timepix4, a large area pixel detector readout chip which can be tiled on 4 sides providing sub-200 ps timestamp binning. *Journal of Instrumentation*, 17(01):C01044, 2022. 97

- [330] Daen Jannis, Christoph Hofer, Chuang Gao, Xiaobin Xie, Armand Béché, Timothy J Pennycook, and Jo Verbeeck. Event driven 4d stem acquisition with a timepix3 detector: Microsecond dwell time and faster scans for high precision and low dose applications. *Ultramicroscopy*, 233:113423, 2022. 97
- [331] Yves Auad, Michael Walls, Jean-Denis Blazit, Odile Stéphan, Luiz HG Tizei, Mathieu Kociak, Francisco de La Peña, and Marcel Tencé. Event-based hyperspectral eels: towards nanosecond temporal resolution. *Ultramicroscopy*, 239:113539, 2022. 97
- [332] J Paul van Schayck, Yue Zhang, Kèvin Knoops, Peter J Peters, and Raimond BG Ravelli. Integration of an event-driven timepix3 hybrid pixel detector into a cryoem workflow. *Microscopy and Microanalysis*, 29(1):352–363, 2023. 97
- [333] Simon Garrigou and Hugo Lourenço-Martins. Atomic-like selection rules in free electron scattering. *arXiv preprint arXiv:2411.11754*, 2024. 98
- [334] Marc R Bourgeois, Andrew W Rossi, and David J Masiello. Strategy for direct detection of chiral phonons with phase-structured free electrons. *arXiv preprint* arXiv:2405.01826, 2024. 98
- [335] Lee Wei Wesley Wong and Liang Jie Wong. Enhancing x-ray generation from twisted multilayer van der waals materials by shaping electron wavepackets. *npj Nanophotonics*, 1(1):41, 2024. 98
- [336] Adamantios P Synanidis, PAD Gonçalves, and F de Abajo. Rydberg-atom manipulation through strong interaction with free electrons. *arXiv preprint* arXiv:2409.18913, 2024. 98
- [337] Jagan Singh Meena, Simon Min Sze, Umesh Chand, and Tseung-Yuen Tseng. Overview of emerging nonvolatile memory technologies. *Nanoscale research letters*, 9:1–33, 2014. 98
- [338] Chu-Ping Yu, Francisco Vega Ibañez, Armand Béché, and Johan Verbeeck. Quantum wavefront shaping with a 48-element programmable phase plate for electrons. *SciPost Physics*, 15(6):223, 2023. 99
- [339] Jack Black (Actor) Liam Lynch (Director). Tenacious d in the pick of destiny. Film, 2006. Scene: J.B. meets Kyle Gass. 117

"It gets easier. Every day, it gets a little easier. But you gotta do it every day — That's the hard part... But it does get easier."

Jogger, BoJack Horseman S02, E12.

BIBLIOGRAPHY

